MODELLING AND EXPERIMENTAL CHARACTERIZATION OF RESONANT PANEL SOUND ABSORBERS

Antonio Esposito

A thesis submitted in partial fulfillment of the degree of Doctor of Philosophy in Industrial Engineering, XXXV Cycle

Department of Industrial Engineering
University of Naples Federico II

Supervisor:
Prof. Rosario Aniello Romano

Antonio Esposito:
Modelling and Experimental Characterization of Resonant Panel Sound Absorbers,
October 2022

Supervisor:
Prof. Rosario Aniello Romano

Ph.D. Programme Coordinator:
Prof. Michele Grassi

Location:
Naples

Date:
October 2022

Ohana means family.
Family means nobody gets left behind, or forgotten.

Dedicated to my mother.

Abstract in lingua italiana

La modellazione analitica dell'impedenza acustica di risuonatori a membrana è stata oggetto di numerosi studi, al fine di ottenerne una caratterizzazione appropriata ad analisi di tipo previsionale. Tuttavia, i modelli di impedenza maggiormente utilizzati nella pratica della progettazione acustica si basano sull'ipotesi di moto pistonico delle membrane, introducendo margini di errore significativi rispetto al reale comportamento di assorbitori di dimensione finita, in cui il comportamento modale è predominante. In questo lavoro di tesi viene proposta una espressione analitica dell'impedenza acustica media superficiale di assorbitori a membrana, in cui le impedenze di piastre vibranti di diverse forme e condizioni di vincolo, eccitate trasversalmente da un carico di pressione, sono state sommate in serie con l'impedenza della cavità retrostante, calcolata mediante il teorema di traslazione dell'impedenza. Tale espressione è stata validata in condizioni di incidenza normale piana, sperimentalmente nel caso di piastre isolate e incastrate ai bordi e numericamente nel caso di sistemi accoppiati piastra-cavità. Ulteriori analisi numeriche sono state effettuate al fine di apprezzare gli effetti dovuti alla presenza di uno strato di materiale poroso all'interno della cavità. Inoltre, la risposta in termini di impedenza di un assorbitore di forma quadrata è stata analizzata numericamente e in via preliminare in condizioni di incidenza sferica in campo libero. L'applicabilità della formulazione proposta come condizione di impedenza superficiale in modelli FEM acustici è stata investigata grazie all'applicazione al caso studio di una stanza reale. Le risposte in frequenza in termini di livello della pressione sonora e i tempi di riverberazione T_{30} numerici e sperimentali sono stati confrontati tra loro per due diverse configurazioni di trattamento acustico, mostrando margini di errore accettabili a bassa frequenza, sebbene lo scarto tra i dati numerici e quelli sperimentali abbia mostrato un trend in leggera crescita, all'aumentare del numero di pannelli presenti nella stanza. A questo proposito, si rendono necessarie ulteriori verifiche in presenza di un quantitativo significativamente più alto di superfici fonoassorbenti e, possibilmente, perfezionando le metodologie di calibrazione dei modelli numerici per tenere conto di possibili fonti ignote di dissipazione acustica. Tuttavia, i risultati ottenuti finora suggeriscono una discreta affidabilità nell'applicazione di tale metodologia, utile ad eludere, quando possibile, l'esigenza di effettuare simulazioni multifisiche che, generalmente, risultano essere estremamente più dispendiose in termini di tempi computazionali.

Abstract

The analytical modelling of the acoustic impedance of panel absorbers has been extensively addressed for the purpose of acoustic predictive analyses. Nevertheless, established approximate design equations rely on the assumption of pistonic plate motion, leading to significant errors with respect to finite sized samples, in which the flexural multimodal behaviour of the plate is predominant. In this thesis, an analytical expression of the surface averaged acoustic impedance of finite sized panel absorbers is obtained, by adding in series the impedance expression of vibrating plates of various shapes and edge constraints, excited by a transverse pressure load, to the acoustic impedance of a multilayered air cavity, calculated according to the impedance translation theorem. Such expressions were validated for normal sound incidence conditions, experimentally for the isolated clamped plate and numerically for the panel-cavity coupled system. Further numerical investigations were performed upon the effects of a porous layer inserted within the cavity as well as the response of a square panel absorber for conditions of spherical sound incidence in free field. The applicability of the proposed formulation as a boundary impedance condition in room acoustics FEM models was investigated for the case study of an existing room. Results in terms of sound pressure level frequency responses and T_{30} were compared against measured data at low frequencies for two different configurations of treatment, respectively showing reasonable deviations at low frequency. Since slight error increments were observed by increasing the number of panel absorbers in the room, further investigation is required by significantly increasing the surface area of acoustic treatment and refining calibration strategies of numerical models when accounting for unknown sources of acoustic damping. Nonetheless, results observed so far are promising towards the use of this methodology to bypass, when possible, the need of performing multiphysics FEM simulations which, in general, are extremely more expensive in terms of computational costs.

Acknowledgments

I am sincerely grateful to my Ph.D. tutor, prof. Rosario Aniello Romano, for his unvaluable guidance throughout the last few years.
I am also thankful to prof. Raffaele Dragonetti and my laboratory mates Marialuisa and Elio, for the fruitful opportunities of discussion and the nice days spent together.
Many thanks go to Emanuele Porcinai and Bradley Alexander from the Technische Universität of Berlin, for the good memories built together and the genuine moments of sharing and teamworking, which were very rare for me to find elsewhere.
Finally, the deepest gratitude goes to my family, for their continuous support and everlasting love.

List of Figures

List of Tables

Contents

Introduction

In the practice of room acoustics design, resonant panel sound absorbers are frequently employed to achieve efficient sound absorption at low frequency, due to their ease of construction and cost efficiency. Indeed, differently from porous absorbers which require large thicknesses in order to be effective at low frequency, panel resonators generally require small cavity depths which, in most cases, are compliant with architectural design needs. Nevertheless, the most employed design equations in the acoustic design practice are derived from approximate models, which present some drawbacks and inaccuracies when applied to non-idealized cases. In particular, they rely upon the schematization of panel-cavity coupled systems as single degree of freedom (SDOF) mass-spring oscillators. With this model, the normal acoustic impedance of plate-cavity coupled systems is obtained by means of electrical analogies, accounting for panel resistance, inertance and air cavity acoustic compliance. According to this, resonance frequencies are dependent primarily on the plate surface mass and bulk stiffness of the air cavity. Nevertheless, inaccuracies arise due to the underlying physical assumptions. Firstly, pistonic motion of the plate is assumed: higher order flexural modes of the plate are not taken into account, as well as the finite size of the sample which, as will be outlined, have a relevant effect on the resulting resonances of the system, implying absorption peaks to be significantly shifted in frequency with respect to the SDOF simplified solution.

On this purpose, the research activity conducted in the context of the doctoral course and summarized in this thesis, aimed to the definition of an extended analytical model, including the contribution due to the vibrational modal behaviour of the plate, with the aim to provide acoustic designers with a tool which may improve the accuracy of predictive analyses when dealing to noise control at low frequency, particularly in small rooms, such as recording studio control rooms, dubbing rooms or similar environments where critical listening represents an essential requirement. For these purposes, the knowledge of the acoustic surface impedance of absorptive boundaries becomes crucial to set properly numerical models, which are necessary to perform accurate predictive analyses, specifically below the Schroeder frequency, where geometrical acoustics based simulation methods do not provide reliable results. In this thesis, the outcomes of a set of experimental and numerical analyses are presented, in order to investigate the effects of different plate shapes and edge constraint conditions, and particularly focusing on rectangular plates coupled to a backing air cavity, with and without the presence of layers of porous material within the latter.

In order to highlight the methodology adopted, an outline of the thesis is reported hereby. In the first part, an overview of the basic concepts underlying the characterization of panel absorbers is provided, by referring to relevant contributions from scientific literature. In particular, after a brief introduction on the principles of sound absorption mechanisms, sound absorption metrics are described highlighting the importance of the acoustic impedance for predictive analyses at low frequency. Then, the derivation of the specific acoustic impedance of vibrating plates is described starting from the equation of motion as defined according to the Kirchhoff's thin plate theory. A frequency dependent expression of acoustic impedance is reported for circular and rectangular plates in both simply supported and clamped edge constraint conditions. With reference to panel-cavity coupled systems, the above mentioned approximate models for the evaluation of acoustic impedance are described, highlighting possible inaccuracies with the support of experimental data provided in literature. Existing extended models accounting for the modal behaviour of plates are also described, the applicability of which is limited to square shaped samples.

In Part II, preliminary investigations and a set of numerical-experimental validations are presented. In the first instance, the outcomes of preliminary FEM analyses are reported, with the aim of highlighting the effects on the surface impedance of panel absorbers due to the finite size of the sample and to different edge constraint conditions. Thenceforth, the analytical frequency expressions of the specific acoustic impedance of clamped rectangular and circular plates were compared against experimental data resulting from acoustical transmission loss measurements in an impedance tube. Furthermore, the response of a clamped rectangular plate to plane oblique sound incidence is investigated by means of FEM simulations, replicating free field conditions for a set of incidence angles.

Consequently to the validation of impedance expressions of isolated clamped plates, the analytical expression of the surface averaged acoustic impedance of plate-cavity coupled resonators is presented for circular and rectangular samples. Such expression is validated numerically, by means of FEM simulations, assuming plane wave normal incidence conditions. Furthermore, the effects of porous absorbers inserted into the cavity are investigated numerically. Finally, the response of a square resonator to spherical sound incidence is investigated by simulating sound incidence from a monopole source placed at several heights upon the sample, in free-field conditions.

In Part III, the applicability of the analytical expression so calculated as boundary impedance conditions in FEM room acoustics models was tested, by means of a numerical-experimental investigation applied to a case study involving a real sized room. For this purpose, a small sized rectangular room was chosen and acoustically treated with panel absorbers. In particular, the validation of a FEM model of the empty room configuration against measured impulse responses is reported and the results of the modal analysis of the sound field in the room are presented. The design stages of panel absorbers are described and two configuration of acoustic treatment are proposed and numerically simulated. FEM models of treated room configurations are validated against measured data, in terms of sound pressure level responses and reverberation times at receiver positions.

Concluding remarks, highlighting the limitations of such a methodology and the proposal of possible further developments are reported in the conclusions.

Part I

Literature Review

In the following chapters, an overview of the fundamental concepts at the basis of the characterization of panel sound absorbers is provided. The state of the art and the scientific international context is analyzed, highlighting the main limitations and contributions to this research work.
Firstly, a description of porous and resonance sound absorption mechanisms is introduced, emphasizing the importance of wave based acoustic metrics, such as acoustic impedance, with respect to energy descriptors, when dealing with room acoustics predictive analyses in the low modal density region. Indeed, since in this case wave propagation effects play an important role, complex quantities become necessary to build up an exhaustive analytical formulation.
A thorough description regarding the dynamic response of thin plates excited by transverse loads is provided: the basic assumptions and the field of validity of the thin plate theory are reported and the equation of motion is derived for plates of different shapes and constraint conditions. Particular attention is paid to the derivation of a frequency dependent equation of the specific acoustic impedance, due to its crucial importance in the analytical characterization of panel sound absorbers. The main differences between infinite and finite sized plates are highlighted, as well as the influence of different shapes and edge constraint conditions. Plate-cavity coupling conditions are analyzed and an overview of existing analytical formulations of the acoustic surface impedance of panel absorbers is reported, ranging from approximate to more complex models.

1 Principles of sound absorption: a brief overview

When a sound wave in air impinges the surface of an object, part of the sound energy can be reflected back to the air domain or transmitted through the object, whilst some other amount of energy can be dissipated across the obstacle material, depending on its microscopic properties, mechanical behavior and mounting conditions. Such a phenomenon can be defined as sound absorption and it represents the most important mechanism at the basis of noise control, especially in enclosed spaces. Depending on the mechanism of energy dissipation, sound absorption systems can be grouped in two major categories: porous and resonant absorbers.

Porous sound absorption occurs due to the thermoviscous dissipation generated by the interaction of oscillating air particles with the microstructural skeleton of the porous material. The most common materials included in this category are fibers (such as rockwool, glasswool, woodwool and polyester fiber), foams (melamine, polyurethane foams) or granular foams (sintered ceramic and metallic materials, aggregates of recycled materials). Specific intrinsic properties of such materials are responsible of the amount of sound energy absorbed: in particular, porosity determines the percentage of air within the material volume, and the quantifies the amount of air possibly passing through pores; tortuosity describes how much air flows paths can be irregular through the material, due to the structural shape of its pores – the greater the tortuosity the less the absorption; air flow resistivity is a measure of the resistance per unit length encountered by an air flow passing through the thickness of a porous material. These properties determine, in some extent, how much friction is generated by the motion of air particles against pores boundaries, allowing for sound energy dissipation into heat. In light of this, it becomes crucial that surfaces of porous materials are located in areas where the profile of air particle velocity becomes maximum. This usually happens at a distance of a quarter wavelength from the nearest rigid surface: in light of this, being equal the thickness of the porous material, the smaller the wavelength, the greater the absorption.

The class of resonant absorbers includes panel and membrane absorbers and cavity resonators such as Helmholtz resonators. With reference to the former, which also constitute the main topic of this thesis, they are usually made up of a flexible thin plate backed by an air cavity volume, in which a layer of porous material is usually placed in order to increase the damping at maximum absorption frequencies. Notably, in scientific literature, it is common to point out nomenclature differences between *panel* and *membrane* absorbers: generally, the former refers to thin plates with no in-plane pre-stress conditions applied, as in the case of the latter, implying notable differences in terms of their dynamic responses.

On the other hand, Helmholtz resonators are generally made up of a rigid air cavity connected to the outer air domain by means of a small hole, named *neck* having specific length and cross section, which determines the amount of air mass oscillating against the cavity volume, implying the system to behave as a mass-spring oscillator. Differently from the case of porous absorption, resonance absorption happens when maximum sound pressure occurs at the interface between air and the resonating surface. In resonant absorbers, maximum absorption occurs at the resonance frequencies of the system, which can be defined depending on the type of absorber in question. For instance, resonances in panel absorbers are governed by several factors, such as panel mass and cavity stiffness. Those quantities are the only considered in very approximate models, which assume the motion of the plate to be pistonic, neglecting the panel flexural stiffness and the contribution of the higher order flexural modes of the plate.

1.1 Acoustic absorption metrics

In light of the comparison between porous and resonance absorbers, it is worthwhile to point out the frequency ranges where such systems show their best efficiency in terms of sound absorption. As mentioned, in porous materials sound absorption usually increases with frequency, fixed the thickness. This allows for a broadband absorption achieving its highest value at the frequency where air particle velocity is maximum, namely at a quarter wavelength from the rigid boundaries of an enclosed space. Nevertheless, commonly employed thicknesses of porous materials are not large enough to provide effective absorption at low frequencies, in compliance with usual architectural needs. This implies that, in most cases, sound absorption provided by porous materials starts to be effective at mid-high frequencies. On the other hand, resonance absorbers are also defined as pressure absorbers: due to the configuration of such devices, they are generally designed to resonate – and then achieve highest absorption – at low frequencies, being placed in areas of maximum sound pressure rather then velocity and usually large thicknesses of the samples are not required. Considering this, it is useful to investigate which sound absorption metrics are more appropriate to quantify the efficiency of such systems depending on the frequency range of interest. In particular, mid-high frequencies predictive analyses of sound fields in enclosed spaces are mainly based on geometrical and statistical evaluations, due to the assumption of a perfectly diffuse sound field: in this case, it is assumed to be composed of a set of energy rays travelling in all directions and that the mean square pressure of each propagating wave is the same, regardless of direction. Under these assumptions, energy descriptors such as reflection and absorption coefficient are commonly adopted in mid-high frequency predictive analyses with an acceptable degree of reliability. Conversely, low frequency modal analysis, generally based on the direct solution of the acoustic wave equation, requires the definition of appropriate boundary conditions by means of complex functions, such as the acoustic impedance, in order to take in account of all possible effects due to wave propagation.
In the following paragraphs, both types of metrics are described, providing a definition of them and investigating, where possible, their field of applicability, since their formulation strictly depends on both the characteristics of the incident sound field and of the material layer in question.

1.1.1 Wave based metrics: characteristic, mechanical and specific acoustic Impedance

Impedance is an important quantity, extensively used in acoustics to describe how a sound field interacts with an obstacle subjected to acoustic excitation: it determines the resistance of a particular medium to the propagation of an acoustic wave through it, providing a useful relationship between acoustic pressure and particle velocity. Different types of acoustic impedance are generally used in different contexts of analysis. It is important to note that the expression of such impedances depends on the properties of the sound field. The assumption at the basis of impedance definitions is that the application of a harmonic sound pressure or force to the surface of a material will generate a periodic velocity field with fixed phase with respect to the applied force.

The first type of impedance is the *characteristic acoustic impedance* Z_c, which denotes the resistance that a medium opposes to the flow of sound energy. For the sake of example, assuming a harmonic plane wave travelling in the x direction and impinging the surface of a fluid layer, its acoustic pressure at the time t can be written as:

$$p(x,t) = Ae^{j\omega(t-kx)} \tag{1}$$

where A is the pressure amplitude, ω is the angular frequency and $k = \omega\left(\frac{\rho}{K}\right)^{1/2}$ is the wavenumber defined as a function of fluid density ρ and bulk modulus K. The related air particle velocity vector is defined as:

$$v(x,t) = \frac{kA}{\rho\omega}e^{j\omega(t-x/c)}. \tag{2}$$

Considering the two equations above, the ratio between pressure and velocity provides the following definition of the characteristic impedance:

$$Z_c = (\rho K)^{1/2} \tag{3}$$

which represents an intrinsic property of the medium for the propagation of plane waves.

The *mechanical impedance* Z_M is used in acoustics to describe fluid load effects provided by a medium upon a vibrating surface. It is defined as the ratio of the applied force over surface velocity and is expressed in Nm/s. The *specific acoustic impedance* Z_S, expressed in Pas/m, is defined as the ratio of sound pressure and particle velocity and is generally used to evaluate reflection and/or transmission of propagating sound waves at the interface between different media. Since continuity condition applies at such interface, it is possible to trace back to the surface impedance and then to the reflection and absorption coefficients of sound absorbing materials, which can be represented, for example, by porous linings placed at the rigid boundaries of untreated rooms.

1.1.2 Energy based metrics: sound Reflection and Absorption coefficients

As mentioned above, when a sound wave hits the surface of an object, incident sound energy is partly re-radiated backwards, partly transmitted and partly dissipated through the object material. Considering the law of conservation of energy, reflected (E_ϱ), transmitted (E_τ) and dissipated (E_δ) energy amounts can be related to the total incident energy E_i by means of the following relationship:

$$E_i = E_\varrho + E_\tau + E_\delta. \tag{4}$$

Normalizing the equation above with respect to E_i yields:

$$1 = \varrho + \tau + \delta, \tag{5}$$

where ϱ, τ and δ are the reflection, transmission and dissipation coefficients, respectively.
Assuming a plane and normally incident sound field upon the surface of a material, its reflection coefficient R can be defined as the ratio of complex sound pressures generated by reflected and incident waves, as follows:

$$R = \frac{p_{ref}}{p_{inc}}. \tag{6}$$

As mentioned, this is a complex quantity which holds in it the phase relationship between incident and reflected waves.

Absorption coefficient describes the effective capacity of a material to absorb sound energy. With reference to the energy balance above, it takes in account not only the actually dissipated energy, but also the sound power transmitted through the material. In light of this, the sound absorption coefficient α can be defined as:

$$\alpha = 1 - \frac{E_\varrho}{E_i} = 1 - |R|^2. \tag{7}$$

As noticeable from the equation above, differently from the reflection coefficient, the absorption coefficient is a real quantity and does not hold phase information about reflected and trasmitted sound waves. On this purpose, such a metric is often used in architectural acoustics application, where such a simplification is more compliant with the type of acoustic analysis of interest in that field. Furthermore, when characterizing the effective sound absorption present in a room, the absorption coefficient may be not completely exhaustive. Hence the need to define the quantity of sound absorbing units, which represent the summation of the effective surface area of absorbing materials, multiplied by their associated absorption coefficients, as follows:

$$S_\alpha = \sum_{i=1}^{n} S_i \alpha_i. \tag{8}$$

2 Specific acoustic impedance of vibrating plates

For an efficient acoustic characterization of panel absorbers, it becomes essential to define appropriate models to predict the mechanical behaviour of plates, since they represent the most typical components of such absorbers. In particular, since practical applications of panel absorbers are mainly concerned with noise control at low frequencies in non-diffuse sound fields, it is convenient to characterize their performance in terms of sound absorption by defining their acoustic surface impedance as a function of frequency. In order to do so, it is necessary to derive the specific acoustic impedance for each single component of the absorber, and primarily for the vibrating plate. Such an impedance can be properly defined once sound pressure loads and velocity distribution over the plate surface are known: on this purpose, it is necessary to model the mechanical behaviour of plates under external loads and investigate the relationships among force, displacement, stress and strain fields.

Nevertheless, an exhaustive mathematical analysis of a vibrating plate modeled as an elastic three-dimensional solid body would imply extremely cumbersome computation, requiring the solution of the differential equation of three dimensional elasticity [3]. Usually, in practical applications, the thickness of such plates is chosen to be much smaller than the other dimensions. On this purpose, it is generally accepted to employ the Kirchhoff's bending theory (also known as "Classical plate theory") [3, 2], which introduces significant simplifications in terms of computational effort still ensuring an accurate modelling of thin plates. Indeed, starting from assumptions which can be considered valid in most cases, this theory allows for the reduction from a three-dimensional to a two-dimensional problem, resulting in a concise derivation of plate governing equations. Once the flexural behaviour of a plate is predicted, and then the pressure loads and velocity distribution over the plate surface are known, it becomes straightforward to calculate its mechanical impedance and then the specific acoustic impedance, which becomes essential for an appropriate acoustic characterization of the whole system.

In light of the above, principles and assumptions at the basis of the Kirchhoff's theory are outlined in the following section, with the aim of providing an exhaustive description of bending wave propagation and free flexural vibration of plates, according to the objectives of this thesis. Starting from that point, analytical models for the computation of specific acoustic impedance of infinite sized, circular and rectangular plates will then be presented for different constraint conditions at the edges.

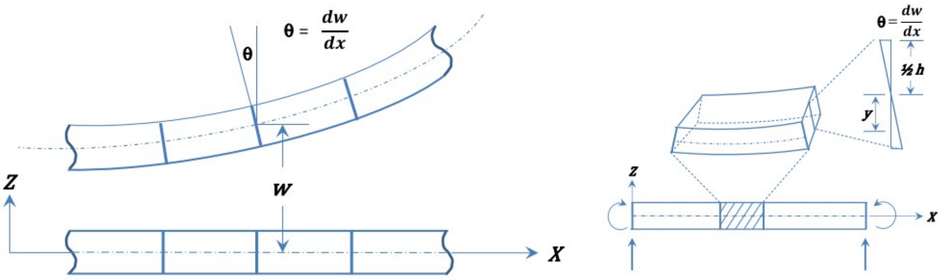

Figure 1: Flexural deformation of a plate according to the Kirchhoff bending theory. From [1], p. 65.

2.1 The Kirchhoff's bending theory for thin plates

As briefly mentioned above, the Kirchhoff's bending theory for thin plates represents a direct application of the theory of elasticity. Indeed, the derivation of the flexural governing equation of thin plates arises from the constitutive, equilibrium and compatibility equations of elasticity, as long as the basic assumptions of the Kirchhoff theory are valid. The main advantage of this theory relies upon the fact that, in most of practical applications, the mechanical behavior of thin plates subjected to external loading is efficiently modeled by a differential equation of fourth order, expressed in terms of the transverse displacement field of the plate middle surface. This simplification allows to circumvent the solution of three-dimensional equations of elasticity, neglecting the shear stresses and leading to a reduced two-dimensional problem.

With reference to Figure 1, assuming a three-dimensional plate lying in the plane xy, with the z axis oriented along the thickness direction, it is possible to state that the simplifications mentioned above are based on the following assumptions:

1. The plate material is homogeneous, isotropic and linear elastic;

2. The plate is initially flat;

3. The thickness of the plate h is small compared to the other characteristic dimensions – at least one tenth of the smallest dimension of the plate;

4. *Hypothesis of small displacements*: the transverse displacements $w(x, y)$ of the midsurface are small compared to the thickness h ($\leq h/10$). A straight line that is normal to the midsurface of the undeformed plate remains straight and normal to the deformed midsurface (see fig. 1)). The slope or rotation angle θ, which is equal to the first derivative of the deflection $\frac{\partial w}{\partial x}$, is very

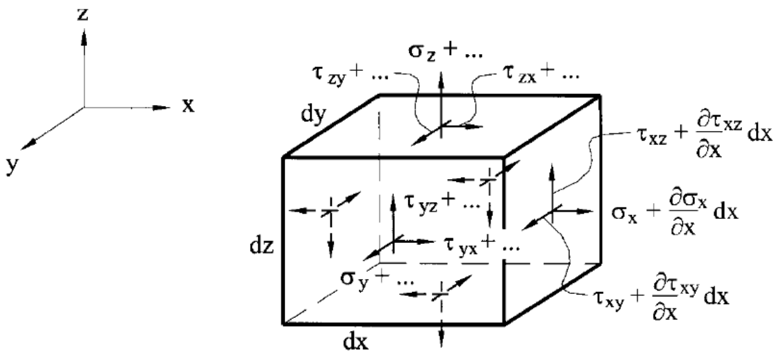

Figure 2: Infinitesimal volume of an elastic body subjected to external loads in equilibrium: a representation of the stress tensor. From [2], par. 1.4.1.

small and its square is negligible compared with unity. In light of this, vertical shear strains γ_{xz}, γ_{yz} and normal strain ε_z can be neglected;

5. The normal stress σ_z in the direction transverse to the plate surface can be neglected, since it is small compared with the other stress components;

6. Holding the hypothesis of small displacements, the midsurface of the plate is assumed to be unstrained during deflections.

The governing equations of plate theory are based on the simplifications arose from these assumptions. Before getting into the details of the derivation, it is worthwhile to provide a brief overview of the theory of elasticity, which constitutes the ground for such process.
When a three-dimensional solid body is excited by external loads, consequent deformations and stresses occur, which depend on the mechanical properties of the material, on its geometry and on the applied loading. As a basic assumption, the body is intended to be linear elastic – namely, the stress-strain relationship is linear –, isotropic and homogeneous – its mechanical properties remain the same through the volume, regardless of direction.

In order to solve the problem of an elastic three-dimensional body subjected to external forces in equilibrium, it is necessary to identify the stress, strain and displacement variables and relate them to appropriate equations. Considering a cuboid infinitesimal volume – shown in Figure 2 – of an elastic body of whatever shape, it is possible to identify for each face of the volume an orthogonal tern of stress components, defined as *normal stresses* (σ_i) and *shear stresses* (τ_{ij}). Those

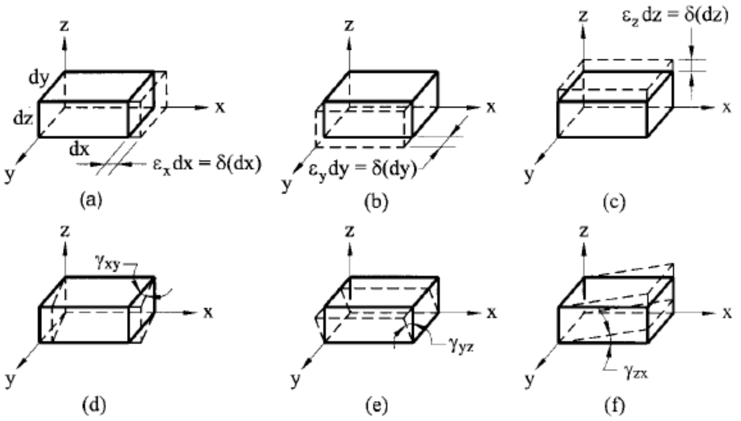

Figure 3: Representation of strain components of the infinitesimal cuboid control volume. - from Ref. [2], par. 1.4.2

stress components form the so called *stress tensor T_s*, defined as:

$$T_s = \begin{pmatrix} \sigma_x & \tau_{xy} & \tau_{xz} \\ \tau_{yx} & \sigma_y & \tau_{yz} \\ \tau_{zx} & \tau_{zy} & \sigma_z \end{pmatrix} \tag{9}$$

which is symmetric due to the *reciprocity law of shear stresses*, which implies that:

$$\tau_{xy} = \tau_{yx} \qquad \tau_{xz} = \tau_{zx} \qquad \tau_{zy} = \tau_{yz}. \tag{10}$$

Hence, only six out of nine stress components result as independent variables.

Similarly to stress components, it is possible to define nine strain vectors with reference to the infinitesimal volume defined above, starting from the assumption that rigid translations and rotations are prevented for the elastic body in question. In particular, referring to figure 3(a), (b), (c), vectors representing the deformation of the volume edges along the coordinate axes are called *normal strains* and can be defined as:

$$\varepsilon_x = \frac{\delta(dx)}{dx} = \frac{\partial u}{\partial x}, \qquad \varepsilon_y = \frac{\delta(dy)}{dy} = \frac{\partial v}{\partial y}, \qquad \varepsilon_z = \frac{\delta(dz)}{dz} = \frac{\partial w}{\partial z}. \tag{11}$$

The remaining three strain vectors – depicted in figure 3(d), (e), (f) – involve not only an edge deformation but also a modification of the angles between the edges in the undeformed configuration. They are called *shear strains* and are defined as:

$$\gamma_{xy} = \frac{\partial u}{\partial y} + \frac{\partial v}{\partial x}, \qquad \gamma_{xz} = \frac{\partial u}{\partial z} + \frac{\partial w}{\partial x}, \qquad \gamma_{yz} = \frac{\partial v}{\partial z} + \frac{\partial w}{\partial y}. \tag{12}$$

As in the case of stress components, strain vectors constitute the three-dimensional symmetric *strain tensor* T_D as follows:

$$T_D = \begin{pmatrix} \varepsilon_x & \frac{1}{2}\gamma_{xy} & \frac{1}{2}\gamma_{xz} \\ \frac{1}{2}\gamma_{yx} & \varepsilon_y & \frac{1}{2}\gamma_{yz} \\ \frac{1}{2}\gamma_{zx} & \frac{1}{2}\gamma_{zy} & \varepsilon_z \end{pmatrix} \tag{13}$$

where, similarly to the case of Eq.10 it holds that

$$\gamma_{xy} = \gamma_{yx} \qquad \gamma_{xz} = \gamma_{zx} \qquad \gamma_{zy} = \gamma_{yz} \,. \tag{14}$$

In light of this, also in this case the independent variables reduce to six out of nine total strain vectors. Consequently, the elastic problem is characterized by fifteen independent variables – namely, six stress components, six strain components and three displacement components.
For each of those variables, the theory of elasticity defines a sufficient number of equations in order to make the elasticity problem statically determinate. Those equations are grouped in three categories: *constitutive equations* (six), *equilibrium equations* (three) and *compatibility equations* (six). For the derivation of the following equations, which is out of the scope of this thesis, please refer to specific scientific literature [3, 2].

The *constitutive equations* express the linear elastic behavior of the material and represent the application of the Hooke's law to a three-dimensional, homogeneous, isotropic and linear elastic body. Such equations are defined as follows:

$$\varepsilon_x = \frac{1}{E}[\sigma_x - \nu(\sigma_y + \sigma_z)] \tag{15}$$

$$\varepsilon_y = \frac{1}{E}[\sigma_y - \nu(\sigma_x + \sigma_z)] \tag{16}$$

$$\varepsilon_z = \frac{1}{E}[\sigma_z - \nu(\sigma_y + \sigma_z)] \tag{17}$$

$$\gamma_{xy} = \frac{1}{G}\tau_{xy} \tag{18}$$

$$\gamma_{xz} = \frac{1}{G}\tau_{xz} \tag{19}$$

$$\gamma_{yz} = \frac{1}{G}\tau_{yz} \tag{20}$$

where E is the Young's modulus, ν is the Poisson's ratio and G is the shear modulus, which are related by the relationship $G = \frac{E}{2(1+\nu)}$.

The *equilibrium equations* constitute a set of three differential equations that describe the equilibrium conditions of an elastic body when subjected to body forces of components F_x, F_y, F_z. Such equations are defined as follows:

$$\begin{aligned}
&\frac{\partial \sigma_x}{\partial x}+\frac{\partial \tau_{xy}}{\partial y}+\frac{\partial \tau_{xz}}{\partial z}+F_x=0\\
&\frac{\partial \sigma_y}{\partial y}+\frac{\partial \tau_{yx}}{\partial x}+\frac{\partial \tau_{yz}}{\partial z}+F_y=0\\
&\frac{\partial \sigma_z}{\partial z}+\frac{\partial \tau_{zx}}{\partial x}+\frac{\partial \tau_{zy}}{\partial y}+F_z=0.
\end{aligned} \tag{21}$$

At last, the *compatibility equations* express the continuity of an elastic body, namely that unstrained plane sections remain plane during deformation and that strain is homogeneous at all locations within the volume of the medium. These equations are obtained by successively differentiating and manipulating Eqs.11 and 12, and can be summarized as follows:

$$\begin{aligned}
&\frac{\partial^2 \varepsilon_x}{\partial y^2}+\frac{\partial^2 \varepsilon_y}{\partial x^2}=\frac{\partial^2 \gamma_{xy}}{\partial x \partial y}\\
&\frac{\partial^2 \varepsilon_z}{\partial x^2}+\frac{\partial^2 \varepsilon_x}{\partial z^2}=\frac{\partial^2 \gamma_{xz}}{\partial x \partial z}\\
&\frac{\partial^2 \varepsilon_y}{\partial z^2}+\frac{\partial^2 \varepsilon_z}{\partial y^2}=\frac{\partial^2 \gamma_{yz}}{\partial y \partial z}
\end{aligned}$$

$$\begin{aligned}
&\frac{\partial}{\partial x}\left[\frac{\partial \gamma_{xz}}{\partial y}+\frac{\partial \gamma_{xy}}{\partial z}-\frac{\partial \gamma_{yz}}{\partial x}\right]=2\frac{\partial^2 \varepsilon_x}{\partial y \partial z}\\
&\frac{\partial}{\partial y}\left[\frac{\partial \gamma_{xy}}{\partial z}+\frac{\partial \gamma_{yz}}{\partial x}-\frac{\partial \gamma_{xz}}{\partial y}\right]=2\frac{\partial^2 \varepsilon_y}{\partial x \partial z}\\
&\frac{\partial}{\partial z}\left[\frac{\partial \gamma_{yz}}{\partial x}+\frac{\partial \gamma_{xz}}{\partial y}-\frac{\partial \gamma_{xy}}{\partial z}\right]=2\frac{\partial^2 \varepsilon_z}{\partial x \partial y}.
\end{aligned}$$

In light of the assumptions introduced at the beginning of this section together with the characteristic equations of the theory of elasticity, it is now possible to derive the governing equation of the classical plate theory, which allows to describe the deflection function $w(x,y)$ of a thin plate subjected to a transversal distributed load $p(x,y)$ – as will be highlighted later on, such a load can be comparable to the mechanical action exerted by the pressure distribution over the upper surface of the plate due to an external sound field.

With reference to Figure 4, consider an infinitesimal volume of a plate with dimensions $dx \times dy$, subjected to a static transverse distributed load per unit area $p(x,y)$. In order to ensure its static equilibrium conditions, the applied pressure $p(x,y)$ must be balanced by the internal stress resultants and couples applied to the midsurface of the element. It is worthwhile to highlight that stress components

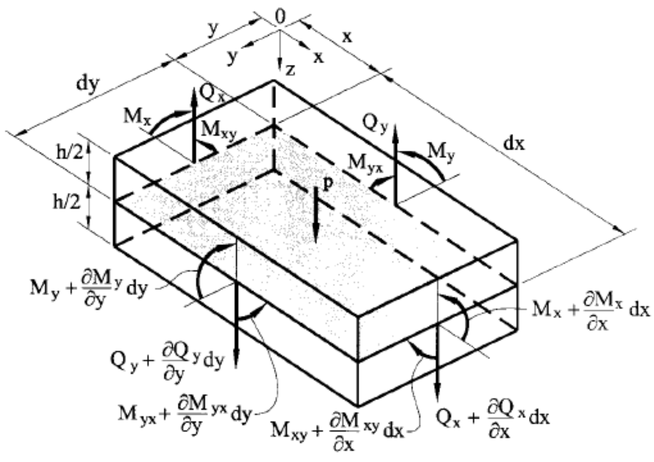

Figure 4: Infinitesimal volume of a plate in equilibrium under the action of external forces and stress resultants and couples. From [2], section 2.3.

σ_x,σ_y,τ_{xy},τ_{yx} vary from point to point through the element volume: nevertheless, due to the smallness of the element, such components can be intended to be as uniformly distributed. Therefore, instead of carrying out a stress analysis by points, it is convenient to introduce the equivalent forces and moments applied to the midsurface of the elements, namely the stress resultants and couples just mentioned. In this way, the three-dimensional stress analysis is reduced to a two-dimensional problem, by only considering the bending of the midsurface of the plate.
In particular, the stress resultants and couples are defined as follows:

- *Shear forces* Q_x, Q_y, which can be expressed as:

$$\left\{ \begin{array}{c} Q_x \\ Q_y \end{array} \right\} = \int_{-h/2}^{h/2} \left\{ \begin{array}{c} \tau_{xz} \\ \tau_{yz} \end{array} \right\} z \, \mathrm{d}z \tag{22}$$

- *Bending moments* M_x, M_y, defined as:

$$\left\{ \begin{array}{c} M_x \\ M_y \end{array} \right\} = \int_{-h/2}^{h/2} \left\{ \begin{array}{c} \sigma_x \\ \sigma_y \end{array} \right\} z \, \mathrm{d}z \tag{23}$$

- *Twisting moments* $M_{xy} = M_{yx}$, expressed as:

$$M_{xy} = \int_{-h/2}^{h/2} \tau_{xy} z \, \mathrm{d}z \tag{24}$$

In light of the above, it is possible to explicit the static equilibrium conditions of the infinitesimal element by means of the following equations:

- *Static equilibrium around z axis:*

$$\frac{\partial Q_x}{\partial x}+\frac{\partial Q_y}{\partial y}+p(x,y)=0 \tag{25}$$

- *Static equilibrium around x axis:*

$$\frac{\partial M_{xy}}{\partial x}+\frac{\partial M_y}{\partial y}-Q_y=0 \tag{26}$$

- *Static equilibrium around y axis:*

$$\frac{\partial M_{yx}}{\partial y}+\frac{\partial M_x}{\partial x}-Q_x=0 \tag{27}$$

  where products of infinitesimal terms have been neglected as terms with a higher order of smallness.

Writing Eqs. 26 and 27 as a function of $Q_y$and Q_x and substituting them into Eq. 25 yields:

$$\frac{\partial^2 M_x}{\partial x^2}+2\frac{\partial^2 M_{xy}}{\partial x \partial y}+\frac{\partial^2 M_y}{\partial y^2}=-p(x,y) \tag{28}$$

which is the *governing equation for the bending of a thin plate*, excited by a uniform transverse load, based on the assumptions of the *Kirchhoff's classical plate theory.* Nevertheless, it is convenient to express Eq. 28 in terms of transverse displacements $w(x,y)$ of the midsurface of the plate: in order to do so, it is necessary to recall the characteristic equations of the theory of elasticity. On this purpose, Eqs. 22, 23 and 24 highlight that the stress resultants and couples are nothing but the integral of the stress components calculated along the thickness h of the plate. Thus, it becomes necessary to define a law of variation of those stress components through the thickness h.

In order to do so, consider the constitutive equations 15-20: as long as the assumption of small displacements is valid, $\varepsilon_z=\gamma_{xz}=\gamma_{yz}=0$ and then Eqs. 17, 19 and 20 can be neglected. Hence, expressing Eqs. 15, 16 and 18 in terms of stress components yields:

$$\begin{cases} \sigma_x=\frac{E}{1-\nu^2}(\varepsilon_x+\nu\varepsilon_y) \\ \sigma_y=\frac{E}{1-\nu^2}(\varepsilon_y+\nu\varepsilon_x) \\ \tau_{xy}=G\gamma_{xy} \end{cases} . \tag{29}$$

Referring to the schematization reported in Figure 1 and bearing in mind the assumption of small displacements, the strain components ε_x, ε_y and γ_{xy} can be defined as:

$$\begin{aligned}\varepsilon_x &= -z\frac{\partial}{\partial x}\left(\frac{\partial w}{\partial x}\right) = -z\frac{\partial^2 w}{\partial x^2}\\ \varepsilon_y &= -z\frac{\partial}{\partial y}\left(\frac{\partial w}{\partial y}\right) = -z\frac{\partial^2 w}{\partial y^2}\\ \gamma_{xy} &= -2z\frac{\partial^2 w}{\partial x\partial y}\end{aligned} \tag{30}$$

where the second derivative terms $\frac{\partial^2 w}{\partial x^2}$, $\frac{\partial^2 w}{\partial x^2}$ and $\frac{\partial^2 w}{\partial x\partial y}$ represent the curvature of the midsurface along the axes x, y and the twisting curvature with respect to the x and y axes, respectively.
Substituting Eqs. 30 into Eqs. 29 and then into Eqs. 26 and 27 yields:

$$\begin{aligned}M_x &= -D\left(\frac{\partial^2 w}{\partial x^2}+\nu\frac{\partial^2 w}{\partial y^2}\right)\\ M_y &= -D\left(\frac{\partial^2 w}{\partial y^2}+\nu\frac{\partial^2 w}{\partial x^2}\right)\\ M_{xy} &= -D(1-\nu)\frac{\partial^2 w}{\partial x\partial y}.\end{aligned} \tag{31}$$

where $D = \frac{Eh^3}{12(1-\nu^2)}$ is the *flexural stiffness* of the plate.

Substituting Eqs. 31 into Eq. 28 yieds:

$$\left(\frac{\partial^4 w}{\partial x^4}+2\frac{\partial^4 w}{\partial x^2\partial y^2}+\frac{\partial^4 w}{\partial y^4}\right)D = p(x,y) \tag{32}$$

which is a fourth order linear partial differential equation having constant coefficients and represents the *static governing equation for the deflection of thin plates* subjected to distributed loads, which is expressed in terms of the transverse displacement of the plate midsurface. Please note that Eq. 32 does not take in account for any dynamic effect on the plate motion. Indeed, the applied external loads are intended to be time-invariant.
Nevertheless, in engineering applications, it is often necessary to introduce the dynamic effects due to time-dependent external forces. These forces can be either *harmonic* – in the case they are periodic forces – or *transient* - randomly time-dependent. In order to obtain an exhaustive mathematical model of the dynamic case, but still holding the validity of Kirchhoff's assumptions, it is necessary to introduce a dynamic governing equation for the forced deflection of thin plates. In order to do so, it is possible to integrate the static case of Eq. 32 by introducing

the following extensions:

- the deflection terms $w(x,y,t)$ and the applied external loads $p(x,y,t)$ are now considered as space and time dependent;
- according to the D'Alembert principle, *inertial forces* are taken in account. These represent the effective forces resulting from the accelerations of the plate mass. They are space and time dependent and can be written as:

$$m\frac{\partial^2 w}{\partial t}(x,y,t) \tag{33}$$

  where $m = \varrho h$ is the surface mass of the material.

Leaving aside for the moment the introduction of additional damping forces, it is now possible to write the differential equation of forced, undamped motion on thin plates subjected to dynamic loads, expressed as follows:

$$D\nabla^4 w(x,y,t) + m\frac{\partial^2 w}{\partial t}(x,y,t) = p(x,y,t). \tag{34}$$

This equation represents a significant simplification of the elastic problem, by reducing its dimensions to a two-dimensional case and taking in account for dynamic effects on the plate motion due to external loads. Together with the static governing equation (Eq. 32), it represents the starting point for the derivation of the velocity field of the plate during deflection and the consequent determination of the specific acoustic impedance functions of thin plates. Such a derivation will be addressed in the following subsections for different boundary conditions of the plate.

2.2 Infinite sized plates

In the case of a homogeneous plate of infinite extent lying in the plane xy and subjected to a spatially distributed plane wave pressure $p(x,y,t)$, its specific acoustic impedance can be defined as:

$$Z_s = \frac{p(x,y,t)}{v(x,y,t)} \tag{35}$$

where $v(x,y)$ is the velocity distribution over the upper surface of the plate. In this case, the response and the excitation load must refer to the same frequency and spatial distribution, as highlighted by Cremer et al. [9]. Considering the above defined equation of motion of a thin plate (Eq. 34), and expressing it in terms of the harmonic velocity $v = j\omega w$, yields:

$$\nabla^4 v(x,y) - k_B^4 v(x,y) = \frac{j\omega}{D} p(k_x,k_y) e^{-jk_x x} e^{-jk_y y} \tag{36}$$

where $k_B^4 = \frac{\omega^2 m}{D}$ is the *bending wavenumber* of waves propagating through the plate and $p(x,y) = p(k_x,k_y)e^{-jk_x x}e^{-jk_y y}$ has been written as an harmonic space dependent function.
Since the plate is infinite and homogeneous, and holding the assumption for the definition of Eq. 35, $v(x,y)$ can be expressed as:

$$v(x,y) = v(k_x,k_y)e^{-jk_x x}e^{-jk_y y}. \tag{37}$$

In light of this, Eq. 36 reads

$$[(k_x^2 + k_y^2)^2 - k_B^4]v(k_x,k_y) = -\frac{j\omega}{D} p(k_x,k_y) \tag{38}$$

and consequently, the impedance Z_s can be expressed as:

$$Z_s = j\omega m \left[1 - \frac{(k_x^2 + k_y^2)^2}{k_B^4}\right]. \tag{39}$$

2.3 Circular plates

In the case of circular plates subjected to uniform loads, it is convenient to express Eq. 34 in polar coordinates, by applying the following relationships:

$$\begin{aligned} x &= r\,cos\varphi \\ y &= r\,sin\varphi \\ r &= \sqrt{x^2 + y} \\ \varphi &= atan\left(\frac{y}{x}\right) \end{aligned}$$

where, with reference to Figure 5, r and φ represent the polar coordinates of a point of the plate having cartesian coordinates (x,y).

The derivation of Eq. 34 in polar coordinates, which is reported in specific literature [3, 2, 10, 11], leads to the following relationship:

$$\nabla_r^4 w(r,\varphi) - k_B^4 w(r,\varphi) = \frac{p(r,\varphi)}{D}. \tag{40}$$

Integrating the equation above and expressing it in terms of linear displacements

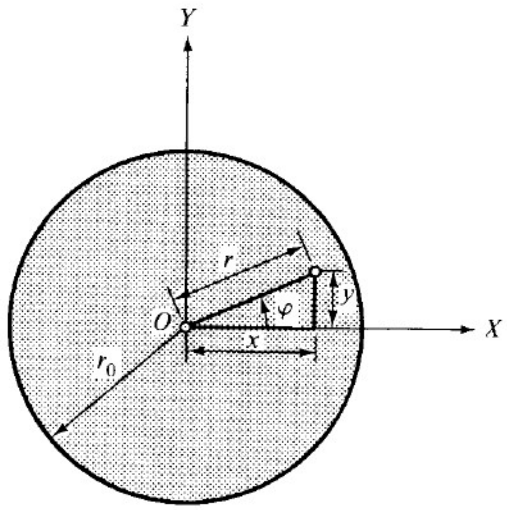

Figure 5: Relationship between Cartesian and polar coordinates in a circular plate. From [3], section 1.4.

w, reads [12, 13]:

$$w(r) = -\frac{p(r)}{k_B^4} + AJ_0(k_B^4 r) + BI_0(k_B^4 r) \tag{41}$$

where J_0 and I_0 are the angular and modified Bessel's functions of the first kind of order zero, respectively, and the coefficients A and B are determined from the boundary conditions.

Eq. 41 is a solution of the partial differential equation 40, obtained by assuming a uniform pressure distribution over the plate surface and considering only the axisymmetric modal bending of the circular plate. The latter assumption is generally valid when the applied loading and the edge constraints are uniform and independent of the angular coordinate φ. In this way, the deflection of the plate and the related stresses will only depend on the radial coordinate r.

By applying the appropriate boundary conditions to Eq. 41, the governing equations for the deflection of circular plates with different constraint conditions can be derived, as will be highlighted in the following subsections.

2.3.1 Simply supported edges

The simply supported constraint condition of a plate implies that both displacement w and radial moment M_r must be zero at the edges. This is expressed by the following homogeneous boundary conditions:

$$\begin{cases} w(r=a) = 0 \\ \left.\frac{\partial^2 w}{\delta r^2}\right|_{r=a} + \frac{\nu}{r}\left.\frac{\partial w}{\delta r}\right|_{r=a} = 0 \end{cases} \tag{42}$$

where a is the length of the radius.
Applying the relationships above to Eq. 41, it leads to to the following expressions for the constants A and B [13]

$$A = \frac{p}{k_B^4 D} \cdot \frac{\left(I_0^{''}(k_B a) + \frac{\nu}{a} I_0^{'}(k_B a)\right)}{\Delta}$$
$$B = -\frac{p}{k_B^4 D} \cdot \frac{\left(J_0^{''}(k_B a) + \frac{\nu}{a} J_0^{'}(k_B a)\right)}{\Delta} \tag{43}$$

where $\Delta = J_0\left(I_0^{''}(k_B a) + \frac{\nu}{a} I_0^{'}(k_B a)\right) - I_0\left(J_0^{''}(k_B a) + \frac{\nu}{a} J_0^{'}(k_B a)\right)$ and the superscript of the Bessel's functions indicate respectively the first and second order derivative. Assuming a uniform pressure load $p(r)$ acting on the surface of the plate, the *mechanical impedance* Z_m can be calculated by considering the following force-velocity ratio:

$$Z_m = \frac{\iint_S p(r)\,\mathrm{d}S}{j\omega \frac{1}{S} \iint_S w(r)\,\mathrm{d}S} \tag{44}$$

where S is the surface area of the plate and the term at denominator represents the time derivative of the mean transverse displacement $w(r)$ over the surface of the plate. Holding the validity of the above assumption and stated that the *specific acoustic impedance* Z_s can be written as a function of the mechanical impedance ($Z_s = Z_m/S$), the following expression of the *surface averaged specific acoustic impedance* $\langle Z_s \rangle$ of a circular simply supported plate subjected to static uniform loads can be obtained by substituting Eqs. 43 into Eq. 44 with successive rearrangements [13]:

$$\langle Z_s \rangle = \left[\frac{j\omega}{k_B^4 D} \frac{\frac{2}{k_B^4 a}\left\{\left(I_0^{''} + \frac{\nu}{a} I_0^{'}\right) J_1 - \left(J_0^{''} + \frac{\nu}{a} J_0^{'}\right) I_1\right\} - \Delta}{\Delta} \right]^{-1} \tag{45}$$

where the argument of the Bessel's functions is still $k_B a$.

2.3.2 Clamped edges

The boundary conditions of a plate clamped all around edges imply that both transverse displacements and rotations are zero at the edges. The corresponding boundary conditions for Eq. 41 reads:

$$\begin{cases} w(r=a)=0 \\ \frac{\partial w}{\delta r}\Big|_{r=a}=0 \end{cases} \tag{46}$$

where a is the radius of the plate. The application of conditions 46 to Eq. 41 yields the following constants A and B [12, 13]:

$$\begin{aligned} A &= \frac{p}{k_B^4 D} \cdot \frac{I_1(k_B a)}{J_0(k_B a) I_1(k_B a) + J_1(k_B a) I_0(k_B a)} \\ B &= \frac{p}{k_B^4 D} \cdot \frac{J_1(k_B a)}{J_0(k_B a) I_1(k_B a) + J_1(k_B a) I_0(k_B a)}\,. \end{aligned} \tag{47}$$

Similarly to the case of simply supported plates, referring to Eq. 44, by means of subsequent arrangements it is then possible to derive the following expression of the *surface averaged specific acoustic impedance* $\langle Z_s \rangle$ of a circular clamped plate subjected to stationary loads:

$$\langle Z_s \rangle = -j\omega\varrho h \cdot \frac{I_1(k_B a) J_0(k_B a) + J_1(k_B a) I_0(k_B a)}{I_1(k_B a) J_2(k_B a) - J_1(k_B a) I_2(k_B a)}\,. \tag{48}$$

2.4 Rectangular plates

As mentioned in the foregoing section, the governing equations for the deflection of thin plates (Eqs. 32, 34) are partial differential equations of the fourth order having constant coefficients. Generally, in the case of rectangular plates, different methods are available to solve such equations and, depending on the shape of the plate and its boundary conditions, they may be more or less computationally expensive.
As reported by Szilard [3], the *rigorous classical approaches* aimed to solve the governing equations for displacements in the differential form, can be summarized as follows:

- *closed form solutions*: such solutions are very rare and generally cumbersome in the case of plates with complex boundary conditions. Nevertheless, few cases are available when this boundary value problem can be solved directly ([3]);

- *superposition principle*: this method has been used by several authors for the analysis of plate vibration ([14, 15, 16, 17]). It consists in superimposing the solution of the homogeneous governing equation with a particular solution of the same general equation, depending on the boundary condition;

- *double trigonometric series solutions*: they were proposed by Navier with reference to the case of a rectangular simply supported plate. This kind of approach reduces the solution of a differential equation to an algebraic solution. A drawback lies in the slow convergence of the method in the case of concentrate and discontinuous loads;
- *single series solutions*: this approach shows a considerably faster convergence with respect to other methods. However, it is limited to the case when the plate has two opposite simply supported sides and the shape of the distributed load is constant in the direction parallel to the two other edges.

Alongside the rigorous approaches introduced above, *energy methods* are available which are based on the application of the virtual work principle. Although they represent an approximation, such methods are more generally applicable to plates of various shapes and boundary conditions. Moreover, their application is easier with respect to classical methods when dealing with rectangular plates.
Several energy methods were introduced over time by Rayleigh [18], Ritz, Galerkin and Vlasov, to mention a few, which also constitute the basis for finite element analysis. Such methods have been extensively employed in plate analysis by several authors, such as Warburton [19], who resorted to the Rayleigh method to derive frequency expressions for all modes of vibrating plates subjected to various boundary conditions as well as possible combinations of them.

In particular, energy methods are also known as *variational methods,* since they lie on an alternative mathematical approach to elastic problems, called *calculus of variation.* Specifically, the determination of the plate displacement field function (but either stress or strain fields) can be reduced to an integral of the function itself, called *functional*: the displacement field can then be retrieved by assuming conditions of extremum of this functional. Such conditions can be expressed by postulates also referred to as *variational principles.* In the elastic analysis of structures, assuming that a system is conservative and holding the validity of the small-deflection theory, such a variational principle can be successfully represented by the *Principle of Minimum Potential Energy,* introduced by Lagrange, which states that

> *among all admissible configurations of an elastic body, the actual configuration (that satisfies static equilibrium conditions) makes the total potential energy Π stationary with respect to all small admissible virtual displacements. For stable equilibrium, Π is a minimum* [2].

This principle can be intended as a specialization of the *principle of virtual work.* In particular, the potential energy Π of an elastic system can be written as

$$\Pi = U + V \tag{49}$$

where:

– $U = -W_i$ is the potential energy of internal forces of the system and it is equal to the negative work of internal forces;

– $V = -W_e$ is the potential energy of external forces of the system and it is equal to the negative work of external forces.

By applying the virtual work principle as

$$\delta W = \delta W_i + \delta W_e = 0 \tag{50}$$

it follows that

$$\delta W = -\delta U - \delta V = -\delta(U + V) = \delta \Pi = 0 \tag{51}$$

where $\delta\Pi$ is the variation of the total potential Π due to the introduction of virtual displacements compatible to the elastic system in question. This relationship provides a mathematical expression of the principle of minimum potential energy. In particular, the expression $\delta\Pi = 0$ mathematically means that the function Π has a point of minimum or maximum. In the case of the elastic theory problem, which is based on the assumption of small displacements, the only possible configuration of equilibrium is that stable: in light of this, the potential energy Π has to be a minimum. Therefore, the aim of the variational methods introduced above is to find out, among a set of admissible functions, the solution that minimizes the total potential energy.

This principle can be used to obtain approximate solutions of structural mechanics problems, in particular plate bending problems with complex boundary conditions. On this purpose, for the scope of this thesis, one of the above mentioned variational methods, namely the Vlasov's method, has been employed in order to derive frequency expressions for the deflections of rectangular plates either clamped or simply supported at the edges and, consequently, their relative specific acoustic impedance functions.

2.4.1 Impedance of simply supported and clamped plates: an application of Vlasov's method

As mentioned above, the dynamic response of vibrating rectangular plates, subjected to various and complex boundary conditions, can be investigated by means of energy methods. On this purpose, the application of Vlasov's method to the case of a clamped rectangular plate subjected to different types of loads has led to the derivation of an analytical expression of its specific acoustic impedance, as highlighted by authors such as Sung and Jan [20], Huang et al., [21] and Jiménez et al. [22]. Such a method represents an extension of the Galerkin's method, the discussion of which is out of the scope of this thesis, although it can be readily found in literature [3, 2].

Let us consider an undamped rectangular thin plate lying in the xy plane and subjected to a harmonic concentrated load $p_e(x,y,t)$, oriented along the z axis and applied at the point (ξ,η). The governing equation for the deflections of such a plate is represented by Eq. 34 that, for the case in question, can be written as:

$$D\nabla^4 w(x,y,t)+m\frac{\partial^2 w(x,y,t)}{\partial t^2}=p_e(x,y,t) \tag{52}$$

where $w(x,y,t)$ is the transverse displacement of the midsurface of the plate, and the remaining quantities hold the same meaning as in Eq.34. Since $w(x,y,t)$ and $p_e(x,y,t)$ are harmonic quantities, they can be expressed as:

$$w(x,y,t)=W(x,y)e^{j\omega t}, \qquad p_e(x,y,t)=P(x,y)e^{j\omega t}. \tag{53}$$

Introducing Eq. 53 into Eq. 52 yields:

$$D\nabla^4 W(x,y)-m\omega^2 W(x,y)-P(x,y)=0. \tag{54}$$

The transverse displacement ad load functions can be expanded by eigenfunctions, as follows:

$$\begin{aligned} W(x,y) &= \sum_{m=1}^{\infty}\sum_{n=1}^{\infty} W_{mn}(x,y)\phi_{mn}(x,y) \\ P(x,y) &= \sum_{m=1}^{\infty}\sum_{n=1}^{\infty} P_{mn}(x,y)\psi_{mn}(x,y) \end{aligned} \tag{55}$$

where, the terms ϕ_{mn} and ψ_{mn} can be further expanded by using separation of variables, as:

$$\phi_{mn}=\psi_{mn}=X_m(x)Y_n(y) \tag{56}$$

the functions $X_m(x)$ and $Y_n(y)$ being orthogonal functions which satisfy the boundary conditions of a beam subjected to transverse deflection. Referring to the Fourier series expansion of $P(x,y)$ (Eq. 55), the constant P_{mn} can be written as a function of $X_m(x)$ and $Y_n(y)$ as follows:

$$P_{mn} = \frac{\int_0^a \int_0^b P(x,y) X_m(x) Y_n(y)\,\mathrm{d}x\mathrm{d}y}{\int_0^a \int_0^b X_m^2(x) Y_n^2(y)\,\mathrm{d}x\mathrm{d}y} \tag{57}$$

where a and b represent the side lengths of the plate. Recalling the principle of virtual work, it is possible to state that a system is in equilibrium if the work done by all the elementary forces acting through kinematically admissible displacements equals zero. For the case in question, the elementary forces are represented by the left-hand term of Eq. 54, which can be defined as an intensity of an unbalanced loading acting upon the surface area A of the plate. On the other hand, infinitesimal displacements δW, admissible with the bending of a thin plate can be defined as:

$$\delta W = \sum_{i=1}^{\infty} \sum_{k=1}^{\infty} \delta W_{ik} \phi_{ik}(x,y) \tag{58}$$

and, in light of Eqs. 54 and 58, the principle of virtual work can be expressed by means of the following Galerkin equation [2]:

$$\int_0^b \int_0^a [D\nabla^4 W(x,y) - m\omega^2 W(x,y) - P(x,y)]\delta W\,\mathrm{d}x\mathrm{d}y = 0\,. \tag{59}$$

By substituting Eq. 55 into Eq. 59 yields:

$$\begin{aligned} D\sum_{m,i}^{\infty}\sum_{n,k}^{\infty} W_{mn} \int_0^b \int_0^a \phi_{ik} \nabla^4 \phi_{mn}\,\mathrm{d}x\mathrm{d}y \\ -m\omega^2 \sum_{m,i}^{\infty}\sum_{n,k}^{\infty} W_{mn} \int_0^b \int_0^a \phi_{ik} \phi_{mn}\,\mathrm{d}x\mathrm{d}y \\ -\sum_{m,i}^{\infty}\sum_{n,k}^{\infty} P_{mn} \int_0^b \int_0^a \phi_{ik} \psi_{mn}\,\mathrm{d}x\mathrm{d}y = 0\,. \end{aligned} \tag{60}$$

Introducing Eqs. 56-57 and taking in account for the orthogonality properties of functions $X_m(x)$ and $Y_n(y)$, defined as follows [20]:

$$\left.\begin{aligned} \int_0^a X_p(x) X_q(x)\,\mathrm{d}x = \int_0^a X_p''(x) X_q''(x)\,\mathrm{d}x = 0 \\ \int_0^b Y_p(y) Y_q(y)\,\mathrm{d}y = \int_0^b Y_p''(y) Y_q''(y)\,\mathrm{d}y = 0 \end{aligned}\right\} \text{if}\, p \neq q\,. \tag{61}$$

Eq. 60, by successive manipulations, becomes:

$$\begin{aligned} & D\sum_m\sum_n W_{mn}(I_1I_2+2I_3I_4+I_5I_6)+ \\ -m\omega^2\sum_m\sum_n W_{mn}I_2I_6 = & \sum_m\sum_n\int_0^b\int_0^a P(x,y)X_mY_n\,\mathrm{d}x\mathrm{d}y \end{aligned} \tag{62}$$

where

$$\begin{aligned} I_1 &= \int_0^a X_m^{(4)}X_m\,\mathrm{d}x\,, & I_2 &= \int_0^b Y_n^2\,\mathrm{d}y\,, \\ I_3 &= \int_0^a X_m''X_m\,\mathrm{d}x\,, & I_4 &= \int_0^b Y_n''Y_n\,\mathrm{d}y\,, \\ I_5 &= \int_0^b Y_n^{(4)}Y_n\,\mathrm{d}y\,, & I_6 &= \int_0^a X_m^2\,\mathrm{d}x\,. \end{aligned} \tag{63}$$

Rearranging Eq. 62, the displacement field at a single modeshape W_{mn}can be written as

$$W_{mn} = \frac{\int_0^b\int_0^a P(x,y)X_mY_n\,\mathrm{d}x\mathrm{d}y}{D(I_1I_2+2I_3I_4+I_5I_6)-m\omega^2I_2I_6} \tag{64}$$

and, accounting for Eq. 55, the dynamic response of a plate subjected to a harmonic transverse load can be expressed as

$$W(x,y) = \sum_m^\infty\sum_n^\infty \frac{\int_0^b\int_0^a P(x,y)X_mY_n\,\mathrm{d}x\mathrm{d}y}{D(I_1I_2+2I_3I_4+I_5I_6)-m\omega^2I_2I_6}X_m(x)Y_n(y)\,. \tag{65}$$

Shape functions $X_m(x)$ and $Y_n(y)$ can be chosen as linearly independent sets of quasi-orthogonal functions satisfying the boundary conditions of the plate: specifically, they are represented by the eigenfunctions of vibrating beams of length equal to the sides of the plate. Solving the differential equation of motion of a vibrating beam [20] leads to the following set of eigenfunctions:

- in the case of a beam simply supported at both ends, one obtains:

$$X_m(x) = sin\left(\frac{m\pi x}{a}\right), \qquad Y_n(y) = sin\left(\frac{n\pi y}{b}\right) \tag{66}$$

  where m and n represent the modal indices of the beam modeshapes;

- in the case of clamped boundaries, it reads:

$$X_m(x) = G\left(\frac{\lambda_m x}{a}\right) - \left[\frac{G(\lambda_m)}{H(\lambda_m)}\right] H\left(\frac{\lambda_m x}{a}\right) \tag{67}$$

$$Y_m(y) = G\left(\frac{\lambda_n y}{b}\right) - \left[\frac{G(\lambda_n)}{H(\lambda_n)}\right] H\left(\frac{\lambda_n y}{b}\right) \tag{68}$$

where the functions

$$\begin{aligned} G(u) &= cosh(u) - cos(u) \\ H(u) &= sinh(u) - sin(u) \end{aligned} \tag{69}$$

λ_m and λ_n satisfying the following relationship:

$$cosh(\lambda)cos(\lambda) = 1\,. \tag{70}$$

Eq. 69 can be solved by means of root-finding algorithms such as Muller's [23] or Newton-Raphson methods [24].

Once the transverse displacement function of the plate has been derived, it is possible to define a surface averaged frequency expression of its specific acoustic impedance. Recalling its definition as a pressure-velocity ratio, it can be written as:

$$\begin{aligned} \langle Z_s \rangle &= \frac{\int_0^b \int_0^a p_e(x,y,t)\,\mathrm{d}x\mathrm{d}y}{\bar{v}(t)S} \\ &= \frac{\int_0^b \int_0^a p_e(x,y,t)\,\mathrm{d}x\mathrm{d}y}{\frac{\partial w(t)}{\partial t}S} \\ &= \frac{\int_0^b \int_0^a P(x,y)\,\mathrm{d}x\mathrm{d}y}{j\omega \bar{W}(x,y)S} \end{aligned} \tag{71}$$

where $S = ab$ is the surface area of the plate, $\bar{v}$ and $\bar{W}$ are the surface averaged velocity and displacement of the plate, respectively. Introducing the displacement field $W(x,y)$ as defined in Eq.65, the averaged specific acoustic impedance $\langle Z_s \rangle$

reads:

$$\langle Z_s \rangle = \frac{\int_0^b \int_0^a P(x,y)\,\mathrm{d}x\mathrm{d}y}{j\omega \left\{ \int_0^b \int_0^a \left[\sum_m^\infty \sum_n^\infty \frac{\int_0^b \int_0^a P(x,y) X_m Y_n \,\mathrm{d}x\mathrm{d}y}{D(I_1 I_2 + 2 I_3 I_4 + I_5 I_6) - m\omega^2 I_2 I_6} X_m(x) Y_n(y) \right] \mathrm{d}x\mathrm{d}y \right\}} . \quad (72)$$

This expression is generally valid for rectangular plates and can be suitably adapted depending on the edge constraint conditions, by introducing proper definitions of X_m and Y_n functions. Besides the simply supported and clamped cases of Eqs. 66-68, more complex boundary conditions can be introduced by resorting to the eigenfunctions for uniform beams reported in literature by several authors, such as Szilard [3].

3 Acoustic surface impedance of panel-cavity coupled resonators

Complex frequency expressions of specific acoustic impedance of panel absorbers have been widely proposed in literature. Starting from the simplest configuration of a panel-cavity system without porous layer, one of the most common approaches lies on the schematization as a single-degree of freedom (SDOF) mass-spring oscillator. This approximate model, based on lumped parameters equations, has been discussed by Cox [4], and Kuttruff [25] in their textbooks, where the normal acoustic impedance of plate-cavity coupled systems was obtained by means of electrical analogies, accounting for panel resistance, inertance and air cavity acoustic compliance. According to this, resonance frequencies are related to the only plate surface mass and bulk stiffness of the air cavity. Alongside to this models, a thorough analytical expression of the acoustic impedance of finite-sized and edge-clamped panel absorbers was provided by Ford and McCormick [26], accounting for mass, flexural stiffness, and internal damping of the panel by solving the equation of motion of a clamped plate for the first four eigenmodes. The resulting averaged surface impedance was determined by applying the virtual work principle, considering the potential and kinetic energies of the panel and the potential energy of the backing air cavity. The effect of placing a porous material into the cavity was investigated and experimentally validated along with the developed surface impedance function. However, although in the general formulation of panel potential and kinetic energies they accounted for rectangular plates, the matrix solution proposed seems to work only for square panels. This formulation was adopted by Frommhold et al. [27], who investigated the sound absorption performance of a flexible square plate backed by a honeycomb structure of Helmholtz resonators. In light of the above, an extension to rectangular plates is necessary, due to their frequent employment in room acoustics treatment. In addition, the shape of the plate, alongside to its surface extension, can have a significant impact on the resulting eigenvalues of the flexural modes.

3.1 Approximate Impedance models

As mentioned above, panel absorbers are generally composed of an impervious flexible plate backed by a sealed air cavity, which must be narrow enough to ensure an adequate bulk stiffness, namely preventing transverse acoustic modes occurring within its volume. Usually, the cavity can be partially filled with a layer of porous material to provide additional damping to the fundamental resonance of the coupled

system and broadening the range around the maximum absorption frequency. In light of this, sound energy is dissipated by means of either flexural damping – due to the panel bending – and to thermoviscous losses occurring throughout the porous layer. In several cases, such a system has been modelled as a single degree of freedom mass-spring resonator: in this system, the panel mass is supposed to vibrate against a spring constituted by the air stiffness of the cavity. Changing parameters such as the mass density of the plate or the cavity depth will influence the resonance frequency where maximum absorption occurs.
Simple design equations were derived by adding plate resistance and mass terms to the surface impedance of the rigid backed air cavity. The latter impedance was derived by applying the transfer matrix method assuming a plane wave normal incidence upon the surface of such a layer. In light of this, the surface impedance of the rigidly backed air cavity reads:

$$Z_{s1} = -jZ_c cot(k_0 d) \tag{73}$$

where $Z_c = \rho_0 c$ is the characteristic impedance, $k_0$is the wavenumber and d is the depth of the air layer. By adding in series the resistance (r_m) and the mass ($j\omega m$) terms of the plate, it becomes:

$$Z_{s2} = r_m - j\left[\omega m - Z_c cot(k_0 d)\right]. \tag{74}$$

Assuming the cavity to be narrow enough to ensure that $kd \ll 1$, the resonance frequency of the system can be calculated when the imaginary part of Eq. 74 vanishes, leading to the following expression:

$$f_{res} = \frac{c}{2\pi}\sqrt{\frac{\rho_0}{md}}. \tag{75}$$

This formulation has also been integrated with the application of the transfer matrix method to take in account for the possible presence of a porous layer to partially fill the cavity. With reference to Figure 6, the porous layer is assumed to be adjacent to the rigid backing of the absorber. The specific acoustic impedance of such a multi-layered system can be calculated according to the impedance translation theorem, reported by Allard et al. [28]. Starting from the assumption of plane normal incidence and locally reactive fluid media, the specific acoustic impedance at the interface point M_i between layers $(i-1)$ and $(i+1)$ can be calculated as follows:

$$Z(M_i) = Z_{c(i-1)} - \frac{jZ(M_{i-1})cotg(k_{i-1}d_{i-1}) + Z_{c(i-1)}}{Z(M_{i-1,bot})} \tag{76}$$

where $Z_{c(i-1)}$,k_{i-1}, d_{i-1} are respectively the characteristic impedance, the complex wavenumber and the thickness of the $(i-1)$ layer. $Z(M_{i-1,bot})$ is the impedance at the bottom end of the $(i-1)$ layer. In the case of the multi-layered system shown in Figure 6, considering that $Z(M_i)$ is infinite at the rigid end, the impedance at the interface between the porous and air layers is calculated by reducing Eq.76 to:

$$Z(M_2) = -jZ_{c1}cot(k_1d_1) \tag{77}$$

where d_1 is the thickness of the porous layer and Z_{c1} and k_1 are calculated adopting the Delany-Bazley-Miki model [29]. Due to continuity conditions, $Z(M_2) = Z(M_3)$ and $Z(M_4)$ can be then calculated by using Eq. 76. In light of this, the surface averaged impedance $\langle Z_s \rangle$ of the whole panel absorber is obtained by coupling in series the impedance $Z(M_4)$ to the panel mass and resistance terms, according to Eq. 74. Nevertheless, approximate design equations are often inaccurate due to their underlying physical assumptions. Firstly, pistonic motion of the plate is assumed: in light of this, higher order flexural modes of the plate are not taken in account as well as the finite size of the sample which, as will be outlined, has a relevant effect on the resulting resonances of the system, implying absorption peaks to be significantly shifted in frequency with respect to the SDOF simplified solution. This has been highlighted by Cox [4] who compared analytical results against impedance measurements carried out in a Kundt's tube of large cross section (Figure 7). Further uncertainty arises in the determination of the panel resistance term: energy losses due to either the internal damping of the panel material or to mechanical friction occurring at the edges are not clearly separated, highlighting the need for a more detailed formulation.

3.2 Acoustic-structure coupling of cavity backed plates by virtual work principle

The limitations of the approximate model presented above have been partially overcome in a study carried out by Ford and McCormick [26]. They developed a frequency expression of the normal acoustic impedance of a square panel absorber, taking in account for the finite size and consequently the modal behavior of the plate, together with the effect provided by the air cavity. Panel material damping and the effects of introducing a porous material into the cavity were also investigated. Starting from the equation of motion of a flexible, clamped square panel, they applied the principle of virtual work in order to calculate the average surface velocity of the coupled system for a single mode. Considering the first four plate eigenmodes, they simultaneously solved those equations by the use of matrices,

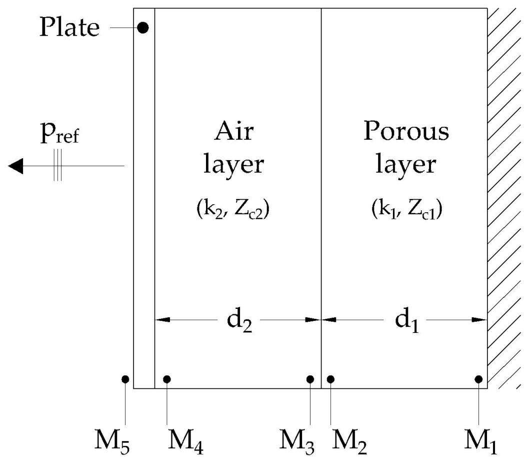

Figure 6: Stratigraphy of a panel absorber with a porous-air multilayered backing.

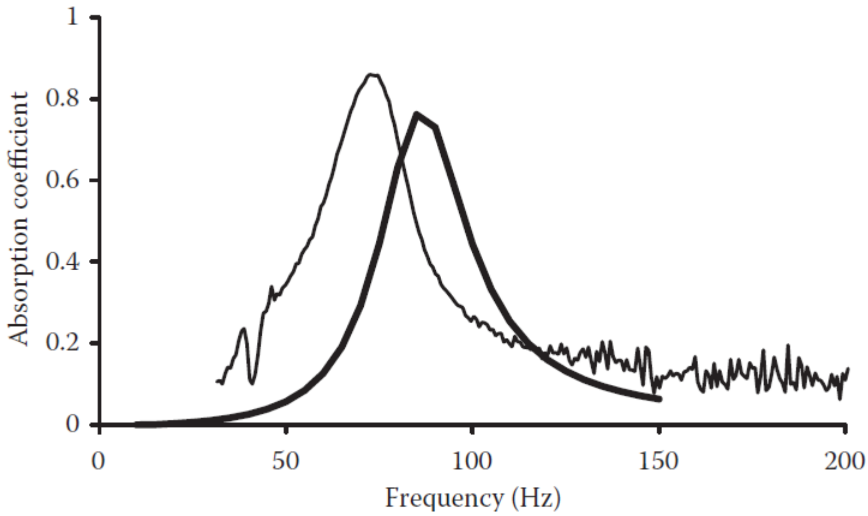

Figure 7: —— Measured and ▬▬ predicted normal incidence absorption coefficient for a commercial membrane absorber. - from [4], par. 7.2.1

and then calculating the average surface impedance, known the pressure.
In particular, starting from the assumption of a thin plate, they calculated the displacement field over the panel surface by superimposing the eigenmode functions of a double clamped beam, as follows:

$$w = \sum_m \sum_n \phi_{mn} f_m(x) g_n(y) \tag{78}$$

where ϕ_{mn} is the maximum displacement occurring over the panel surface and $f_m(x)$ and $g_n(y)$ are the equations of double clamped beams along x and y directions, defined as:

$$f(x) = cos\gamma\left(\frac{x}{a} - \frac{1}{2}\right) + kcosh\gamma\left(\frac{x}{a} - \frac{1}{2}\right), \tag{79}$$

$$g(y) = cos\epsilon\left(\frac{y}{b} - \frac{1}{2}\right) + ccosh\epsilon\left(\frac{y}{b} - \frac{1}{2}\right), \tag{80}$$

where a and b are the side lengths of the plate and k and c are:

$$k = sin\frac{\gamma}{2} / sinh\frac{\gamma}{2} \tag{81}$$

$$c = sin\frac{\epsilon}{2} / sinh\frac{\epsilon}{2} \tag{82}$$

$$tan\frac{\gamma}{2} + tanh\frac{\gamma}{2} = 0 \tag{83}$$

$$tan\frac{\epsilon}{2} + tanh\frac{\epsilon}{2} = 0\,. \tag{84}$$

In order to apply the virtual work principle, the total energy of the cavity-plate coupled system was calculated, which includes the potential and kinetic energies of the panel and the potential energy of the cavity air volume. The potential energy U_p of the vibrating plate was defined as:

$$U_p = \frac{D}{2}\int_0^a \int_0^b \left(\frac{\partial^2 w}{\partial x^2}\right)^2 + \left(\frac{\partial^2 w}{\partial y^2}\right)^2 + 2\left(\frac{\partial^2 w}{\partial x \partial y}\right) \mathrm{dxdy}. \tag{85}$$

Considering Eq.78 and that the acoustic impedance of the absorber the potential energy U_p has to be expressed in terms of the average displacement $\bar{w}_{mn} = \frac{1}{ab}\int_0^a \int_0^b w_{mn}\,\mathrm{dxdy}$, Eq.85 for a square panel after integration becomes:

$$U_p = \frac{D}{2a^2} \sum_m \sum_n (1 + jg_{mn}) B_{mn} \bar{w}_{mn}^2 \tag{86}$$

where g_{mn} is the hysteretic loss factor of the panel material and B_{mn} is defined as:

$$B_{mn} = \frac{\gamma^2\epsilon^2}{256}[(\gamma^4+\epsilon^4)(1+c^2)(1+k^2)+2\gamma^2\epsilon^2(1-c^2)(1-k^2)$$
$$+4\gamma\epsilon(2-\epsilon(1-c^2)-\gamma(1-k^2))]. \tag{87}$$

The kinetic energy T_p of the vibrating plate was defined as:

$$T_p = \frac{M}{2}\int_0^a\int_0^b\left(\frac{\partial w}{\partial t}\right)^2 \mathrm{dxdy} \tag{88}$$

where, M is the surface mass of the panel. Accounting again for Eq. 78 and the average displacement $\bar{w}_{mn}$, T_p for a square panel reads:

$$T_p = \frac{Ma^2}{2}\sum_m\sum_n A_{mn}\bar{\dot{w}}^2_{mn} \tag{89}$$

where

$$A_{mn} = \frac{\epsilon^2\gamma^2}{256}(1+c^2)(1+k^2). \tag{90}$$

Finally, the potential energy U_a of the air cavity volume, which is supposed to be narrow enough to prevent any standing waves occurring in it, can be defined as:

$$U_a = \frac{\gamma_0 P_0}{2V}(\delta V)^2 \tag{91}$$

where V is the volume of the air cavity and $P_0$is the atmospheric pressure. Hence, for a square panel, it becomes:

$$U_a = \frac{\gamma_0 P_0}{2d}a^2\left(\sum_m\sum_n\bar{w}_{mn}\right)^2. \tag{92}$$

Once calculated the potential and kinetic energies of the system, the virtual work principle can be applied, stating that for a system in static equilibrium, at every infinitesimal virtual displacement $\delta\overline{w}$, it is associated a null mechanical work. In light of this, named $F = pa^2$ the driving force of the system, the virtual work principle can be expressed as:

$$\frac{\partial T_p}{\partial\bar{w}}\partial\bar{w}+\frac{\partial U_p}{\partial\bar{w}}\partial\bar{w}+\frac{\partial U_a}{\partial\bar{w}}\partial\bar{w} = Fe^{j\omega t}\partial\bar{w}. \tag{93}$$

Accounting for Eqs. 86, 89 and 92, the equation above becomes:

$$MA_{mn}\bar{\ddot{w}}_{mn}+\frac{D(1+jg_{mn})}{a^4}B_{mn}\bar{w}_{mn}+\frac{\gamma_0 P_0}{d}\sum_m\sum_n\bar{w}_{mn} = pe^{j\omega t}. \tag{94}$$

This is the equation of motion for a single mode of the coupled panel-cavity system. Remembering that the average velocity $\bar{V}_{mn}$ for each single mode can be obtained from:

$$\bar{\dot{w}}_{mn} = \bar{V}_{mn} e^{j\omega t} \tag{95}$$

a set of equations of the type of Eq. 94 can be solved simultaneously in matrix form, in order to calculate the average velocity $\bar{V}_{mn}$ for each mode. Then, recalling that

$$Z_a = \frac{p}{\sum_m \sum_n \bar{V}_{mn}} \tag{96}$$

a frequency expression of the average specific acoustic impedance of the panel absorber can finally be derived.

Part II

Preliminary investigations and numerical-experimental validations

4 Preliminary study on the effects of panel size and edge constraints

In this chapter, the results of preliminary numerical simulations are presented, in order to investigate to what extent panel size and edge constraint conditions affect the behavior of panel absorbers in terms of acoustic impedance and absorption. In the first place, a numerical analysis was conducted on panel absorbers of different size, holding the same constraint conditions and exciting them by a plane sound field at normal incidence. Surface impedances evaluated from multiphysics FEM simulations were then compared to those obtained from analytical approximate models. Discrepancies in terms of resonance frequencies and the accuracy of approximate models were investigated. A further numerical investigation was performed on a plate resonator under the same excitation conditions as the case above, by changing in turn the edge constraint conditions with the aim of highlighting the effects on the acoustic behaviour of such a sample due to different mounting conditions. Again, effects on the resulting impedances and absorption coefficients were investigated.

4.1 Panel size effects for plane wave incidence

As mentioned in the previous chapter, analytical approximate formulations, introduced in Section 3.1, model the coupled panel-cavity systems as SDOF mass-spring oscillators, accounting for only air cavity stiffness and the surface mass of the plate and neglecting the actual surface extension of the panel itself. In order to highlight the main inaccuracies that such a formulation implies against a realistic model of a panel absorber, FEM simulations of a standing wave tube test-rig were performed (Figure 8), with the aim of evaluating the surface impedance of the sample. The sample, assumed to behave as a homogeneous isotropic and elastic material, was a circular aluminum plate of thickness $h = 0.5$ mm, the mechanical and geometrical properties of which are listed in Table 1. The plate was clamped all around the

ϕ [cm]	h[mm]	E [GPa]	ν [-]	η [-]	ρ [kg/m^3]
10, 30, 60	0.5	70	0.32	0.0015	3000

Table 1: Geometrical and mechanical properties of the aluminum plate: diameter ϕ, plate thickness h, elastic modulus E, Poisson's ratio ν, loss factor η, mass density ρ.

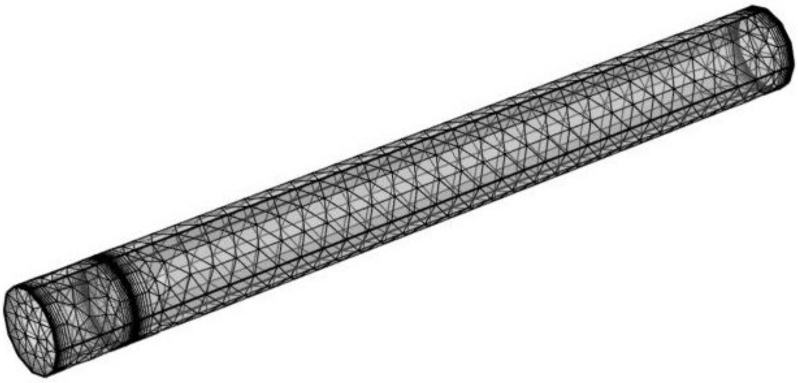

Figure 8: FEM meshed model of a standing wave tube test-rig. The sample, modelled as a shell coupled to a backing air domain, was a cylindrical panel absorber with an air cavity of 10 cm depth.

edges and coupled with an air cavity of 4.5 cm depth. Parametric FEM simulations were then performed, by progressively increasing the plate diameter from 10 cm to 30 cm and 60 cm. According to Eq. 74 the surface impedance of the system was calculated as follows:

$$Z_s = j[\omega m - Z_c cot(k_0 d)]\,. \tag{97}$$

where k_0 and d are the wavenumber and depth of the air cavity, and m is the surface mass of the plate. Material damping was accounted for by defining a complex material density as:

$$\rho = \rho_0(1 - j\eta) \tag{98}$$

where η is the isotropic loss factor reported in Table 1.

The analytical surface impedance Z_s resulting from FEM simulations, was evaluated by extracting complex sound pressure values at two points within the air domain of the tube, according to the transfer function method, as defined in ISO 10534-2:1998 [6]. The related absorption coefficient was calculated according to the equation:

$$\alpha = \frac{4Re\left\{\frac{Z_S}{Z_0}\right\}}{\left|\frac{Z_S}{Z_0}\right|^2 + 2Re\left\{\frac{Z_S}{Z_0}\right\} + 1}. \tag{99}$$

Numerical and analytical impedances (in terms of phase) and absorption coefficients were compared in Figures 9, 10 and 11. As visible from the graphs, the analytical results show always the same and only resonant frequency, occurring at 230 Hz, regardless of the surface area of the plate. Looking at Figure 9, it is noticeable that the first numerical resonance frequency occurs at 501 Hz, showing a relevant discrepancy in terms of modal behaviour with respect to the approximate model. As long as the panel diameter is increased, being equal the clamped edge conditions, further modes appear in the numerical solution, while the resonance frequency of the panel-cavity coupled system approaches the analytical value. This is noticeable in Figure 10, where the first numerical resonance frequency occurs now at 241 Hz, and additional modes are detected at 145 Hz and 462 Hz, where new absorption peaks are visible. This is even more evident in Figure 11, where alongside the 230 Hz resonance, further modes occur at 104, 183, 319, 456 and 620 Hz. These additional resonances can be identified as structural radiative modes of the plate: such modeshapes are always symmetric with respect to the displacement occurring at the center of the panel, which is coincides to an antinode, namely a point where the displacement field occurring over the surface of the panel reaches its maximum. Regardless of the shape of the plate, the highest radiation efficiencies occur at the fundamental radiative mode and at higher order odd modes. Generally, for circular plates, such modeshapes are consituted by an antinodal area occurring at the center of the plate with additional concentric antinodal circumferences, which increase the more the higher the eigenfrequency. This is noticeable in Figure 12 where the first and second radiative modeshapes of a circular clamped aluminum plate of 30 cm diameter are shown.

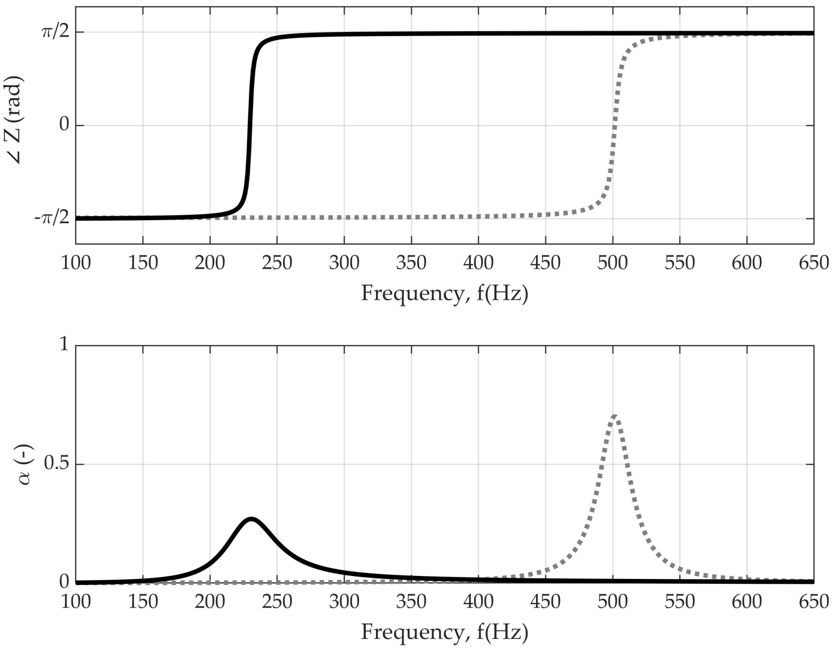

Figure 9: Surface Impedance phase (top) and absorption coefficient (bottom) of a 10 cm diameter panel resonator: ——approximate model, ┈┈FEM simulation.

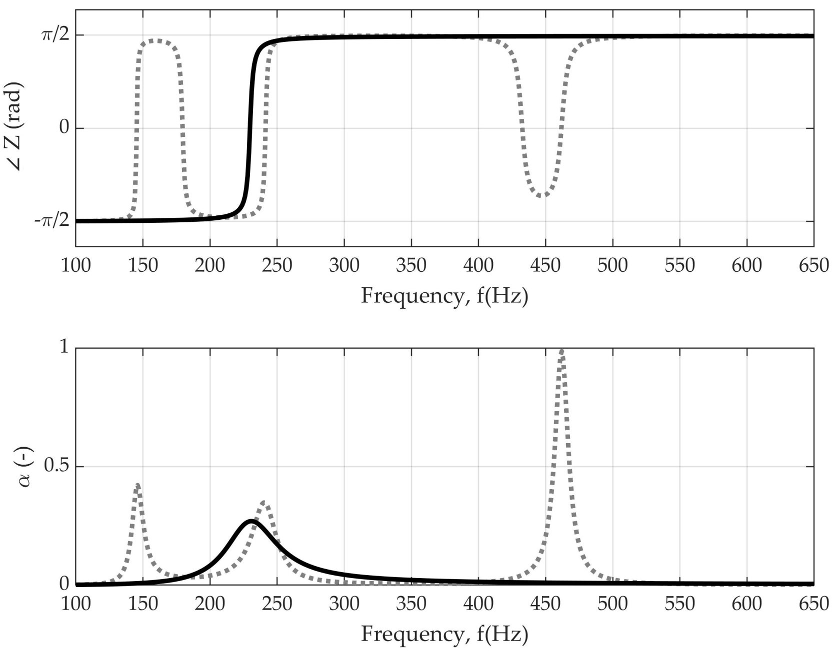

Figure 10: Surface Impedance phase (top) and absorption coefficient (bottom) of a 30 cm diameter panel resonator: ——approximate model, ┈┈FEM simulation.

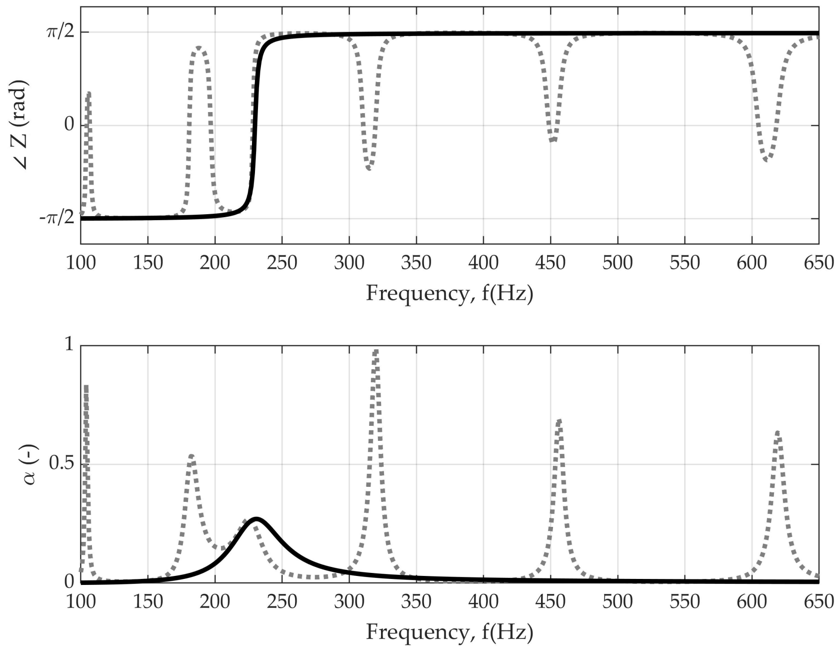

Figure 11: Surface Impedance phase (top) and absorption coefficient (bottom) of a 60 cm diameter panel resonator: ——approximate model, ········FEM simulation.

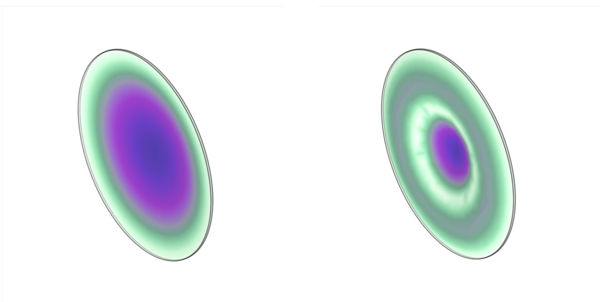

Figure 12: First (left hand side) and second (right hand side) radiative modeshapes of an aluminum clamped circular plate (30 cm diameter).

From this preliminary analysis, the following outcomes are worth to be highlighted:

- approximate models are far more inaccurate with respect to numerical simulations, the smaller the surface area of the panel. This comes from the basic assumption of pistonic motion of a plate of infinite extent, which neglects the effect of edge constraints on the dynamic response of the plate. Being equal the cavity depth and the edge constraints of the plate, there is a surface area extent at which approximate model starts to be efficient in predicting just one of the plate-cavity resonance frequency (60 cm diameter panel in the case reported here);

- the greater the surface of the plate, the more the actual resonant frequencies of the system. Indeed, additional eigenfrequencies can appear above and below the coupled system resonance frequency, and are represented by radiative modes of the plate. Considering the same frequency range, the number of this modes increases with the surface area extent of the plate.

In light of the above, it is evident that more thorough analytical models of panel absorbers are necessary in order to ensure accurate acoustic predictive analyses: these should take in account the influence of panel size on the modal behaviour of the plate, which is responsible, as seen, of the additional resonant peaks experienced by a realistic panel resonator.

4.2 Edge conditions effects for plane wave incidence

In this paragraph, a preliminary FEM analysis is presented in order to investigate the effect of edge constraint conditions upon the resonant behaviour of panel absorbers. As in the case of the previous analysis, a cylindrical panel absorber was used as a sample, modeling an impedance tube virtual test-rig and assuming plane wave incidence conditions. The diameter size of the plate was hold to be 10 cm wide, as well as the cavity depth, which was equal to 4.5 cm. Three simulations were performed by applying different constraint conditions at the edges: clamped, simply supported and free edge condition. The geometrical and mechanical properties of the plate are again summarized in Table 1. Also in this case, surface impedances and absorption coefficients were evaluated and compared in the frequency range 100-650 Hz, in which only the first resonance mode of the system is observable.

As noticeable from the graphs in Figure 13, a gradual decrease in frequency of the first eigenmode is observable when changing edge constraints from clamped (501 Hz) to simply supported (301 Hz) and then to free edge condition (229 Hz). This is due to the increased stiffness provided by edge constraints as long as they approach to clamping. In this case indeed, edge rotations and linear displacements are both suppressed, implying the actual deflection to involve the smallest amount of plate mass: similarly to what observed above, the smaller the vibrating surface area, the higher the eigenfrequency of the first structural mode.

A further relevant effect is noticeable by analyzing the absorption coefficient graph. Indeed, alongside the frequency shifting effect, a gradual decrease of absorption peak is observable as long as the constraint conditions become less rigid, being equal the plate material damping: in the clamped case indeed, absorption achieves the maximum value of 0.7; in the simply supported case it decreases to 0.3, whilst in the extreme conditions of free edges, absorption becomes zero. Since no source

edge condition	f_{res} [Hz] (uncoupled plate)	η_{res} [-]	T_{struct} [s]
free edge	9.22×10^{-5}	0.9998	2.41×10^{4}
simply supported	233.57	0.0075	1.25
clamped	476.88	0.0075	0.61

Table 2: Structural decay times at the first eigenmode of a circular plate with three different constraint conditions.

of damping other than internal material loss factor was considered in the model, this phenomenon can be attributed to the relationship between material damping and the flexural stiffness resulting from different constraint conditions. Indeed, since a clamped plate is less free to vibrate with respect to a simply supported or free-edged plate, sound energy is more easily dissipated by deflection. This is also observable from the impedance trends: as long as constraint become less rigid, the phase curve becomes less damped, up to the free edge case where a steep trend is observable in correspondence of the resonance frequency. A further demonstration of such phenomenon can be provided by evaluating the structural modal decay times for the same plate subjected to different edge conditions. Structural decay times T_{struct} can be calculated by inverting the relationship provided by Cremer [9], as follows:

$$T_{struct} = \frac{ln(10^6)}{2\pi f_{res}\eta_{res}} \tag{100}$$

where f_{res} and η_{res} are respectively the real part and the damping ratio associated to the eigenfrequency in question. These quantities can be readily calculated by means of a FEM eigenfrequency study. As summarized in Table 2, structural modal decay times decrease from a value of 2.41×10^4 seconds for the free edge case to values of 1.25 and 0.61 seconds for the simply supported and clamped edge conditions, respectively.

The outcomes of this preliminary analysis revealed that:

- as noticeable from Figure 13, analytical approximate models provide the same results in terms of impedance and absorption coefficient as those resulting from FEM simulations of free edge panels: this is in compliance with the assumption of pistonic motion and infinite sized vibrating panels, although it represents the less realistic condition when compared to the build-up of real absorbers;

- from now on, the analysis will be focused on panel absorbers with clamped edges, since they represent the closest condition to the building process of a real panel absorber, due to its ease of construction and affordable costs.

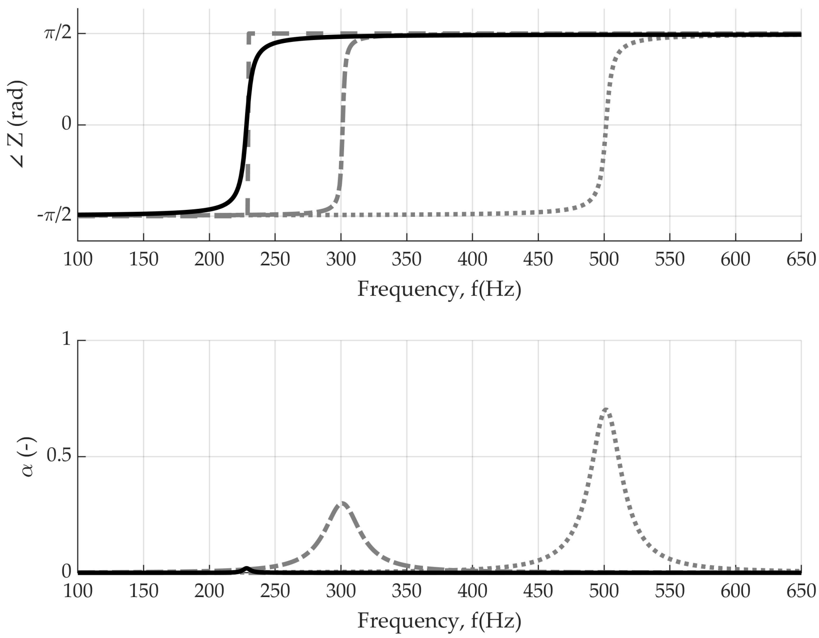

Figure 13: Surface Impedance phase (top) and absorption coefficient (bottom) of a 10 cm diameter panel resonator for different constraint conditions: approximate model, FEM clamped edges, FEM simply supported edges, FEM free edges.

Nevertheless, it is the most mathematically far condition from approximate models, hence the need for a more detailed characterization, which is one of the main objectives of this thesis.

5 Impedance of finite-sized clamped plates: experimental and numerical analysis

In this chapter, analytical formulations of the specific acoustic impedance of finite-sized clamped plates are validated against numerical simulations and experimental measurements. Circular and rectangular plates are tested within a standing wave tube, with the aim of evaluating their transmission loss and then specific acoustic impedance, by means of the acoustic method proposed by Song and Bolton [5] and implemented in the ASTM E2611-19 standard [30]. Resulting quantities are compared against analytical formulations of Eq. 48 for circular plates and Eq. 72 for rectangular plates. Possible variations in the resulting acoustic impedance due to oblique sound incidence are investigated numerically and analytically, by introducing slight but significant integrations to Eq. 72, to account for plane oblique incidence in the case of rectangular clamped plates.

5.1 Acoustical measurement of the specific acoustic impedance of a plate

A transfer matrix based method for evaluating the acoustical properties (such as characteristic impedance and complex wavenumber) of homogeneous and isotropic porous materials was proposed by Song and Bolton [5] and successively implemented in the ASTM E2611-19 standard [30]. Here the basic formulations are presented and some considerations are introduced in order to extend the method to applications involving elastic plate samples in bending.

The experimental test-rig for the application of such a method is schematized in Figure 14: an impedance tube is divided in two segments by the sample holder, which is placed halfway of its length. A plane wave normally incident sound field is radiated into the section upstream of the sample by a loudspeaker placed at one end of the tube. Sound pressure values are measured at positions P_1 to P_4,two of them being located in the downstream segment of the tube. The other end of the tube is capped by means of an anechoic termination (usually a layer of porous material). Complex sound pressures measured at positions 1 to 4 can be written as the superposition of positive and negative going sound waves A, B, C, D as follows:

$$
\begin{aligned}
P_1 &= (Ae^{-jkx_1} + Be^{jkx_1})e^{j\omega t}, \\
P_2 &= (Ae^{-jkx_2} + Be^{jkx_2})e^{j\omega t}, \\
P_3 &= (Ce^{-jkx_3} + De^{jkx_3})e^{j\omega t}, \\
P_4 &= (Ce^{-jkx_4} + De^{jkx_4})e^{j\omega t},
\end{aligned} \tag{101}
$$

where $x_1$to x_4 represent the coordinates of the four microphone positions, k is the wavenumber in air and A, B, C and D can be written as:

$$
\begin{aligned}
A &= \frac{j(P_1 e^{jkx_2} - P_2 e^{jkx_1})}{2sink(x_1 - x_2)} \\
B &= \frac{j(P_2 e^{-jkx_1} - P_1 e^{-jkx_2})}{2sink(x_1 - x_2)} \\
C &= \frac{j(P_3 e^{jkx_4} - P_4 e^{jkx_3})}{2sink(x_3 - x_4)} \\
B &= \frac{j(P_4 e^{-jkx_3} - P_3 e^{-jkx_4})}{2sink(x_3 - x_4)}.
\end{aligned} \tag{102}
$$

In light of the above, transfer matrix calculation can be applied to relate each other pressure and normal particle velocity fields at the upstream and downstream interfaces of the sample, as follows:

$$
\begin{bmatrix} P \\ V \end{bmatrix}_{x=0} = \begin{bmatrix} T_{11} & T_{12} \\ T_{21} & T_{22} \end{bmatrix} \begin{bmatrix} P \\ V \end{bmatrix}_{x=d} \tag{103}
$$

where $x = 0$ and $x = d$ are the linear coordinates of the two faces of the sample. Pressure and velocity values can be expressed as a function of the travelling waves A, B, C, D as follows:

$$
P|_{x=0} = A + B \tag{104}
$$

$$
V|_{x=0} = \frac{A - B}{\rho_0 c} \tag{105}
$$

$$
P|_{x=d} = Ce^{-jkd} + De^{jkd} \tag{106}
$$

$$
V|_{x=d} = \frac{Ce^{-jkd} - De^{jkd}}{\rho_0 c} \tag{107}
$$

where $\rho_0 c$ is the characteristic impedance of plane waves in air and d is the sample thickness. Equation 103, which represents an overdetermined system of equations, can be reduced to a linear system and solved by taking in account the principles of reciprocity and simmetry, yielding:

$$
\begin{aligned}
T_{11} &= T_{22} \\
T_{11}T_{22} - T_{12}T_{21} &= 1.
\end{aligned}
\tag{108}
$$

In light of this, the terms T_{ij} can be written as:

$$T_{11} = \frac{P|_{x=d}\, V|_{x=d} + P|_{x=0}\, V|_{x=0}}{P|_{x=0}\, V|_{x=d} + P|_{x=d}\, V|_{x=0}} \tag{109}$$

$$T_{12} = \frac{P|_{x=0}^{2} - P|_{x=d}^{2}}{P|_{x=0}\, V|_{x=d} + P|_{x=d}\, V|_{x=0}} \tag{110}$$

$$T_{21} = \frac{V|_{x=0}^{2} - V|_{x=d}^{2}}{P|_{x=0}\, V|_{x=d} + P|_{x=d}\, V|_{x=0}} \tag{111}$$

$$T_{22} = \frac{P|_{x=d}\, V|_{x=d} + P|_{x=0}\, V|_{x=0}}{P|_{x=0}\, V|_{x=d} + P|_{x=d}\, V|_{x=0}}. \tag{112}$$

The T_{ij}terms if the matrix in Eq. 103 can be related to the acoustic properties of elastic plates in bending by considering the following formulation reported by Allard et al. [28]:

$$\begin{bmatrix} \sigma_x \\ v_x \end{bmatrix}_{x=0} = \begin{bmatrix} 1 & -Z_p(\omega) \\ 0 & 1 \end{bmatrix} \begin{bmatrix} \sigma_x \\ v_x \end{bmatrix}_{x=d} \tag{113}$$

where σ_x and v_x are the normal stresses and velocities on the faces of the plate and Z_p represents its mechanical impedance, given as a ratio of pressure over velocity. Due to the acoustical excitation of the vibrating plate, this can also be intended as the specific acoustic impedance of the plate, which can be calculated by means of Eq. 72 for rectangular plates and Eq. 48 for circular plates.

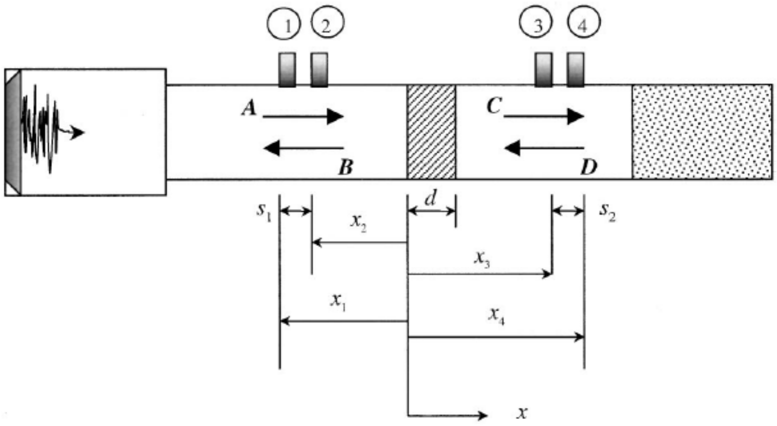

Figure 14: Schematic of the tube test-rig for the application of the Song-Bolton method. Taken from ref. [5].

5.1.1 Rectangular clamped plate

The normal specific acoustic impedance of a rectangular clamped plate has been calculated according to Eq. 72. In order to validate such a formulation against experimental data, sound transmission measurements were performed by means of an impedance tube of rectangular cross section. An acrylic plate was tested, the geometrical and mechanical properties of which are reported in Table 3. The acoustic method proposed by Song and Bolton [5] was employed for measuring the specific acoustic impedance of the plate. As suggested by the authors, a steel standing wave tube of 143×93 mm rectangular cross section was used, with an additional tube segment mounted downstream of the sample holder. The acrylic plate was secured to the tube structure by means of through screws on side flanges of the tube, in order to simulate edge clamped conditions. A half-inch microphone was placed at four locations along the tube, two upstream the sample holder and the others across the additional tube section, which was provided with a polyester fiber anechoic termination. A schematic of the measurement set up is shown in Figure 15. Analytical impedance, calculated from Eq. 72, is compared to that measured, showing a good agreement in terms of magnitude and phase (Figure 16). Phase inversion occurs at the first radiative mode of the plate (1,1), whose associated modeshape is depicted in Figure 17.

$L_x [mm]$	$L_y [mm]$	$h\ [mm]$	$E\ [GPa]$	$\nu [-]$	$\eta\ [-]$	$\rho\ [kgm^{-3}]$
143.00	93.00	2.00	2.89	0.35	0.01	1078.58

Table 3: Geometrical and mechanical properties of the acrylic plate: L_x and L_y (side lengths), h (thickess), E (elastic modulus), ν (Poisson's ratio), η (material loss factor), ρ (mass density).

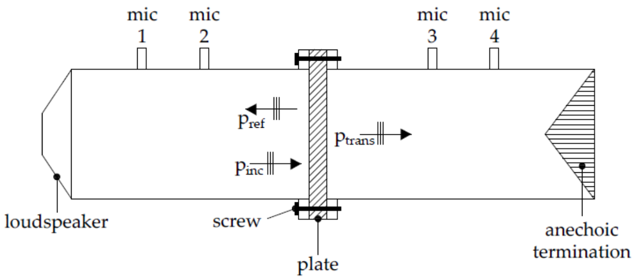

Figure 15: Schematic of the setup for sound transmission measurements of a rectangular plate in a standing wave tube. Dimensions are expressed in mm.

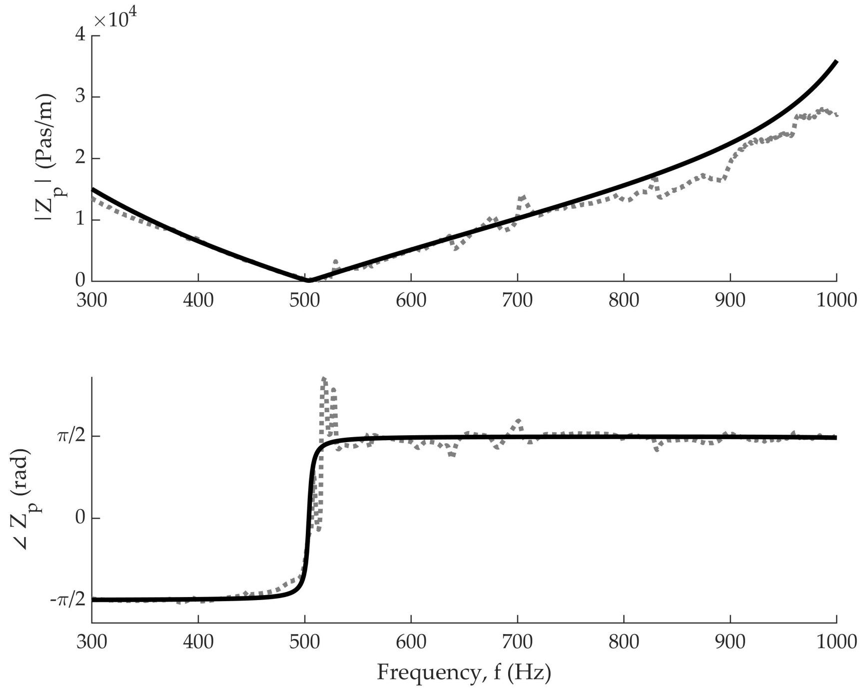

Figure 16: Magnitude and phase of the specific acoustic impedance of a rectangular clamped acrylic plate: measured values; analytical values.

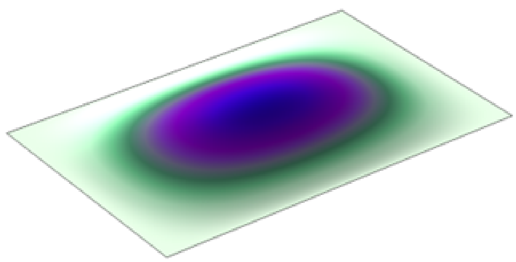

Figure 17: Modeshape of a 143 mm × 93 mm plate at the first radiative resonant frequency (506 Hz), obtained from FEM eigenfrequency study on an acrylic shell clamped at the edges.

5.1.2 Circular clamped plate

Similarly to the case above, the Song-Bolton method was applied also to the case of circular plates. On this purpose, a circular steel impedance tube was used in order to test a circular aluminum plate. Geometrical and mechanical properties of the plate are reported in Table 4. The choice of a very reduced sample thickness, allowed for emulating edge clamping conditions by framing the aluminum plate in the middle of the profiled joint connecting the two tube segments (see Figure 18). Also in this case, acoustic impedance calculated from Eq. 48 is compared to that measured in terms of magnitude and phase within the range of frequency of 250-2000 HZ, in which plane wave assumption is valid. As visible from Figure 19, results are in good agreement over frequency, and at both resonances visible at 477 Hz and 1833 Hz, corresponding to the first two radiative modes of the plate, the modeshapes of which are similar to those depicted in Figure 12. Some deviation between measured and analytical values is observable close to the antiresonance peak in the impedance magnitude: this may be expected in light of the sudden transition from a resonant to a rigid behaviour in correspondence of the antiresonance. Nevertheless, the measured impedance value at antiresonance is far more greater than the characteristic impedance of air, suggesting a fairly rigid behavior of the plate, as expected at that frequency.

$\phi[mm]$	h $[mm]$	E $[GPa]$	$\nu[-]$	η $[-]$	ρ $[kgm^{-3}]$
100.00	0.50	69	0.33	0.015	3006.63

Table 4: Geometrical and mechanical properties of the circular aluminum plate: ϕ (diameter), h (thickess), E (elastic modulus), ν (Poisson's ratio), η (material loss factor), ρ (mass density).

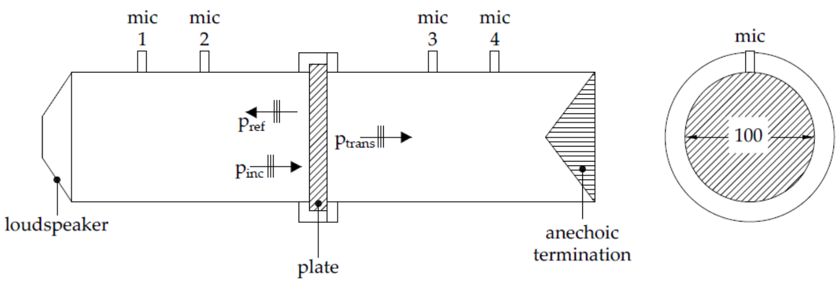

Figure 18: Schematic of the setup for sound transmission measurements of a circular plate in a standing wave tube. Dimensions are expressed in mm.

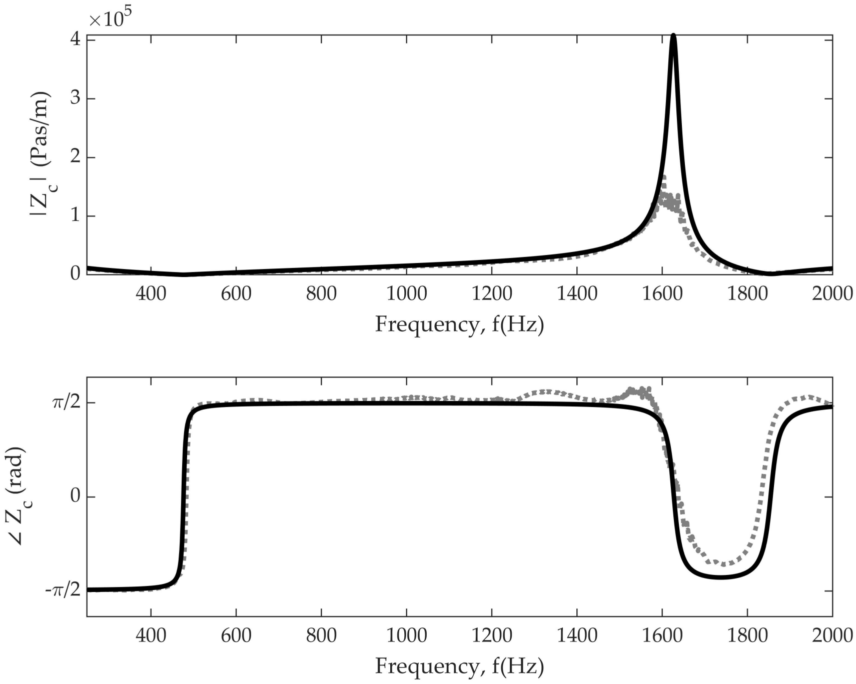

Figure 19: Magnitude and phase of the specific acoustic impedance of a circular clamped aluminum plate: measured values; analytical values.

5.2 Numerical investigation on the plate response to oblique plane waves

In the analytical formulations adopted so far, sound fields exciting the samples under analysis were always assumed to be plane and normal to the surface of the plate. Under this assumption, the pressure distribution over the plate surface is uniform, regardless of frequency and the dimensional relationship between acoustic wavelengths and the characteristic dimensions of the sample. In light of that, a numerical investigation was carried out on a baffled rectangular plate, by varying the angle of incidence of the impinging sound field, in order to test the validity of Eq. 72, which was properly integrated to account for such an external condition. In particular, the term $P(x,y)$, representing the incident pressure distribution defined over the surface of the plate, can be more generally defined by accounting for oblique angles of incidence, as follows:

$$P(x,y) = p_0 e^{-jk_0[x\,sin\theta cos\varphi + y\,sin\theta sin\varphi]}, \tag{114}$$

where θ and φ respectively represent the zenithal and azimuthal angles of incidence and p_0 is the pressure amplitude. Substituting $P(x,y)$ as defined in Eq. 114 into Eq. 72, it would be possible to calculate the resulting acoustic impedance, in

$L_x[mm]$	$L_y[mm]$	$h\ [mm]$	$E\ [GPa]$	$\nu[-]$	$\eta\ [-]$	$\rho\ [kgm^{-3}]$
143.00	93.00	0.50	70	0.25	0.02	3000

Table 5: Geometrical and mechanical properties of the acrylic plate: L_x and L_y (side lengths), h (thickness), E (elastic modulus), ν (Poisson's ratio), η (material loss factor), ρ (mass density).

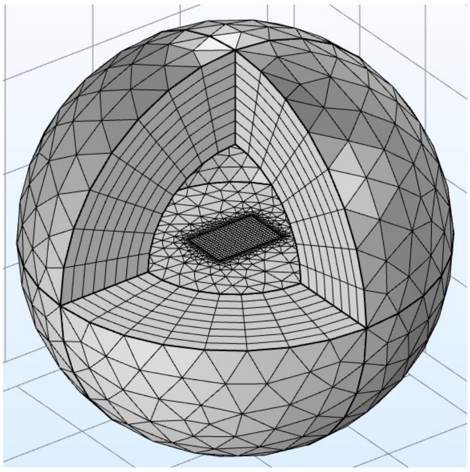

Figure 20: Free-field FEM meshed domain: the baffled rectangular clamped shell lies in the xy plane (mapped quadratic elements), surrounded by a spherical air domain (tetrahedral meshes). External PML shells are discretised by means of swept meshes.

presence of a plane and oblique condition of incidence. In order to investigate the validity of this formulation, a set of numerical FEM simulations was performed, by considering a baffled and clamped rectangular plate in free field conditions, excited by a background sound pressure field at various angles of incidence. In order to do so, a three-dimensional model was set up considering a baffled plate lying on the middle plane of a sphere, which was modeled as an acoustic domain with its external shells defined as Perfectly Matched Layers (PML): such numerical conditions are essential to guarantee a perfect sound absorption at the boundaries, with the aim of effectively simulating acoustic free field conditions. In the first instance, the model was validated by assuming normal plane wave incidence, and comparing the acoustic impedance evaluated as the ratio of the surface averaged acoustic pressure and particle velocity over the surface of the plate. Such an impedance, was then compared to that calculated from Eq. 72, assuming plane wave field normal incidence. The geometrical and mechanical features of the plate in question are summarized in Table 5, whilst the meshed FEM domain is depicted in Figure 20.

On this purpose it is worth to highlight that mapped quadratic mesh elements were chosen to discretise the structural domain, by identifying the smallest element size as $\lambda_{struct}/10$, where λ_{struct} is the smallest bending wavelength. The adjacent

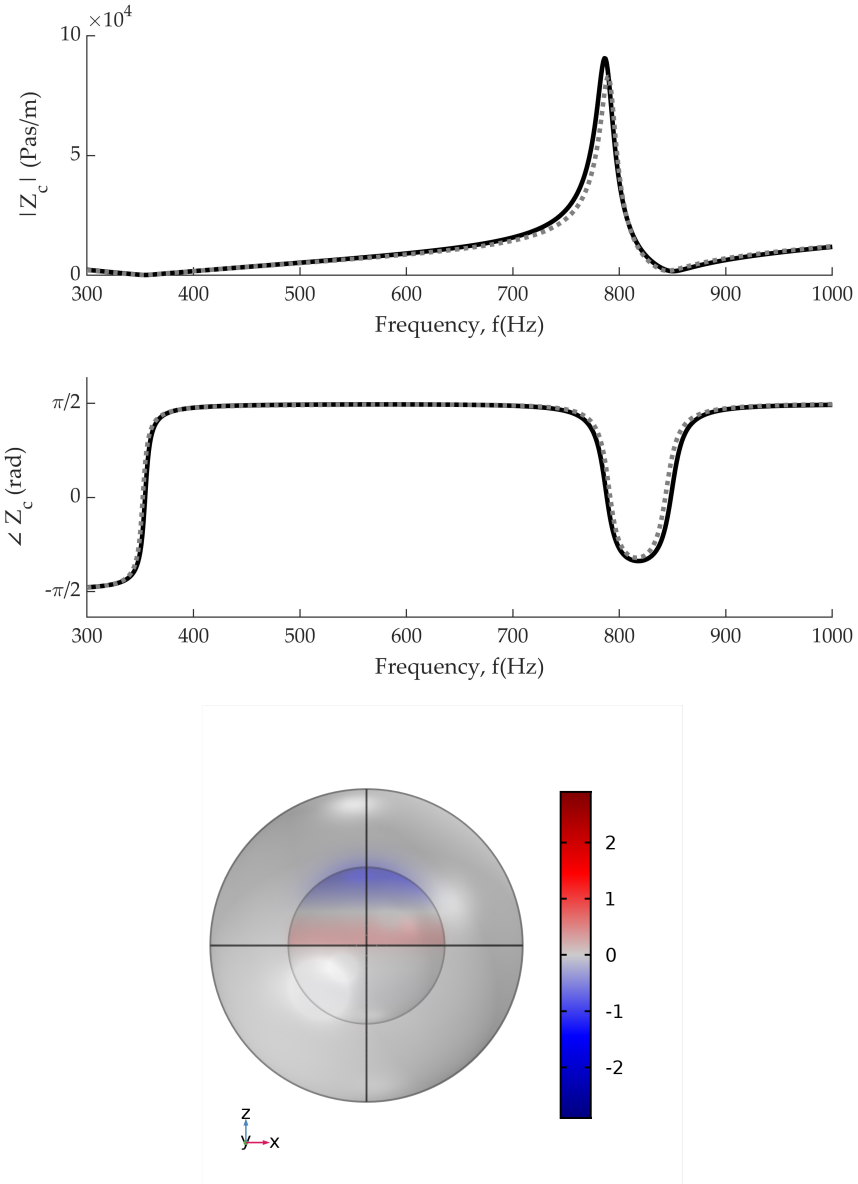

Figure 21: Top: Magnitude and phase of the specific acoustic impedance of a rectangular clamped aluminum plate for plane wave incidence at $\theta = 0°$: ——— analytical values; ········ FEM simulated values. Bottom: representation of the incident sound pressure field at 1 kHz within the air domain of the FEM model. The baffled plate lies in the xy plane and PML shells surround the spherical air domain.

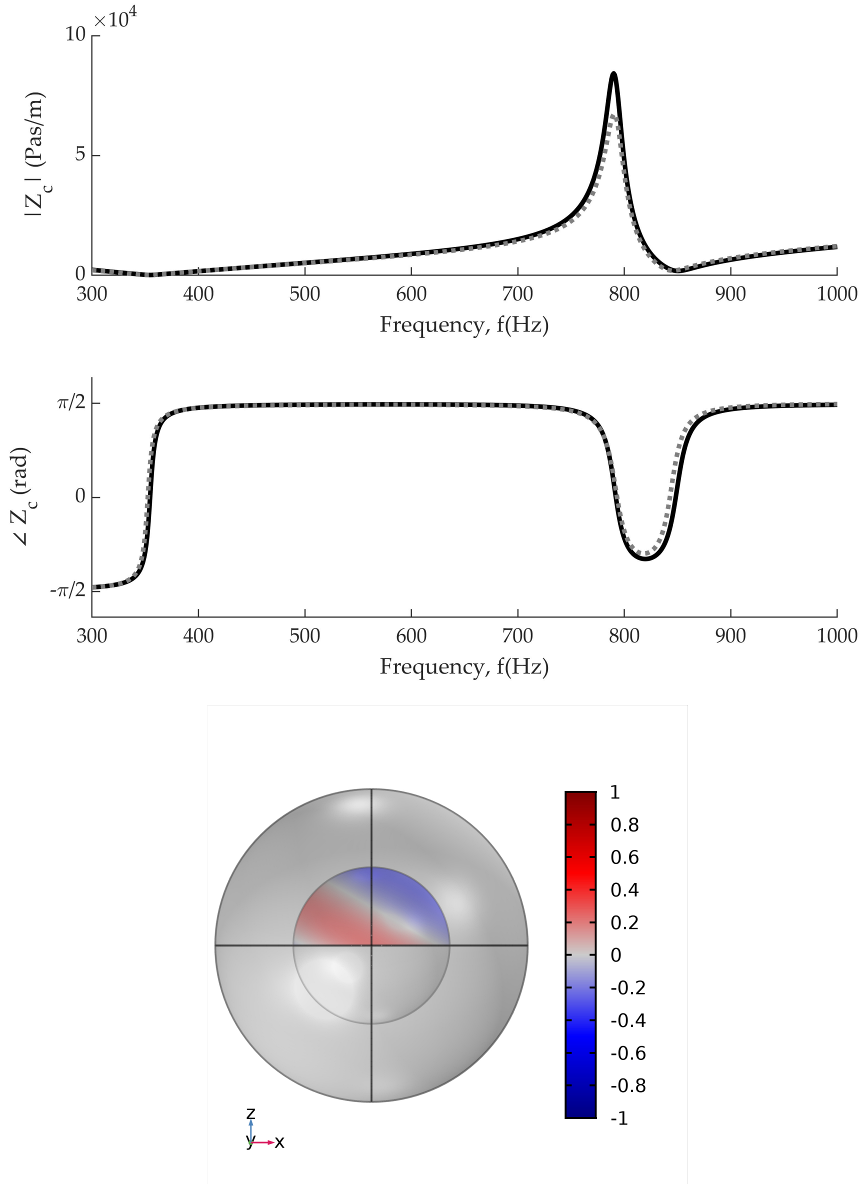

Figure 22: Top: Magnitude and phase of the specific acoustic impedance of a rectangular clamped aluminum plate for plane wave incidence at $\theta = 30°$: analytical values; FEM simulated values. Bottom: representation of the incident sound pressure field at 1 kHz within the air domain of the FEM model. The baffled plate lies in the xy plane and PML shells surround the spherical air domain.

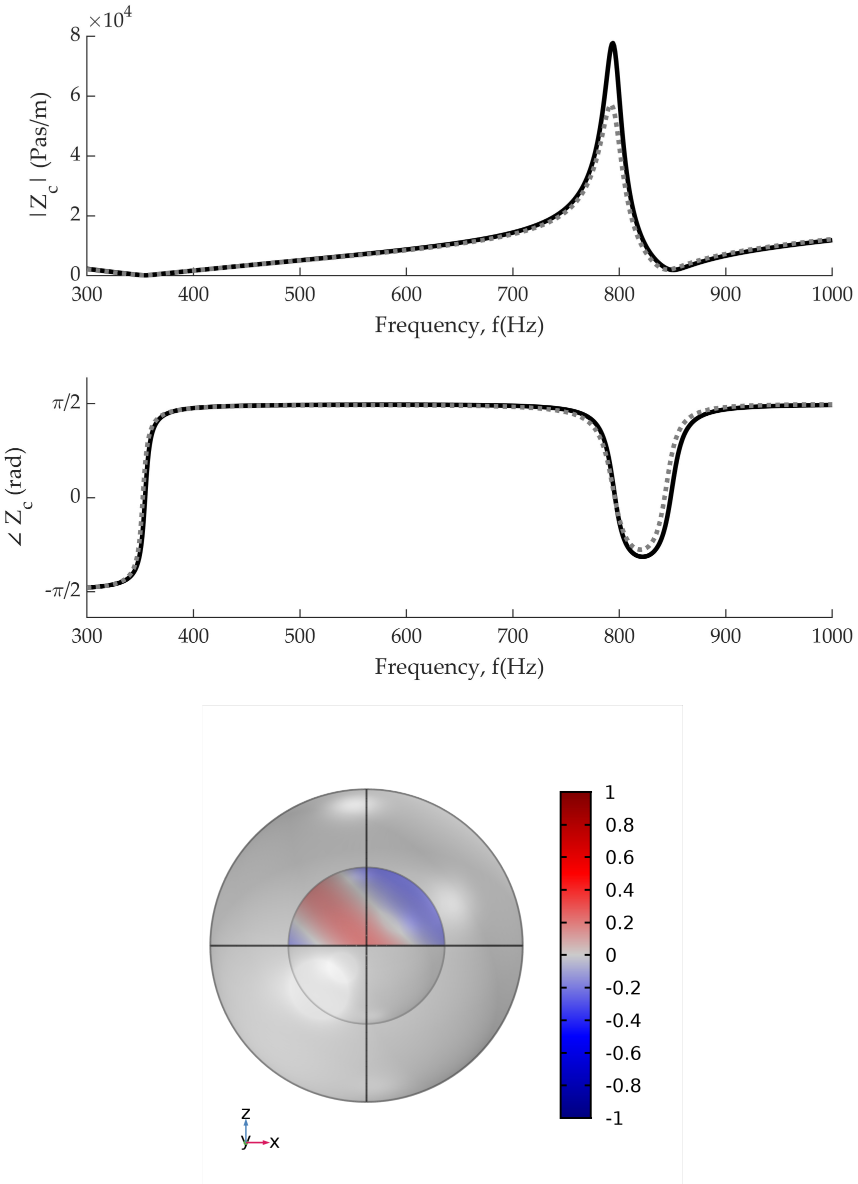

Figure 23: Top: Magnitude and phase of the specific acoustic impedance of a rectangular clamped aluminum plate for plane wave incidence at $\theta = 45°$: ——analytical values; ········FEM simulated values. Bottom: representation of the incident sound pressure field at 1 kHz within the air domain of the FEM model. The baffled plate lies in the xy plane and PML shells surround the spherical air domain.

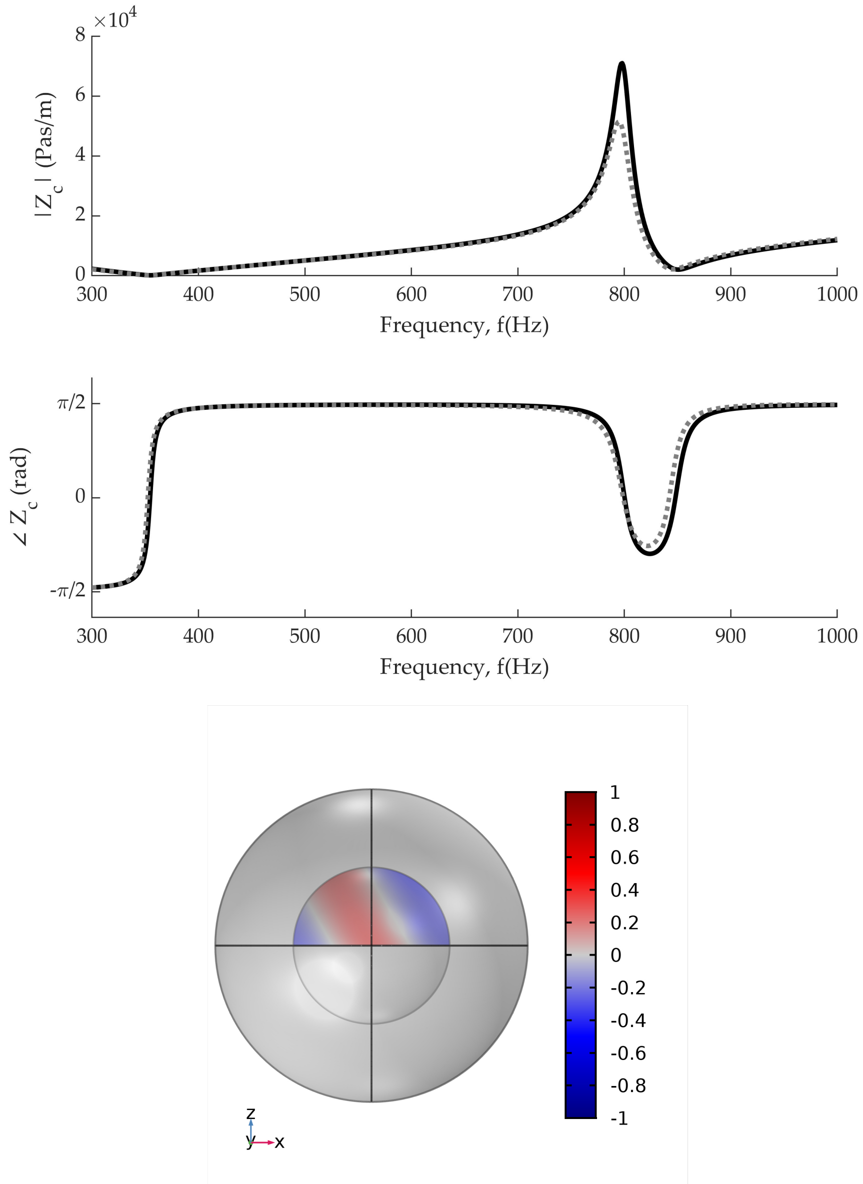

Figure 24: Top: Magnitude and phase of the specific acoustic impedance of a rectangular clamped aluminum plate for plane wave incidence at $\theta = 60°$: —— analytical values; ········ FEM simulated values. Bottom: representation of the incident sound pressure field at 1 kHz within the air domain of the FEM model. The baffled plate lies in the xy plane and PML shells surround the spherical air domain.

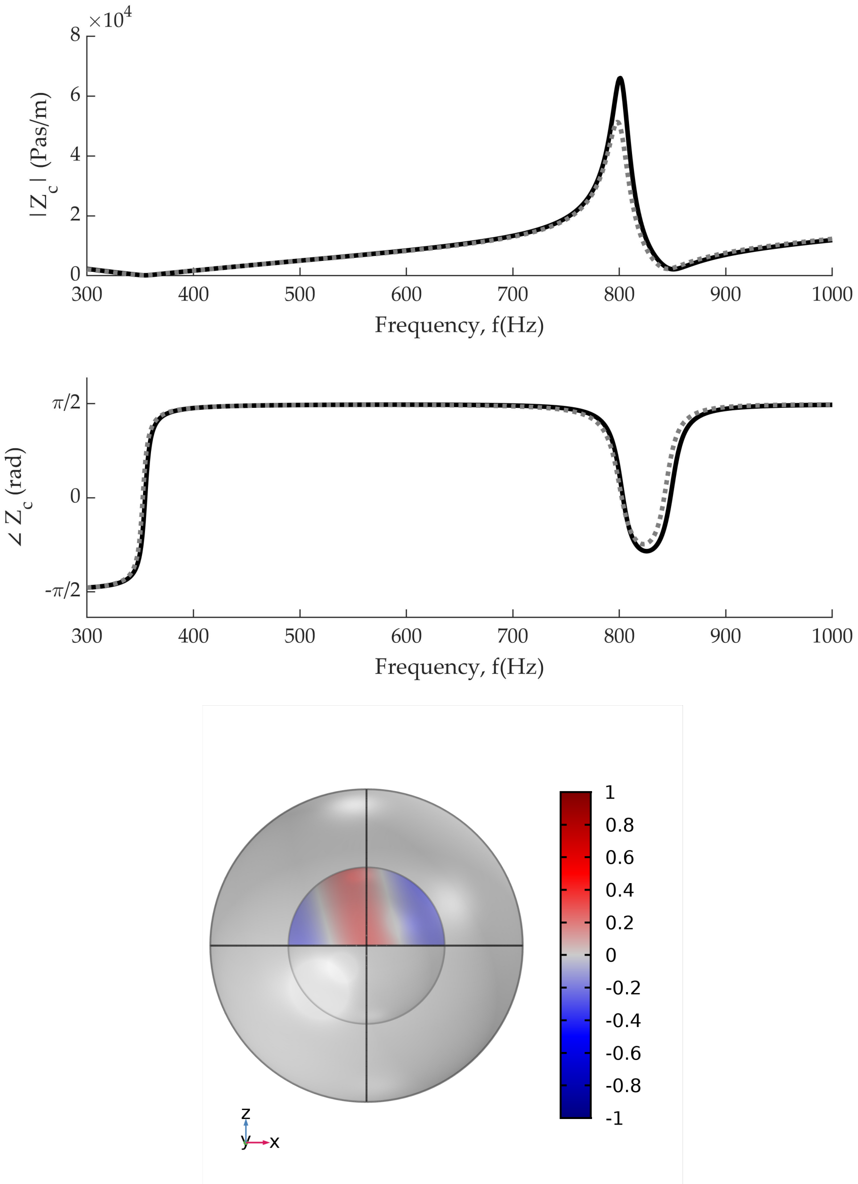

Figure 25: Top: Magnitude and phase of the specific acoustic impedance of a rectangular clamped aluminum plate for plane wave incidence at $\theta = 75°$: analytical values; FEM simulated values. Bottom: representation of the incident sound pressure field at 1 kHz within the air domain of the FEM model. The baffled plate lies in the xy plane and PML shells surround the spherical air domain.

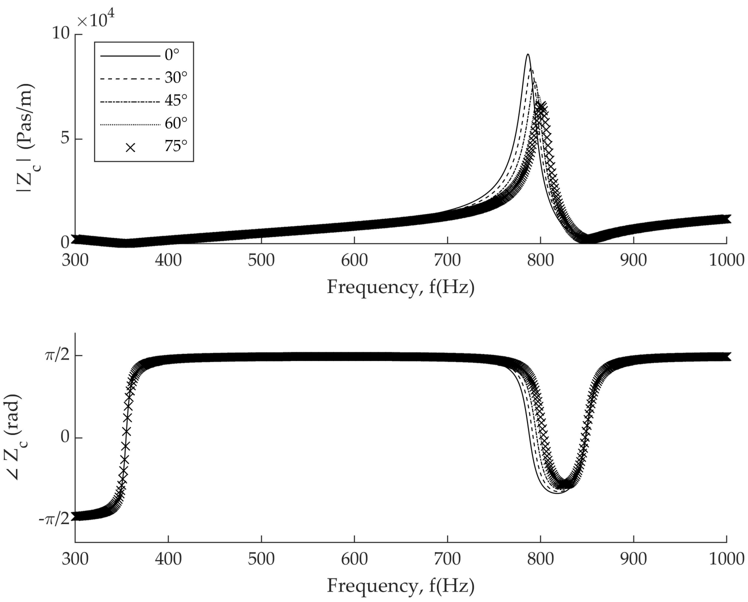

Figure 26: Magnitude and phase of the analytical specific acoustic impedance of a rectangular clamped aluminum plate for plane wave incidence at $\theta = 0°, 30°, 45°, 60°, 75°$.

air domain was meshed using free tetrahedral elements according to the $\lambda/8$ rule of thumb, whilst for PMLs swept meshes were used. Specific acoustic impedances are compared in Figure 21: as noticeable from the graph, in the frequency range of 300-1000 Hz, the first two radiative modes are observable (352 Hz and 848 Hz), showing a good agreement between numerical and analytical data.

Once such a model was validated, the zenith angle of incidence θ with respect to the normal direction to the plate, of the impinging sound field was gradually varied across values of $\theta = 30°, 45°, 60°, 75°$. For each of this value, a new simulation was performed and the plate acoustic impedance was evaluated and then compared to the analytical solution from Eq. 72, which was properly integrated considering the oblique incident pressure $P(x, y)$ from Eq. 114. As visible from Figures 22-25, analytical results are again in good accordance with numerical impedances, confirming the validity of the analytical model also for plane oblique incidence conditions. Furthermore, it was highlighted that the eigenfrequencies of the first two radiative modes are held constant regardless of the angle of incidence. A relevant change is detected at the first antiresonance, which, as shown in Figure 26, results to be gradually shifted up in frequency as the zenith angle θ increases. This is also associated to a progressive reduction of the impedance magnitude peaks, the greater the angle θ. This last effect, due to sound pressure phase lags on the surface of the sample generated by the oblique wavefront, requires further analyses in order to be properly implemented in the analytical model.

6 Surface impedance of panel absorbers: a numerical validation

In this chapter, the analytical surface impedance of plate-cavity coupled absorbers has been calculated for circular and rectangular samples. As will be highlighted in the following sections, specific acoustic impedances obtained from Eq. 48 and Eq. 72 were coupled in series with the impedances of the backing cavities, in some cases extending the analysis also to multilayered backings with porous layers, which were taken in account by integrating the analytical formulation with the transfer matrix method (Eq. 76). Analytical impedances so calculated were then compared to the normal acoustic impedance of circular and rectangular samples, which were numerically evaluated either as pressure-velocity ratios over the plate surface or by applying the transfer function method [6] to the results of FEM simulations that virtually replicated sound incidence conditions of an impedance measurement test-rig in a standing wave tube. Further analyses were carried out on a square absorber, in order to investigate the validity of the analytical surface impedance formulation also in the case of spherical sound incidence. On this purpose, a hemispherical free-field FEM model was set, in order to simulate diversified sound incidence conditions on a baffled panel absorber.

6.1 Circular panel absorber

A circular panel absorber was tested in order to validate the analytical formulation of its normal surface impedance introduced below. The sample in question, shown in Figure 27, was constituted of a circular and edge clamped aluminum plate (whose geometrical and mechanical properties are listed in Table 4) backed by a 4.5 cm deep air cavity. The normal surface impedance of the coupled system was analytically obtained by adding in series the specific acoustic impedances of a circular clamped plate, as defined in Eq. 48 to that of an air cavity of depth d, as defined in Eq. 73. Combining the two expressions above, yields:

$$\langle Z_S \rangle = \langle Z_p \rangle + Z_a = -j\left(\omega m \cdot \frac{I_1(k_Ba)J_0(k_Ba) + J_1(k_Ba)I_0(k_Ba)}{I_1(k_Ba)J_2(k_Ba) - J_1(k_Ba)I_2(k_Ba)} + Z_0 cot(k_0 d)\right) \tag{115}$$

where $k_B^4 = \frac{\omega^2 m}{D}$ is the *bending wavenumber* of waves propagating through the plate, m is the plate surface mass, a is the plate radius, Z_0 is the characteristic impedance of air, k_0 is the wavenumber in air and d is the cavity depth. The impedance resulting from Eq. 115 was compared to the numerical surface impedance retrieved from a

FEM model replicating the experimental test rig as defined by ISO 10534-2:1998 [6], and applying the transfer function method described in the same standard. A multiphysics FEM simulation was set by modelling a circular edge clamped plate as a shell: the structural-acoustics coupling was assigned by introducing continuity conditions of velocity at the interface between the shell domain and the adjacent air domains, represented by the backing cavity and by the tube segment where an incident plane sound field was assigned as an external excitation. According to Figure 28, the system was discretised by using free triangular elements for the shell domain, whose maximum size was equal to $\lambda_{struct}/10$. Free tetrahedral meshes were employed to discretise air domains and sized according to the $\lambda_{min}/10$ criterion. Normal plane wave incidence conditions were set by assigning an inward normal velocity to the end of the tube corresponding to the loudspeaker diaphragm.

Numerical and analytical impedances are compared in Figure 29, showing a good agreement over frequency, especially at the first resonance occurring at 504 Hz, where a shift of 3 Hz is observable between numerical and analytical curves. Nevertheless, a greater shift of 25 Hz is detectable at the second resonance mode, occurring at 1828 Hz for the FEM solution and at 1854 Hz for the analytical model. Sound absorption peaks around 0.70 are observable at the first and second resonance respectively (Figure 30), in both numerical and analytical results.

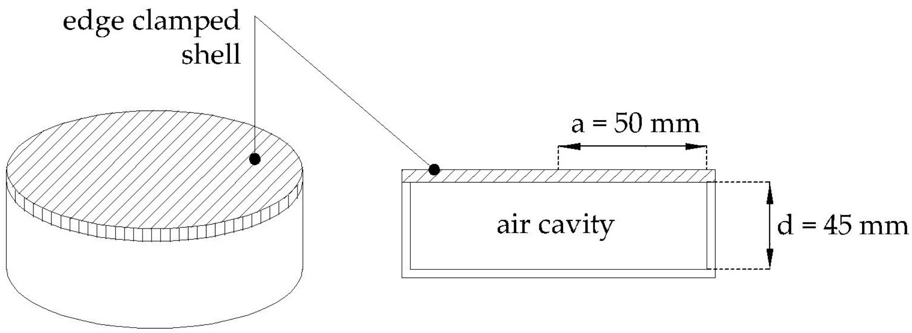

Figure 27: Schematic of the circular panel absorber simulated in FEM.

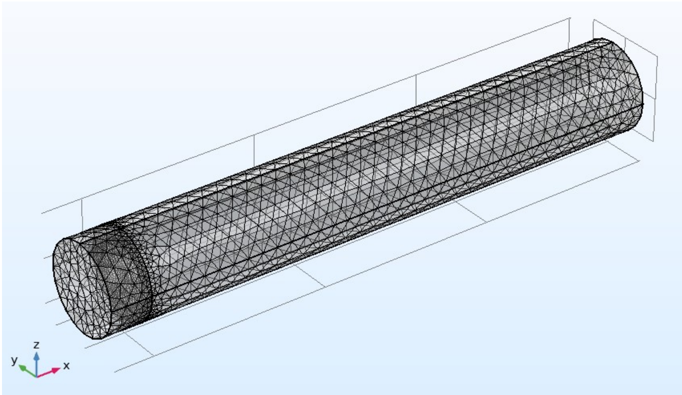

Figure 28: Meshed FEM model of the experimental test-rig as defined by ISO 10534-2:1998 [6]. The shell was meshed using free triangular elements, air domains were discretised by means of free tetrahedral elements according to the $\lambda_{min}/10$ criterion.

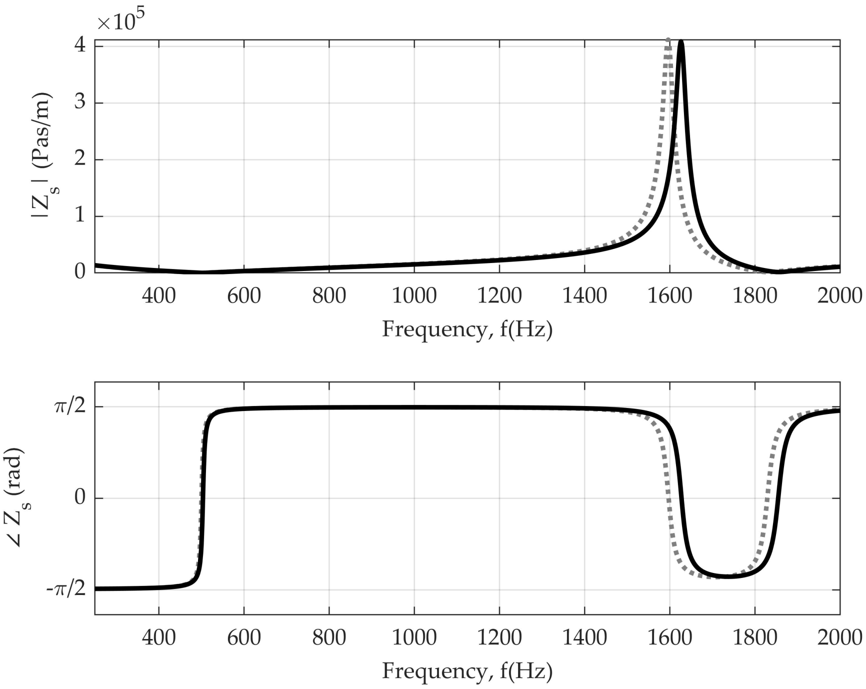

Figure 29: Magnitude and phase of the normal surface acoustic impedance of a circular clamped aluminum plate backed by a 4.5 cm deep air cavity: ——analytical values; ········FEM simulated values.

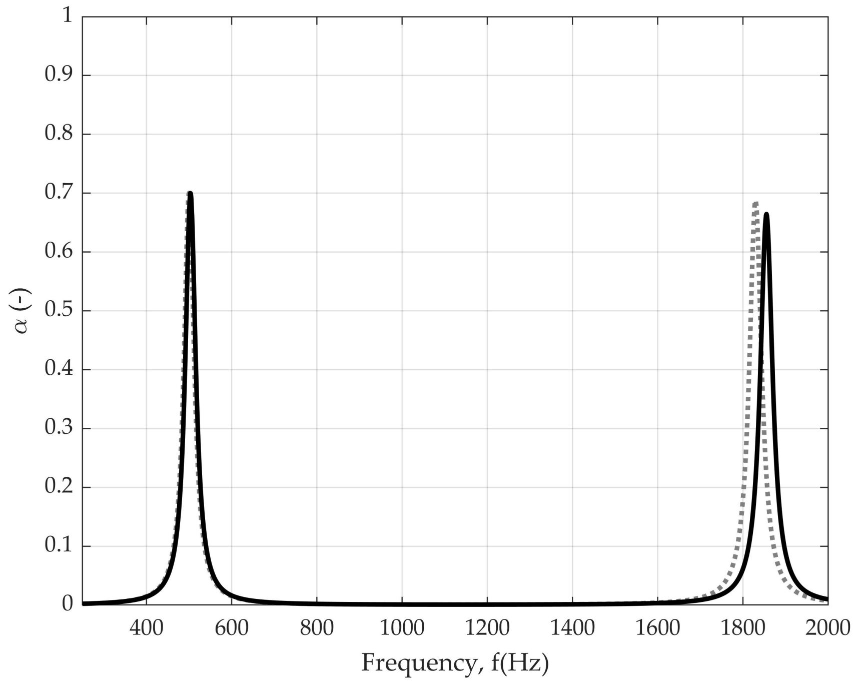

Figure 30: Normal sound absorption coefficient of a circular clamped aluminum plate backed by a 4.5 cm deep air cavity: ——analytical values; ········FEM simulated values.

6.2 Rectangular panel absorber

Similarly to the case of a circular sample, the analytical surface impedance of a rectangular panel absorber was calculated by adding in series the surface averaged acoustic impedance of a clamped rectangular plate, as defined in Eq. 72 and the impedance of a cavity of depth d, yielding the following relationship

$$\langle Z_S \rangle = \langle Z_p \rangle + Z_a = \frac{\int_0^b \int_0^a P(x,y)\,\mathrm{d}x\mathrm{d}y}{j\omega \left\{ \int_0^b \int_0^a \left[\sum_m^\infty \sum_n^\infty \frac{\int_0^b \int_0^a P(x,y) X_m Y_n \,\mathrm{d}x\mathrm{d}y}{D(I_1 I_2 + 2 I_3 I_4 + I_5 I_6) - m\omega^2 I_2 I_6} X_m(x) Y_n(y) \right] \mathrm{d}x\mathrm{d}y \right\}} \tag{116}$$

$$- jZ_0 cot(k_0 d) \tag{117}$$

where the variables involved hold the same meaning introduced in the Subsection 2.4.1.

The impedance so calculated was compared to the numerical impedance evaluated from FEM multiphysics simulations assuming plane wave normal sound incidence upon the surface of the absorber (Figure 34). The latter was constituted of an acrylic rectangular plate, clamped at the edges and coupled to a backing cavity of 3 cm depth. Geometrical and mechanical properties of the absorber are summarized in Figure 31 and Table 6. This test-rig was modeled in FEM by setting up a multiphysics simulation where the thin plate was defined as an edge clamped shell and the structural-acoustics coupling conditions to the adjacent air volumes was achieved by applying velocity continuity conditions. The resulting normal acoustic impedance was evaluated as the surface averaged pressure-velocity ratio at the plate-air interface towards the domain of the incident sound field.

Analytical and numerical surface impedances and absorption coefficients are compared in Figures 32 and 33. As noticeable from the graphs, the curves are in good agreement in terms of amplitude and resonance frequencies: in particular, a shift of 2 Hz is observable between the analytical and numerical solution at the first resonance frequency occurring at 319 Hz. Figure 34 shows the numerical pressure distribution within the backing cavity and external air volumes and the transverse velocity distribution over the shell surface at the first resonance frequency: as visible from the plots, the shell vibrates according to the first radiative modeshape (1,1) of a rectangular clamped plate – occurring at 238 Hz in the case of uncoupled conditions – achieving the maximum amplitude of transverse displacement at the center of the surface, consequently transmitting sound energy into the backing cavity. Given that, a sound absorption peak of 0.47 is observable in Figure 33. A further absorption peak, related to the second radiative plate mode (3,1), is observable at 568 Hz. At this point, it is interesting to evaluate the effect of the air backing cavity onto the resulting acoustic impedance of the whole coupled system with respect to the specific acoustic impedance calculated for the isolated plate vibrating in uncoupled conditions. As visible from Figure 32, the first flexural mode (1,1) of the uncoupled clamped plate occurring at 238 Hz is shifted up to 319 Hz, when coupling the plate to a narrow air cavity. A smaller shift is also observable at the second mode (3,1), which is shifted up in frequency of 10 Hz. This phenomenon is due to the additional stiffness provided by the air spring represented by the backing cavity, which should be narrow enough to ensure an adequate bulk stiffness, namely preventing transverse acoustic modes occurring within its volume. Given that, according to equation 116, narrower cavities will increase the frequency shifting effect, whilst wider cavities will reduce it or at most cancel it out, when the cavity volume is big enough to allow for transverse standing waves to occurr in the frequency range of interest.

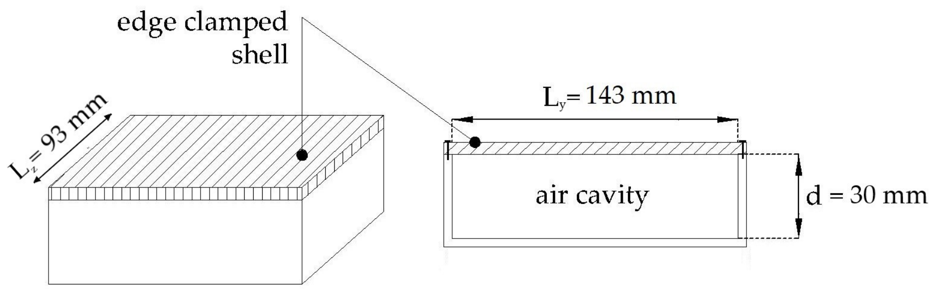

Figure 31: Schematic of the rectangular panel absorber simulated numerically.

$L_y[mm]$	$L_z[mm]$	$h\ [mm]$	$E\ [GPa]$	$\nu[-]$	$\eta\ [-]$	$\rho\ [kgm^{-3}]$
143	93	1	2.89	0.35	0.02	1190

Table 6: Geometrical and mechanical properties of the rectangular acrylic plate: $L_x$and L_y (side lengths), h (thickness), E (elastic modulus), ν (Poisson's ratio), η (material loss factor), ρ (mass density).

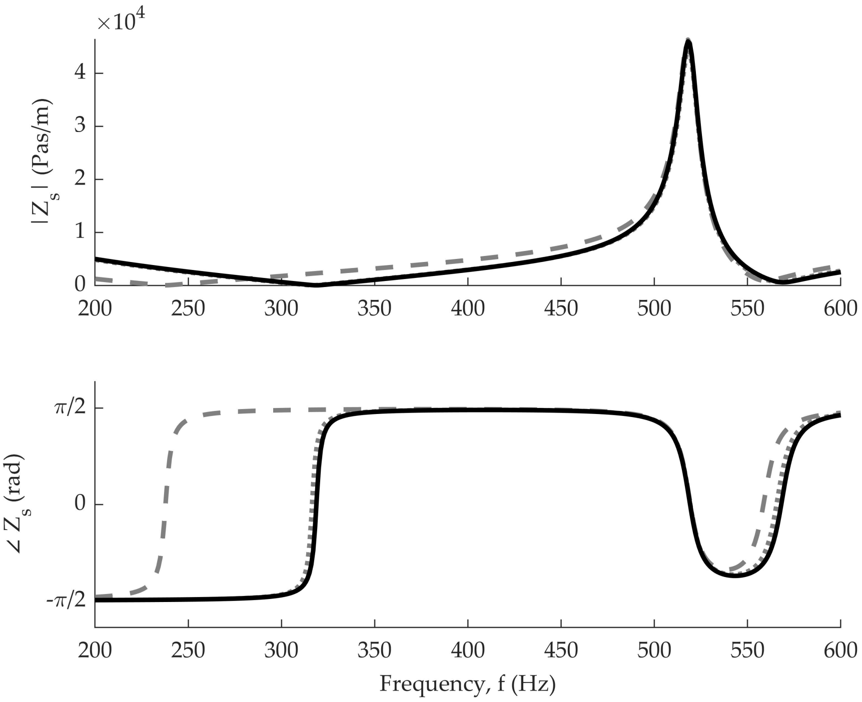

Figure 32: Magnitude and phase of the normal surface acoustic impedance of a rectangular clamped acrylic plate backed by a 3 cm deep air cavity: ——analytical values; ········ FEM simulated values. — — · analytical acoustic impedance values of the uncoupled plate.

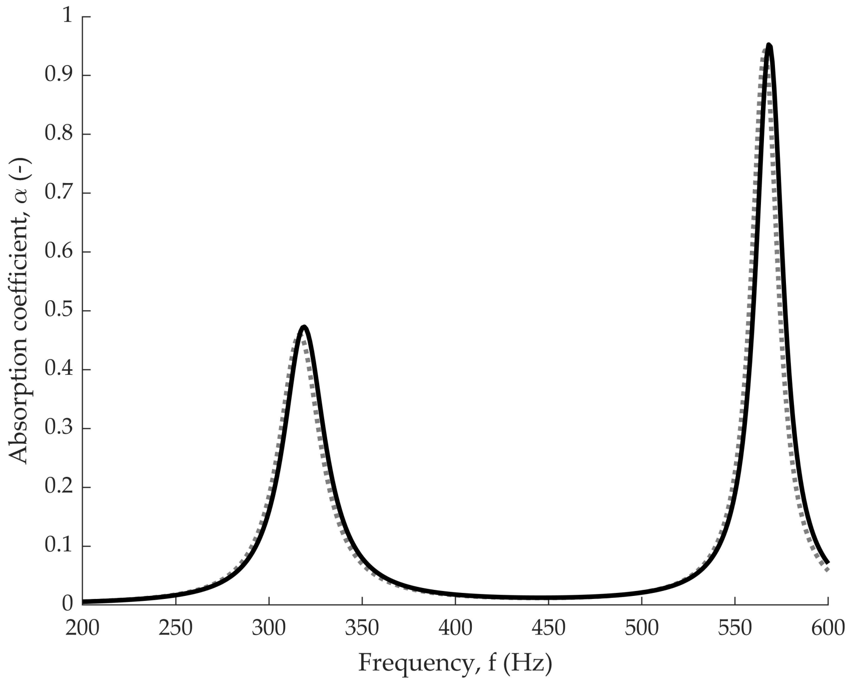

Figure 33: Normal sound absorption coefficient of a rectangular clamped acrylic plate backed by a 3 cm deep air cavity: ——analytical values; ········ FEM simulated values.

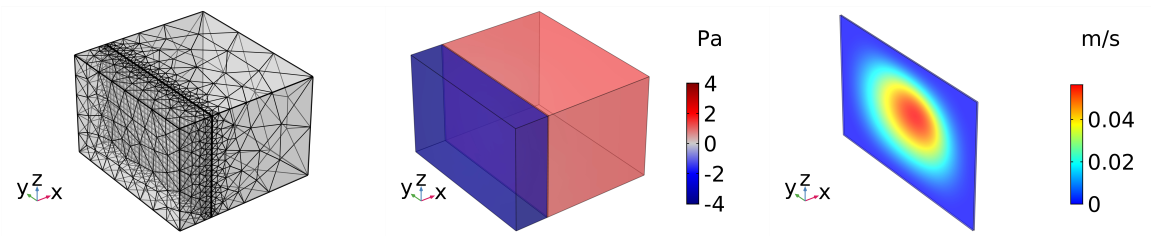

Figure 34: Left hand side: meshed 3D domain: quadratic mapped elements were used for the shell, air domains were meshed by using free tetrahedral elements; in the middle: distribution of the total acoustic pressure within cavity and external air domains at 319 Hz; right hand side: transverse velocity distribution over the shell surface at 319 Hz.

6.2.1 Effects of porous layers within the backing cavity

A further numerical analysis was conducted in order to investigate the effects of partially filling the air cavity with a layer of porous material. In this case, the sample tested in the analysis above was updated by adding a 1.5 cm thick layer of porous material into the cavity, with air flow resistivity $\sigma = 5000$ rayls/m, placed in contact with the rigid end of the backing cavity, as shown in Figure 35. In such a way, the thickness of the air layer, adjacent to the thin plate, was halved to 1.5 cm. A FEM simulation with the same setup as the case above was carried out, in order to calculate the resulting surface averaged acoustic impedance. The analytical model of a multilayered backing with a layer of porous material partially filling the air cavity was accounted for, by applying the transfer matrix method according to Eq. 76. In this case, the surface averaged acoustic impedance $\langle Z_S \rangle$ becomes:

$$\langle Z_S \rangle = \langle Z_p \rangle + Z_{a,2} = \frac{\int_0^b \int_0^a P(x,y)\, \mathrm{d}x\mathrm{d}y}{j\omega \left\{ \int_0^b \int_0^a \left[\sum_m^\infty \sum_n^\infty \frac{\int_0^b \int_0^a P(x,y) X_m Y_n \, \mathrm{d}x\mathrm{d}y}{D(I_1 I_2 + 2 I_3 I_4 + I_5 I_6) - m\omega^2 I_2 I_6} X_m(x) Y_n(y) \right] \mathrm{d}x\mathrm{d}y \right\}} \tag{118}$$

$$- \frac{Z_{a,1} j Z_0 cot(k_0 d) + \rho_0^2 c_0^2}{Z_{a,1} - j Z_0 cot(k_0 d)},$$

where $Z_{a,1} = -jZ_{por} cot(k_{por} d_{por})$ is the surface impedance at the interface between the porous layer and the air gap, with Z_{por} and k_{por} were calculated from Miki model and d_{por} is the thickness of the porous material.

A comparison between the absorber with and without porous layer within the cavity is shown in Figures 36 and 37 in terms of surface impedance and absorption coefficient. As noticeable from the graphs, the first resonance peak was shifted down in frequency of 9 Hz, whilst a slighter frequency downshift of 1 Hz is observed at the second resonance. Additional dissipation is provided at the first resonance frequency, increasing the sound absorption peak from 0.46 to 0.87. On the other hand, sound absorption at the second resonance was slightly decreased from 0.94 to 0.89. These results suggests that:

- the more the acoustic damping is increased into the backing cavity by placing a layer of porous material within its volume, the less the stiffness of the air layer is dominant, slightly shifting down the resonance frequencies of the system towards the eigenfrequencies of the plate modes in uncoupled conditions;
- sound absorption at eigenfrequencies corresponding to the higher order modes of the plate, which are not significantly affected by the air cavity stiffness in coupled conditions, is slightly decreased when adding a porous layer within the cavity;
- sound absorption at the eigenfrequencies of the plate which are significantly affected by the stiffness of the backing cavity in coupled conditions, is significantly increased when adding a porous layer within the cavity.

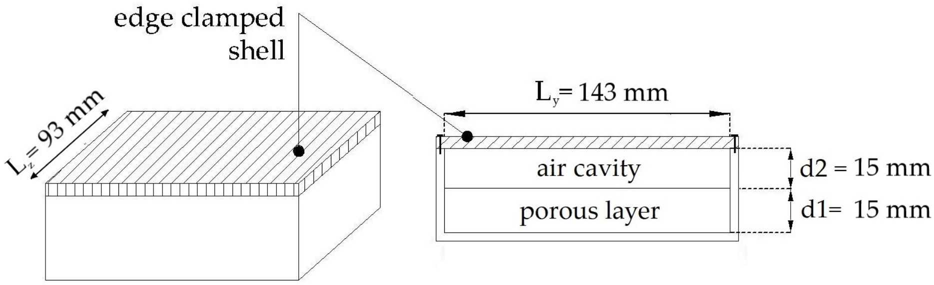

Figure 35: Schematic of the rectangular panel absorber with a porous layer partially filling the air cavity, simulated numerically.

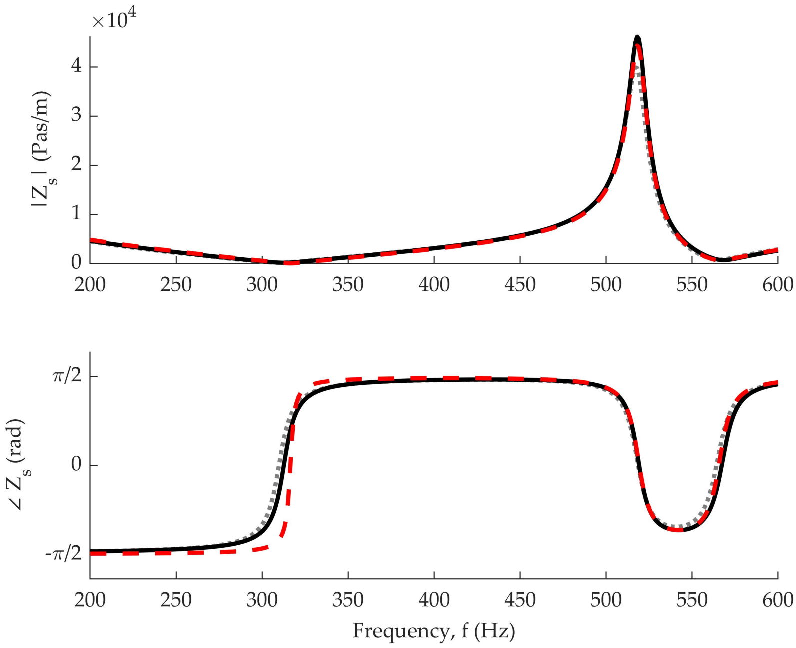

Figure 36: Magnitude and phase of the normal surface acoustic impedance of a rectangular clamped acrylic plate backed by a 1.5 cm deep air cavity and 1.5 cm thick layer of porous material ($\sigma = 5000$ rayls/m): ——analytical values; ········ FEM simulated values. – – · numerical acoustic impedance values of the panel absorber without porous layer (3 cm air cavity).

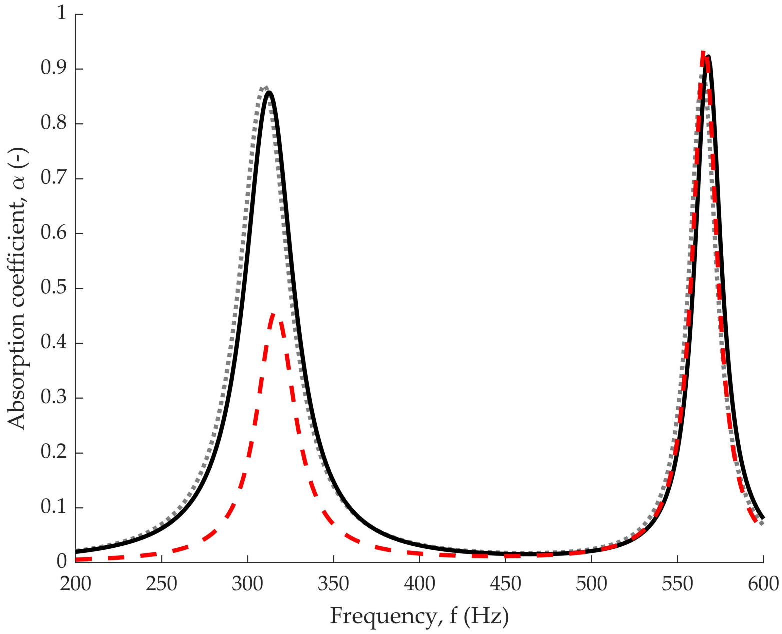

Figure 37: Normal sound absorption coefficient of a rectangular clamped acrylic plate backed by a 1.5 cm deep air cavity and 1.5 cm thick layer of porous material ($\sigma = 5000$ rayls/m): ——analytical values; ········ FEM simulated values. – – · numerical absorption coefficient of the panel absorber without porous layer (3 cm air cavity).

In order to find out how such a damping effect may be enhanced, a numerical parametric analysis was conducted by increasing either the thickness or the air flow resistivity of the porous layer, changing those quantities in turn. At a first instance, the surface impedance was calculated for the same panel absorber configuration as depicted in Figure 35, leaving unaltered the thickness d_1 of the porous layer and by choosing among a set of different values of air flow resistivity σ equal to 2000 rayls/m, 5000 rayls/m and 10000 rayls/m, which represent plausible values of σ for porous materials commonly used in acoustic applications. Sound propagation within the porous layer volume was again modelled by resorting to the Miki model [29]. In Figure 38, the trend of the normal sound absorption coefficient is depicted, showing negligible effects due to the variation of flow resistivity, in terms of frequency shifting and absorption. For the sake of clarity, the resulting resonance frequencies and absorption coefficient peaks for each value of air flow resistivity are summarized in Table 7.

An additional parametric numerical analysis was carried out by choosing different thicknesses of the porous layer among values of d_1 equal to 0.5 cm, 1.5

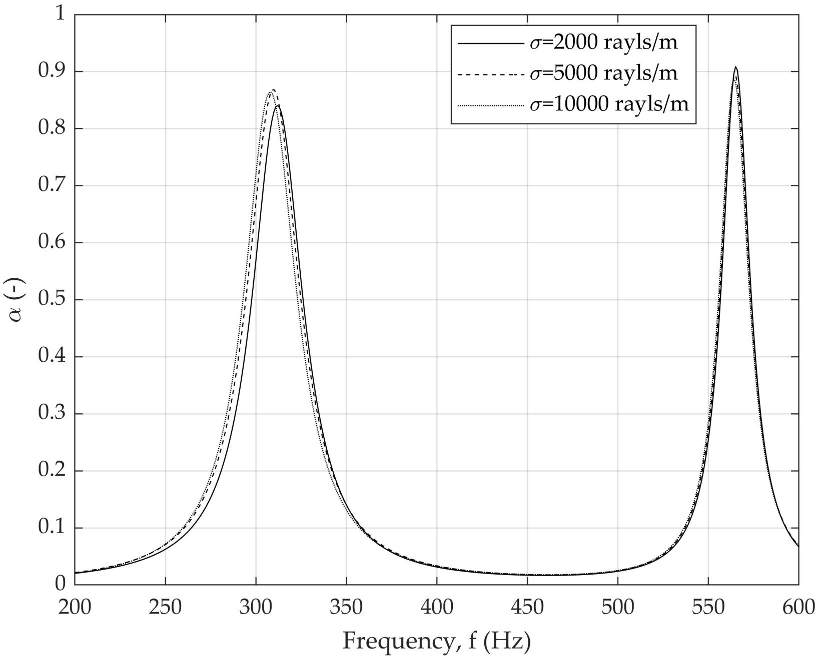

Figure 38: Normal sound absorption coefficient of a clamped rectangular acrylic plate backed by a 1.5 cm deep air gap and a 1.5 cm thick layer of porous material with different values of air flow resistivity σ.

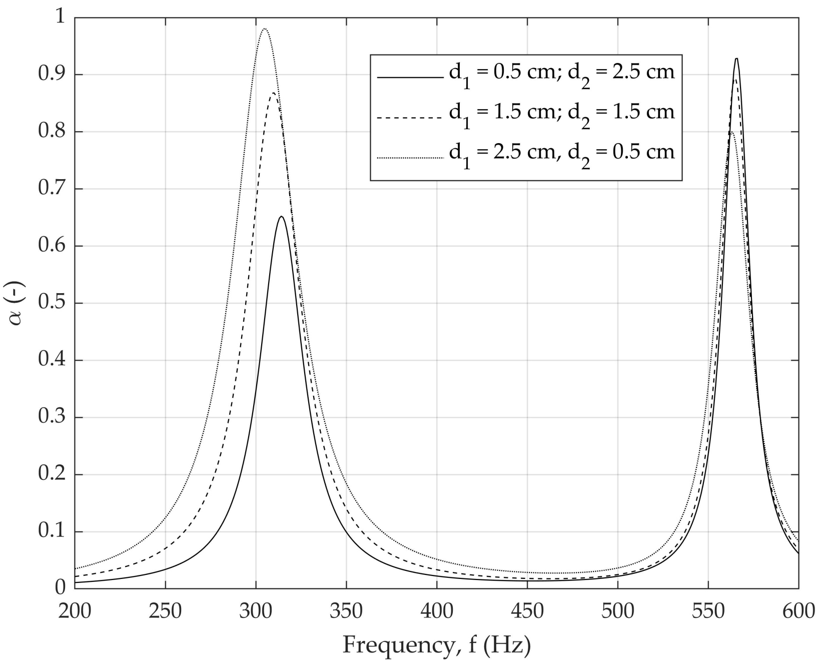

Figure 39: Normal sound absorption coefficient of a clamped rectangular acrylic plate backed by an air layer d_2 and a porous layer d_1. Values are reported for different values of d_1 and d_2.

$d_1[cm]$	$\sigma[rayls/m]$	$f_{res,1}$ $[Hz]$	α at $f_{res,1}$ $[-]$	$f_{res,2}$ $[Hz]$	α at $f_{res,2}$ $[-]$
1.5	2000	312	0.84	565	0.90
1.5	5000	310	0.87	565	0.89
1.5	10000	308	0.86	564	0.89

Table 7: First and second resonance frequencies and related sound absorption for different values of the air flow resistivity of the porous layer d_1.

$d_1[cm]$	$d_2[cm]$	$\sigma[rayls/m]$	$f_{res,1}$ $[Hz]$	α at $f_{res,1}$ $[-]$	$f_{res,2}$ $[Hz]$	α at $f_{res,2}$ $[-]$
0.5	2.5	5000	314	0.65	566	0.93
1.5	1.5	5000	310	0.87	565	0.89
2.5	0.5	5000	305	0.98	563	0.80

Table 8: Sound absorption values at the first and second resonance frequencies for different values of thickness of layers d_1 and d_2.

cm and 2.5 cm, and accordingly varying the air layer thickness d_2 in order to keep the depth of the whole cavity $d_1 + d_2$ equal to 3 cm, as shown in Figure 35. FEM simulations were performed by leaving unaltered the model setup used for previous analyses, and air flow resistivity σ was kept constant to 5000 rayls/m. Results in terms of sound absorption coefficient are shown in Figure 39 and summarized in Table 8: as noticeable, significant effects are observed in terms of frequency shifting and absorption peak variations when changing the thickness of the porous layer. In particular, being equal the thickness $d_1 + d_2$, an increase of the porous layer thickness d_1 implies a downshift of resonance frequencies, enhancing sound absorption at the first mode and decreasing it at the second resonance. Vice versa, a decrease of the porous layer d_1 shifts up the eigenfrequencies, decreasing absorption at the first resonance and increasing it at the second one. A progressive reduction of the porous layer thickness d_1 implies the resulting impedance and absorption coefficient approach those of a rectangular panel backed by a 3 cm air cavity, reported in Figures 32 and 33.

6.3 Numerical investigation on the resonator response to spherical sound incidence

Alongside the validation of the surface averaged impedance of panel aborbers for normal plane wave incidence, a numerical analysis was performed in order to investigate the response of a square panel absorber under spherical wave excitation and consequently the effects of such a wavefront on the resulting surface impedance evaluated as a pressure-velocity ratio over the surface of the panel. In particular, a set of FEM simulations was carried out by simulating the acoustical excitation of such a panel, inserted in a rigid baffle in order to minimize edge effects, by a

L [cm]	d [cm]	h [cm]	E [GPa]	$\nu[-]$	η [$-$]	ρ [kgm^{-3}]	d_1 [cm]	d_2 [cm]
45	10	0.50	3.7	0.25	0.05	760	5	5

Table 9: Geometrical and mechanical properties of the square absorber composed by a MDF plate coupled to a multilayered porous-air backing cavity: L (side length), h (plate thickness), E (elastic modulus), ν (Poisson's ratio), η (material loss factor), ρ (mass density), d_1 (thickness of the porous layer), d_2 (depth of the air gap).

monopole source placed at different heights above the panel in free field. Geometrical and mechanical properties of the absorber are summarized in Table 9.

The square shape of the absorber was chosen in order to ensure geometrical symmetry of the test-rig. This was simulated by modelling a hemispherical air domain of radius equal to 1.80 m, surrounded by a perfectly matched layer (PML), which ensures the minimization of sound reflections occurring at the boundaries of the model (Figure 41). As in the case of Section 5.2, the efficiency of PML was validated against analytical relationships, by comparing the numerical sound pressures evaluated at several points assuming a perfectly rigid floor to the pressure values calculated analytically at the same points. The increased overall dimension of the absorber, with respect to those analyzed in the previous investigations, was chosen in order to provide a sufficient sound pressure variation along the surface of the plate, in light of the spherical wavefront. A preliminary evaluation of such variation was performed analytically by gradually increasing the height of the monopole source. The resulting sound pressure was calculated along the x direction from the center point to the edge of the plate according to the following relation:

$$p(x) = \frac{A}{r} sin(\omega t - kr) \tag{119}$$

where A is the pressure amplitude of the spherical wave, t is time, k is the wavenumber in air, ω is the angular frequency and r is calculated as $\sqrt{x^2+h^2}$ according to the schematization depicted in Figure 40. According to this, the variation of sound pressure levels along the x direction on the surface of the plate was calculated as follows:

$$\triangle L_p(x) = |L_p(x) - L_p(0)|\,. \tag{120}$$

Such variations are reported in Figure 42, at 50 Hz for different source heights, namely 0.20 m, 0.40 m, 0.60 m, 1.20 m and 1.50 m, along the direction normal to the panel and passing through its center.

Considering those source heights, a set of FEM simulations was performed according to the model setup depicted in Figure 41. For each simulation the averaged

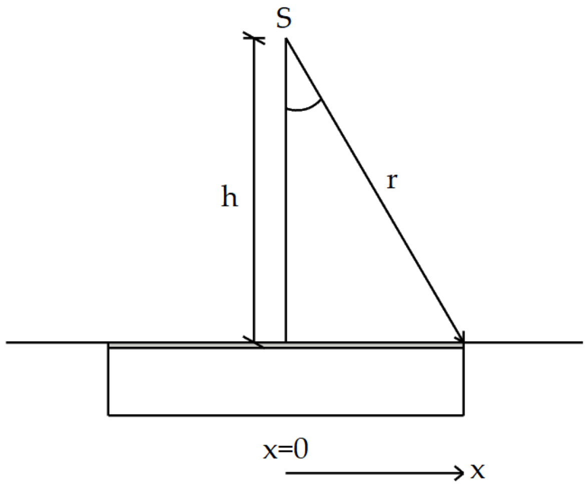

Figure 40: Monopole source S placed at a height h from the top surface of the absorber. Sound pressure is calculated at several points along x, as a function of the distance r.

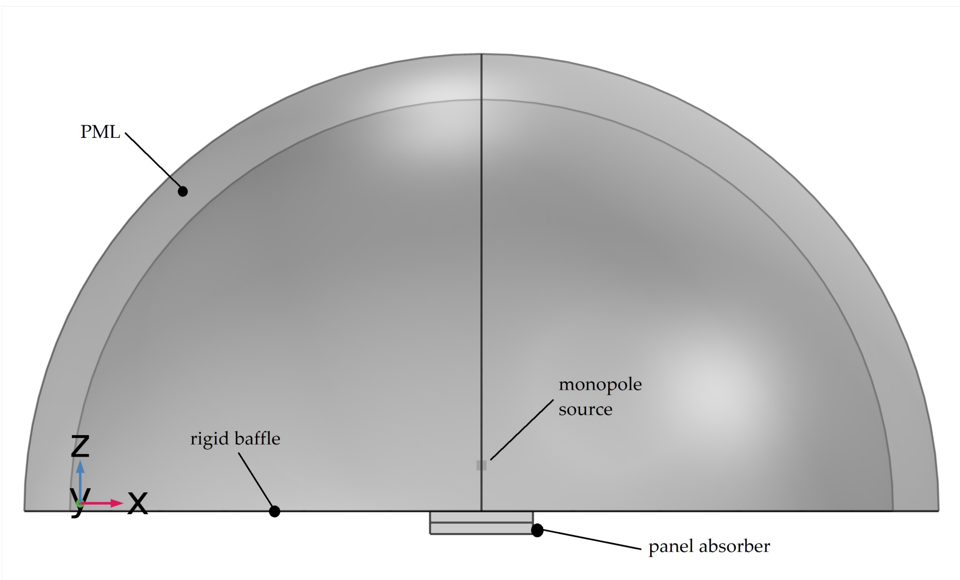

Figure 41: Three dimensional FEM model setup of a monopole source radiating over a baffled panel absorber in free field conditions. The hemispherical air domain of 1.80 m radius is surronded by a Perfectly Matched Layer (PML) to prevent sound reflection from the boundaries.

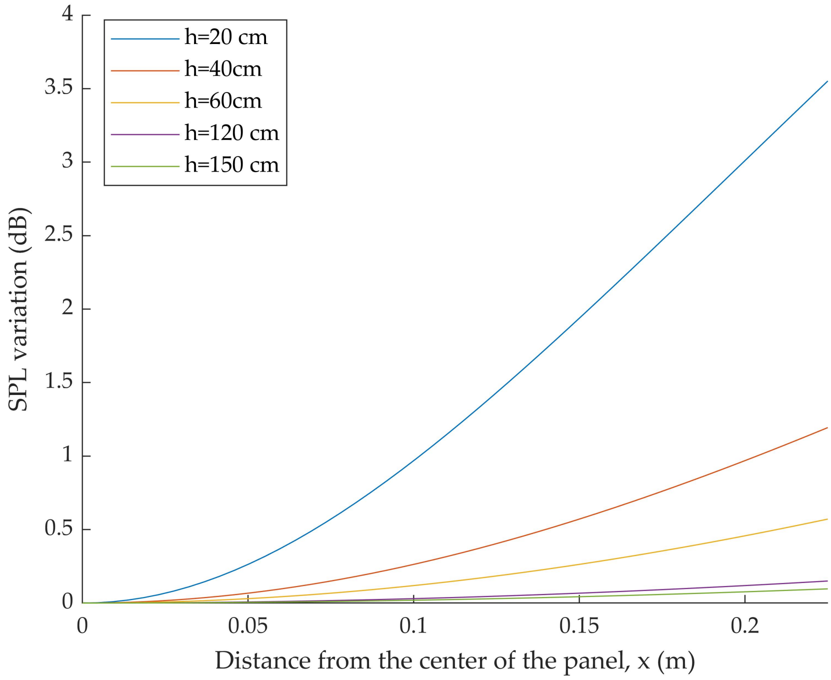

Figure 42: Sound Pressure Level variation calculated at different distances from the center of the panel for several heights of a monopole source radiating at 50 Hz.

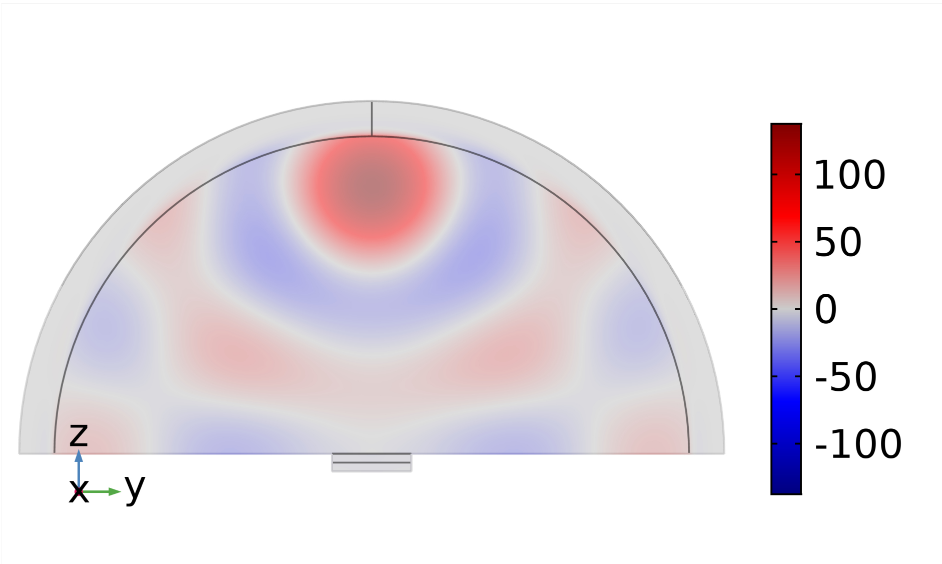

Figure 43: Distribution of the total sound pressure field [Pa] in the three dimensional FEM model of a monopole radiating over a baffled panel absorber in free field conditions. For the case in Figure, the source was placed at a height $h = 1.50$ m.

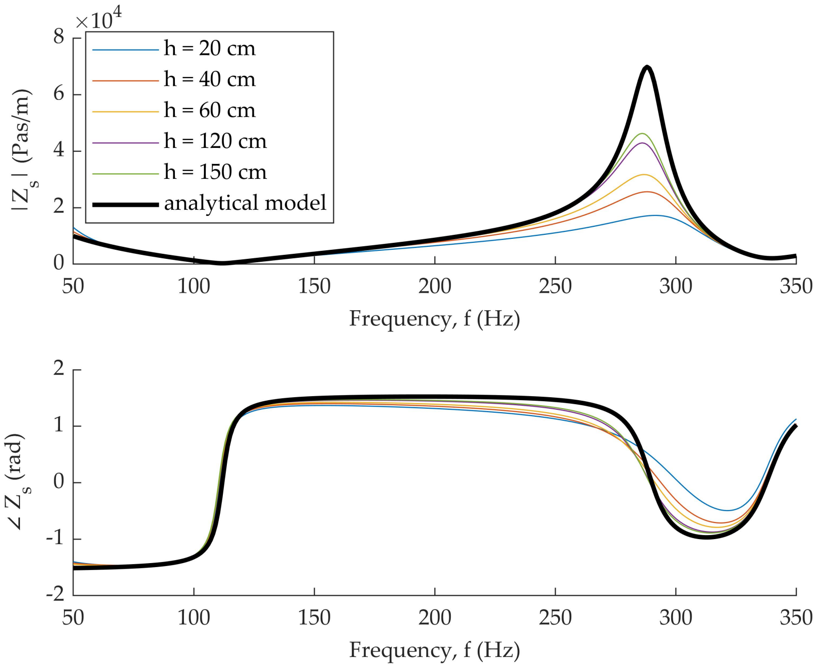

Figure 44: Comparison of the surface averaged analytical impedance of the panel absorber against those evaluated from the free field FEM model for several heights of the monopole source.

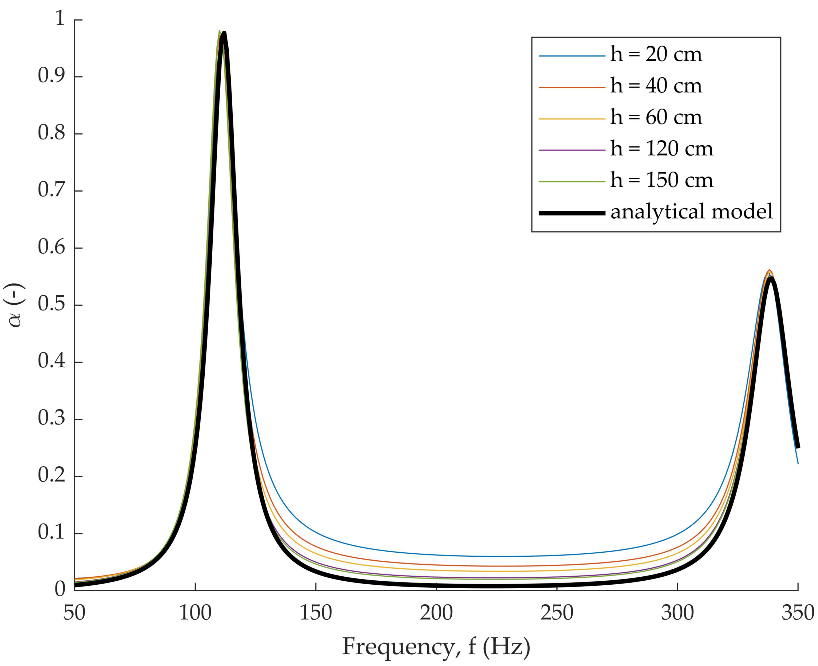

Figure 45: Comparison of the analytical absorption coefficient of the panel absorber against those evaluated from the free field FEM model for several heights of the monopole source.

surface impedance of the absorber was calculated as the average pressure-velocity ratio over the surface of the panel. Such numerical impedances are compared in Figure 44 against the analytical impedance, calculated according to Eq. 118. Results are also shown in terms of absorption coefficients in Figure 45.

The results shown in the graphs provide some insights on two main effects:

- surface impedance and absorption coefficients show no significant variations in correspondence of the panel resonance frequencies, holding the same values of absorption peaks regardless of the source height;
- relevant effects are observable in proximity of the antiresonance occurring at 289 Hz, where the impedance becomes smaller the closer the monopole source to the absorber top surface.

As expectable, the latter point may be attributable to phase lag effects due to the spherical wavefront, which do not occur in the case of a plane wave normal incidence. Nevertheless, some further analytical and experimental investigations are in progress, in order to thoroughly analyze the relationship between direct and scattered sound pressure fields in proximity of the absorber surface. However, the unchanged acoustic behaviour of the panel around resonance frequencies is promising with regards to the potential of the analytical model to account for different conditions of sound incidence.

Part III

Real room case study

Sound absorption of acoustic resonances in the low modal density region of enclosed spaces has been extensively studied over time and still presents a challenging topic with reference to room acoustics predictive analyses. As it is well known, geometrical acoustics simulation techniques [31, 32] do not account for wave propagation effects resulting from the interaction of sound waves with room boundaries. Numerical methods such as FEM [33, 34], BEM [35, 36, 37] or FDTD [38, 39] are necessary to achieve an acceptable degree of reliability, especially in the case of arbitrarily shaped rooms. In particular, in FDTD simulations, immersed boundary methods seem to be a promising approach to model complex impedance surfaces [40, 41]. To this end, an exhaustive definition of a complex and frequency dependent acoustic impedance at room boundaries is required. While this has been achieved with acceptable accuracy for porous absorbers [42, 43, 44], a certain degree of uncertainty is still present in the case of resonant panel absorbers. Nevertheless, the latter represent one of the most employed solutions for low frequency room modes absorption, due to their affordable cost, ease of construction and compliance with architectural constraints. As described in the chapters above, such systems are generally composed of an impervious flexible plate backed by a sealed air cavity, which must be narrow enough to ensure an adequate bulk stiffness, namely preventing transverse acoustic modes occurring within its volume. Usually, the cavity is partially filled with a layer of porous material to provide additional damping and broaden the spectrum of sound absorption around resonance frequencies. As a result, sound energy is dissipated by means of either flexural damping – due to the panel bending – or by thermoviscous losses occurring throughout the porous layer. In order to allow for a proper vibroacoustic excitation of the plate, panel absorbers must be placed at high sound pressure areas in the room – usually corners and/or rigid walls: this way, the particle velocity profile in the cavity becomes sufficiently high to ensure the effectiveness of the porous material in terms of sound absorption. The analytical frequency expression of the surface averaged acoustic impedance of rectangular panel absorbers, calculated as described in the chapters above, was numerically validated for plane wave normal incidence conditions. From now on, the applicability of such an expression as an impedance boundary condition into FEM room acoustics models will be investigated experimentally and numerically. In particular, the acoustic behaviour of an existing cuboid room has been studied and a FEM model was built and validated against room impulse response measurements carried out at several receiver positions within the room. Once the modal behaviour of the empty room was analyzed and the main eigenmodes were identified, two configurations of acoustic treatment were proposed, based on the use of panel absorbers. Treated room FEM models were then validated against experimental measurements, similarly to the case of the empty room configuration. The main assumption underlying this investigation relies on the fact that the actual surfaces corresponding to the panel absorbers were assigned with a frequency dependent and surface averaged acoustic impedance, calculated for normal incidence conditions and assuming the surface to behave as a locally reacting material, namely implying that surface impedance is not dependent on the angle of incidence. If such an hypothesis may lead to significant errors in some cases [45], it is also true that the sound field in rooms at lowest frequency eigenmodes generates wide areas where sound pressure distribution is uniform in proximity of the boundary surfaces. In light of this, although some errors can be expected and would need further investigation, the use of this methodology, when properly validated (as in this case), may help to circumvent the need of performing multiphysics simulations, which imply considerably higher computational costs. In the following chapters, the empty room FEM model validation, the design of the acoustic treatment, discussion of results, limitations of the method and its possible improvements will be addressed.

7 Experimental validation of an empty room FEM model

For this numerical-experimental analysis, an existing cuboid room, acoustically untreated, was chosen in the premises of the Acoustics and Audio Communication Department of the Technische Universität of Berlin, in the context of a joint research project. The surface extension of the room was equal to 21.7 m^2 and its volume equal to 60.7 m^3. Most of the boundary surfaces were acoustically rigid: a tiled ceramic floor, 4.6 m^2 of glazing and two concrete walls were present in the room (Figure 46). False ceiling and two perimeter walls were consisting of plasterboard, and the possible presence of porous materials within their cavity backing was not investigated, since not relevant for the scope of the experiment. The room was chosen due its regular shape and small volume, which allows to observe a strong modal behaviour and well defined modeshapes at frequencies below 200 Hz, in order to appreciate the effect of panel absorbers to be designed with the aim of damping low frequency eigenmodes.

Figure 46: Pictures of the empty room from two different points of view.

7.1 Room Impulse Response measurements

Room impulse response measurements were performed at three receiver points randomly distributed throughout the room (Figure 47), one of them being placed at a corner, in order to properly identify the highest number of room resonance frequencies. The acoustic equipment used to perform measurements consisted of a Norsonic Nor276 dodecahedron with a frequency response defined in the 50-5000 Hz range; a Norsonic Nor280 power amplifier; a NTI MA220 omnidirectional microphone connected to a digital audio interface for signal acquisition. The sound

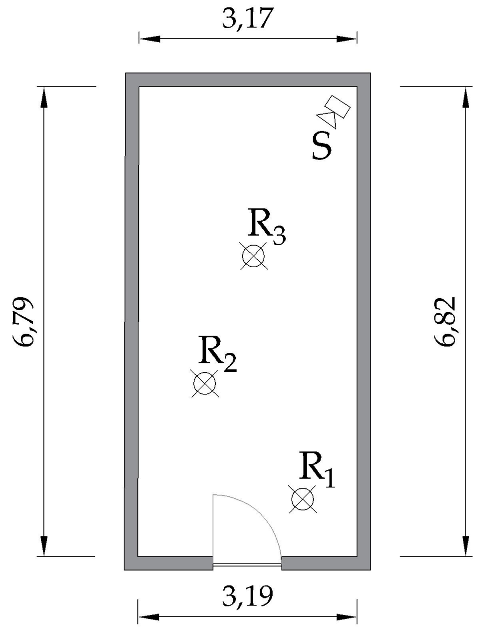

Figure 47: Plan section of the empty room with side dimensions (expressed in m) and source and receivers positions.

power level response of the loudspeaker provided by the manufacturer is reported in third octave bands in Figure 48. An exponential sine sweep defined in the 20-2000 Hz range was used as a test signal, with a sample rate of 48 kHz. Source and receiver positions are shown in the plan section in Figure 47: the source height was fixed at 0.40 m whilst receivers were placed at a 0.65 m height, in order to excite and detect as best as possible the peaks of sound pressure level responses associated to room modes.

7.2 FEM model setup

A three-dimensional acoustic FEM model was then set up, according to the room geometry: the acoustic air domain was meshed using tetrahedral according to the $\lambda_{min}/6$ rule of thumb (Figure 49), assuming all the boundaries to behave as sound rigid surfaces. Unknown acoustic damping already present in the room was taken in account according to a procedure proposed by Roozen et al. [46]: a frequency dependent acoustic loss factor was extracted from reverberation time measurements, according to the following relationship:

$$\xi = \frac{ln(10^6)}{2\omega T_{30}} \approx \frac{1.1}{fT_{30}}. \tag{121}$$

This expression is equivalent to a relation proposed by Cremer [9] to calculate the structural loss factor η of a harmonically vibrating structure as a function

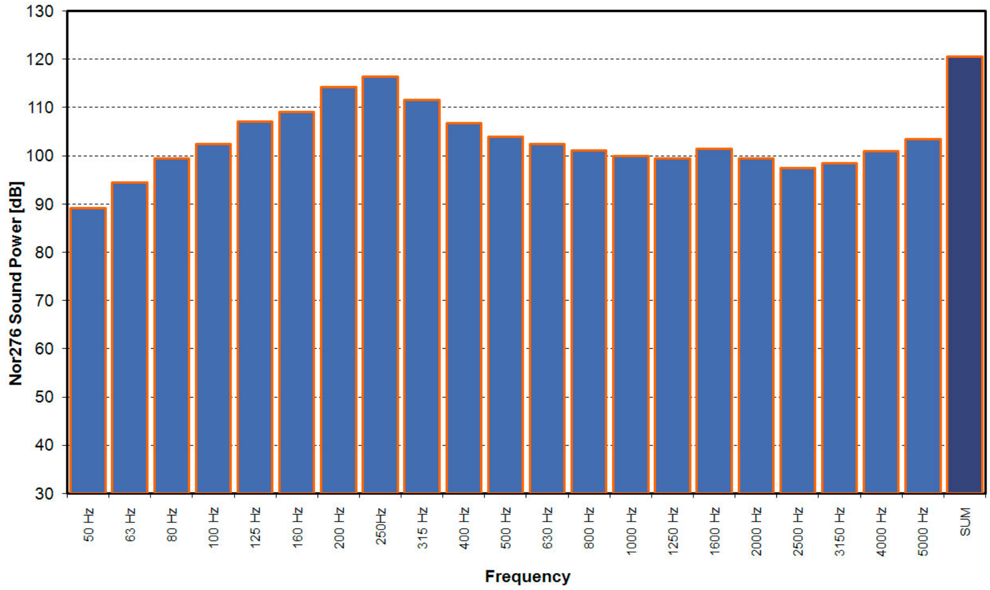

Figure 48: Sound power level frequency response of the Norsonic Nor276 dodecahedron, expressed in third octave bands. Taken from the manufacturer website: https://web2.norsonic.com/product_single/dodecahedron-loudspeaker-nor276/.

of T_{struct}, which is the time required for the structure to dissipate its vibrational energy to one-millionth of its initial value. The acoustic loss factor was then included into a complex sound wave velocity defined in the FEM acoustical domain, as follows:

$$c = c0(1 + j\bar{\xi}) \tag{122}$$

where $\bar{\xi}$ is the loss factor averaged among all the receiver positions within the room. The complex sound speed frequency expression was defined by using a piecewise cubic interpolation function across the third octave bands values retrieved from T_{30} measurements. Although it relies on non trivial assumptions, this methodology is generally useful to calibrate FEM models, including sources of unknown damping already present in the room, without the need of performing multiphysics simulations.

7.3 Results and discussion

The experimental validation of the FEM room model was achieved by comparing the measured sound pressure level responses against those evaluated numerically at the same receiver positions. Results are shown in the 50-200 Hz frequency range: lower and upper limits were respectively chosen due to the lower frequency limit of the loudspeaker response and to the fact that panel absorbers were supposed to exhibit

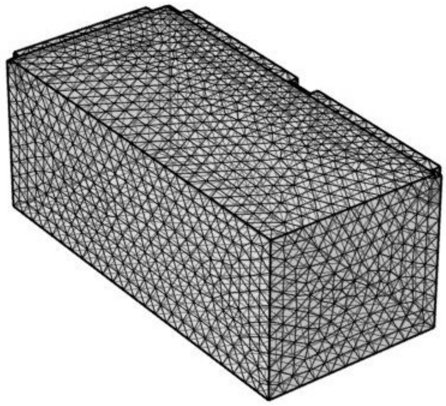

Figure 49: Meshed tridimensional model of the empty room: as a purely acoustical FEM model, the air domain was meshed according to the $\lambda_{min}/6$ criterion.

their highest efficiency at the first few room modes, occurring far below 200 Hz. In Figure 50, numerical and measured full scaled sound pressure level (SPL) responses are compared at each receiver, both normalized with respect to the maximum value of the experimental curve. A reasonable agreement between them is observable across their trend with peaks and troughs, which correspond to acoustic resonances and antiresonances. A quantitative error analysis was performed, showing that the frequency averaged deviation between measured and numerical responses at each receiver is always smaller than 4 dB. In this preliminary error analysis, possible effects due to the loudspeaker response were not taken in account. A more detailed analysis has been carried out and discussed later on. In light of this validation, the FEM model of the empty room was used as a basis for subsequent simulations of the treated room, holding the complex sound velocity function previously defined to take in account unknown existing acoustic damping.

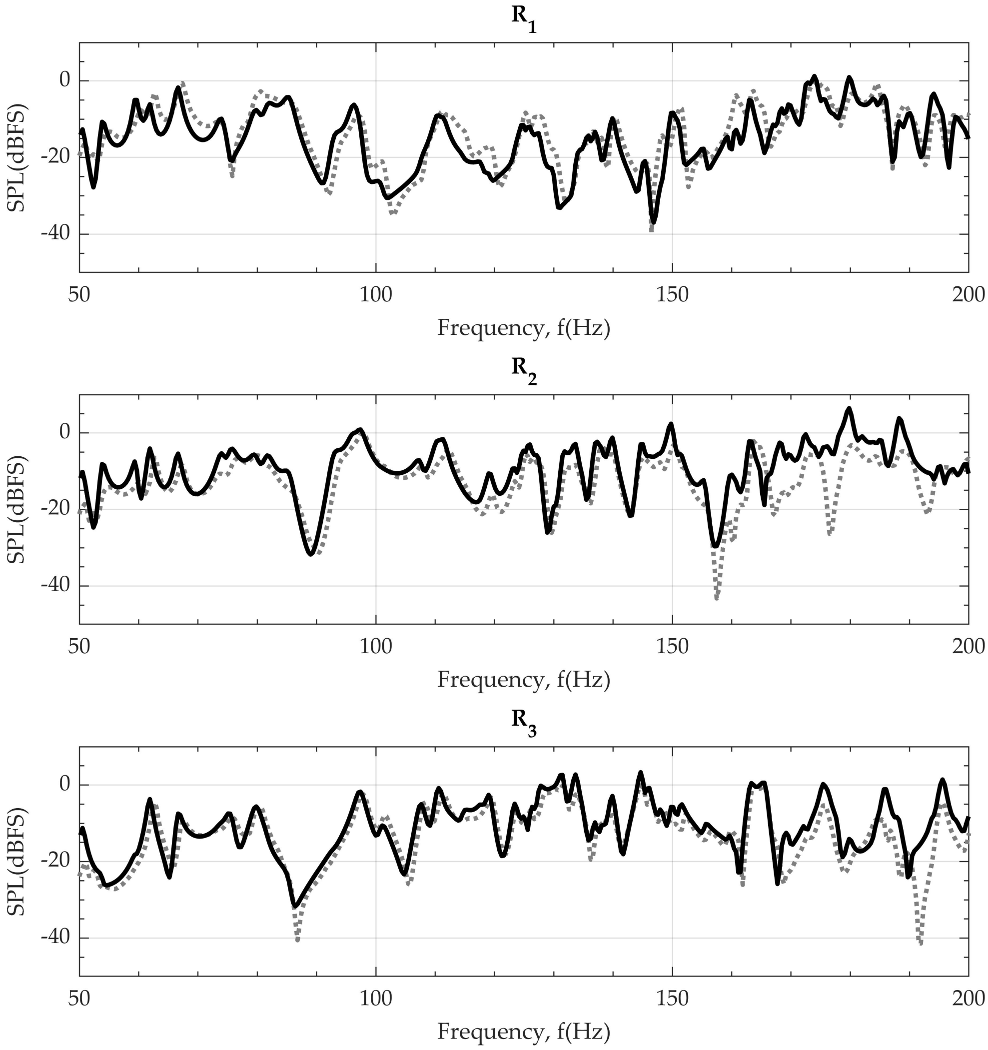

Figure 50: SPL full scaled frequency responses at receiver positions for the empty room configuration at receivers R1, R2 and R3. .... measured values; —— simulated values.

8 Design of panel absorbers for acoustic treatment at low frequency

Once the FEM model of the empty room was validated, a numerical modal analysis was performed to identify significant room modes and consequently define appropriate strategies of acoustic treatment. Considering the axes orientation as depicted in Figure 51, the room mode (0,1,1) occurring at 66.6 Hz was chosen since it is responsible for one of the highest SPL peaks in the frequency responses shown in Figure 50. Although a Schroeder frequency equal to 335 Hz was retrieved from reverberation time measurements, the main goal here was to identify lowest modes to be damped by means of resonant absorption peaks typical of a single panel absorber. In light of the above, a panel absorber was designed according to Eq. 118, following the most common stratigraphy of such devices, as depicted in Figure 52. It was composed of the following elements:

- a MDF plate of 5 mm thickness secured to the lateral MDF rigid frames by means of wood screws, in order to emulate clamping conditions at the edges. Mechanical properties of the material were partially provided by the manufacturer and partially found in literature [8]. They are summarized, together with geometrical features, in Table 10;
- an air layer of 2 cm thickness;
- a rigid backed glasswool layer of 16 cm thickness, with an air flow resistivity σ=5537 rayls/m. This quantity was experimentally measured by means of an acoustic method developed by Dragonetti et al. [7].

$L_y[m]$	$L_z[m]$	$h[mm]$	E^* $[GPa]$	ν^* $[-]$	η^* $[-]$	ρ $[kgm^{-3}]$
1.35	1.00	5.00	3.70	0.25	0.05	760.00

Table 10: Mechanical properties of the MDF thin plate: L_y and L_z (side lengths), h (thickness), E (elastic modulus), ν (Poisson's ratio), η (material loss factor), ρ (mass density). The values of quantities denoted with * notation are drawn from Bies and Hansen [8].

For this last purpose it is worthwile to highlight the experimental procedure adopted to retrieve the air flow resistivity of the porous layer. As well established, steady state and alternate airflow based methods are defined by the standards [47] and [48]. Nevertheless, both would require very specific instrumentation, namely a flow meter for the former case and high performance microphones able to properly

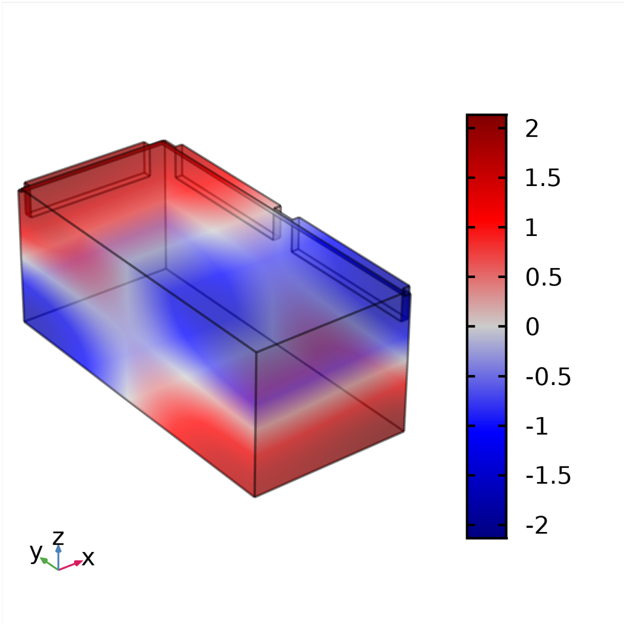

Figure 51: Room mode (0,1,1) at 66.6 Hz in the empty room configuration.

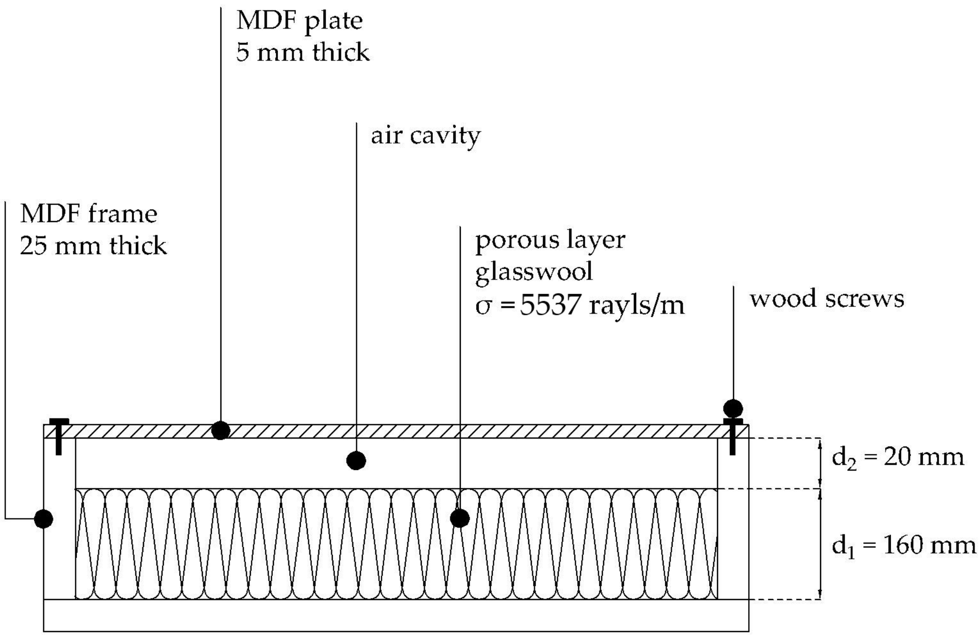

Figure 52: Stratigraphy of the designed panel absorber: a 5 mm thick MDF plate is backed by a 20 mm deep air gap and a 160 mm thick glasswool layer, rigidly backed by a 25 mm thick MDF frame.

detect pressure fluctuations at 2 Hz, in the latter case. Such requirements were overcome with the method proposed by Dragonetti et al. [7], which implies the use of standard measurement microphones due to the application of an indirect acoustical method based on alternate airflow at frequencies higher than 2 Hz. The experimental test-rig, depicted in Figure 53, was constituted of an impedance tube segment of circular cross section of 10 cm diameter, in which two cavities were present above and below the loudspeaker driver. According to proper assumptions and approximations which are well explained in the related paper [7], the flow resistance R_a can be obtained according to the equation:

$$im(r) = -\omega \bar{C}_{dw} R_a \tag{123}$$

where ω is the angular frequency, $\bar{C}_{dw}$ is the acoustic compliance of the cavity downstream of the loudspeaker and $im(r)$ is the imaginary part of the ratio between the sound pressures measured in the upper and lower cavities. An in depth analysis revealed that $im(r)$ decays almost linearly in frequency below a certain upper limit f_{lim}. According to this, the flow resistance R_a of the glasswool samples in question was calculated as the slope of the linear regression of $im(r)$ which, for the sample and the measurement apparatus, in question was considered valid below 40 Hz (Figures 53-54). The average value of measurements carried out on three different samples turned out to be equal to 5537 rayls/m, which is in good accordance to the manufacturer technical datasheet which provided a value of air flow resistivity of 5000 rayls/m.

The resulting surface impedance and absorption coefficient are reported in Figures 56 and 57. As noticeable from the graphs, the highest absorption peak above 50 Hz is achieved within the 65-75 Hz frequency interval, which includes the (0,1,1) eigenfrequency occurring at 66.6 Hz. Additional absorption peaks are observable at 92, 137, 156, 161 Hz and 179 Hz, although resonances above 100 Hz result to be significantly more damped than the others. Two different treatment configurations were proposed in accordance with the room modeshape shown in Figure 51. Since a uniform sound pressure distribution is clearly noticeable in correspondence of room corners, and considering that all the standing wave antinodes are located in that areas, a first treatment configuration was proposed by placing one single panel absorber at a room corner. In order to enhance sound absorption effects, a further configuration was introduced, placing an additional panel absorber with the same characteristics at the other corner along the same side of the room (Figure 58).

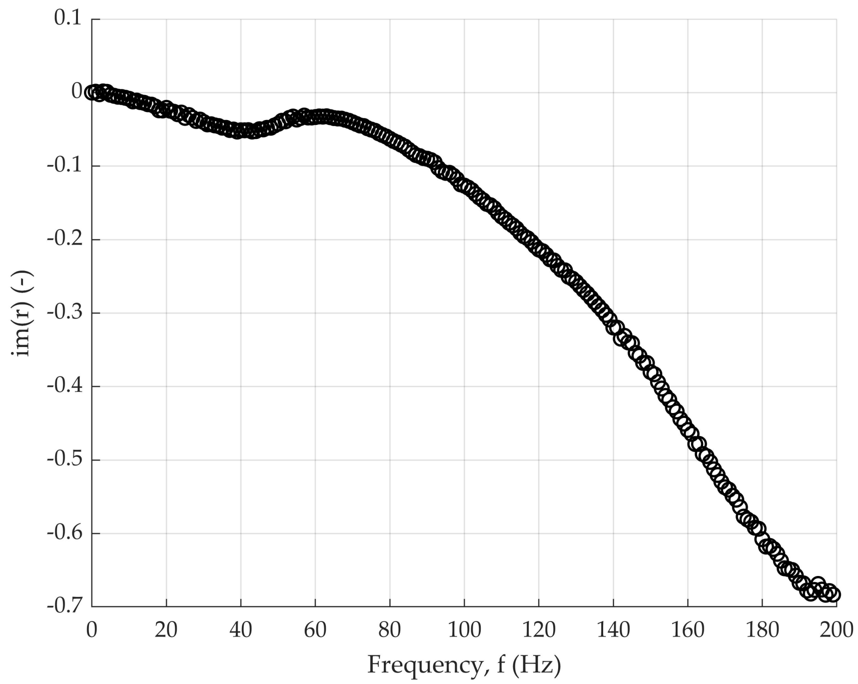

Figure 53: Trend of $im(r)$ over frequency: a linear decay is observable below $f_{lim} = 40$ Hz.

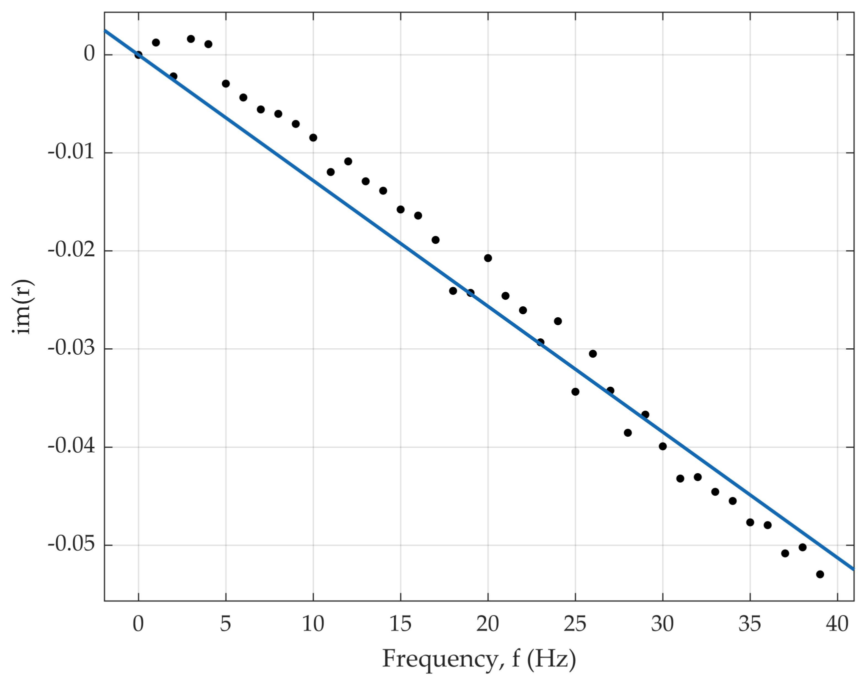

Figure 54: Linear regression of $im(r)$ values within the frequency interval 0-40 Hz.

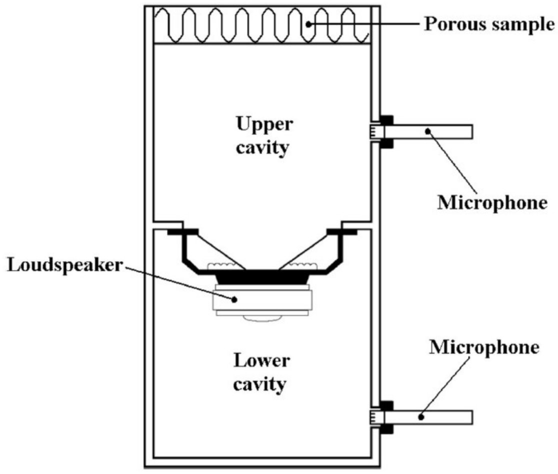

Figure 55: Experimental test-rig for the evaluation of the air flow resistance of porous materials, according to the method proposed by Dragonetti et al. [7].

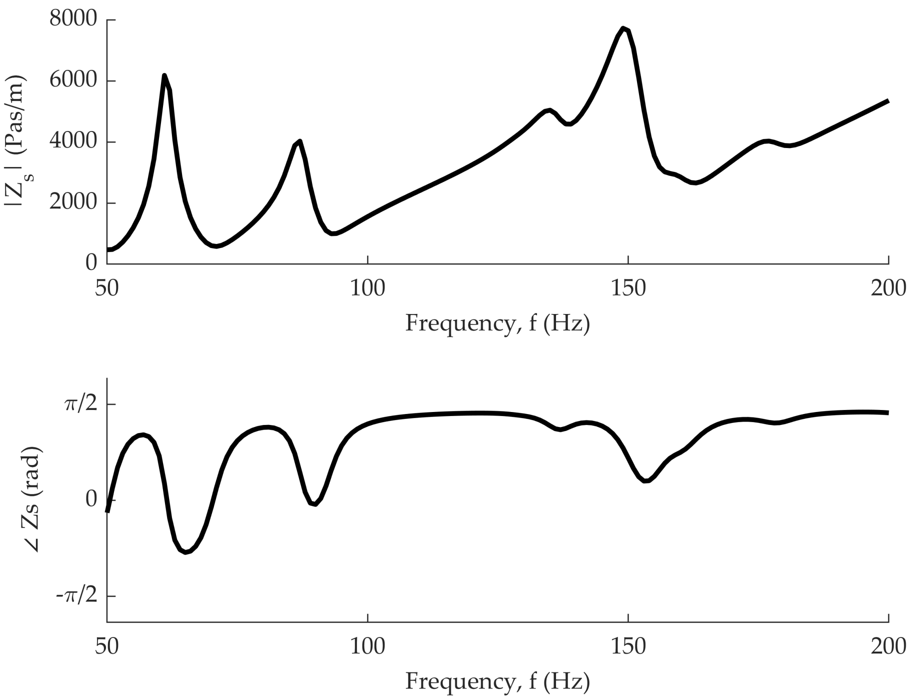

Figure 56: Magnitude (top) and phase (bottom) of the surface acoustic impedance of the panel absorber depicted in Figure 52.

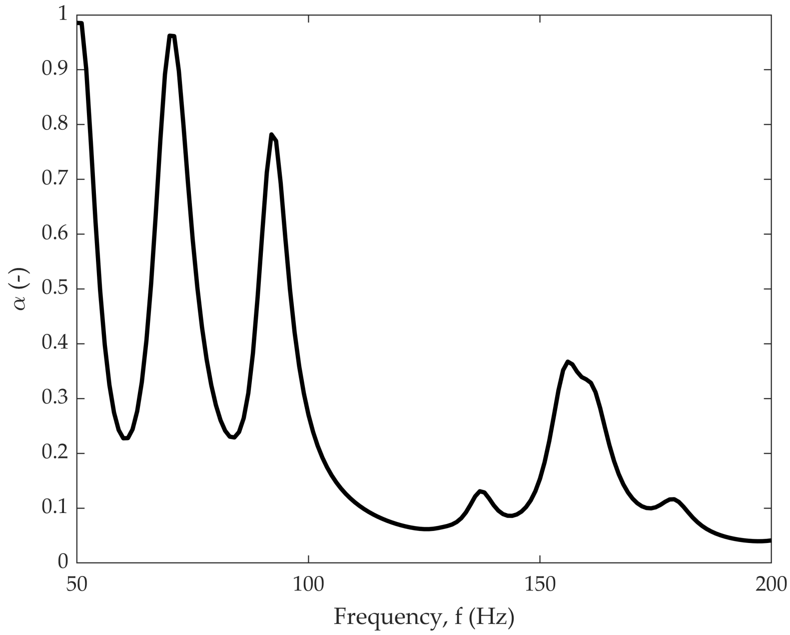

Figure 57: Sound absorption coefficient of the panel absorber depicted in Figure 52.

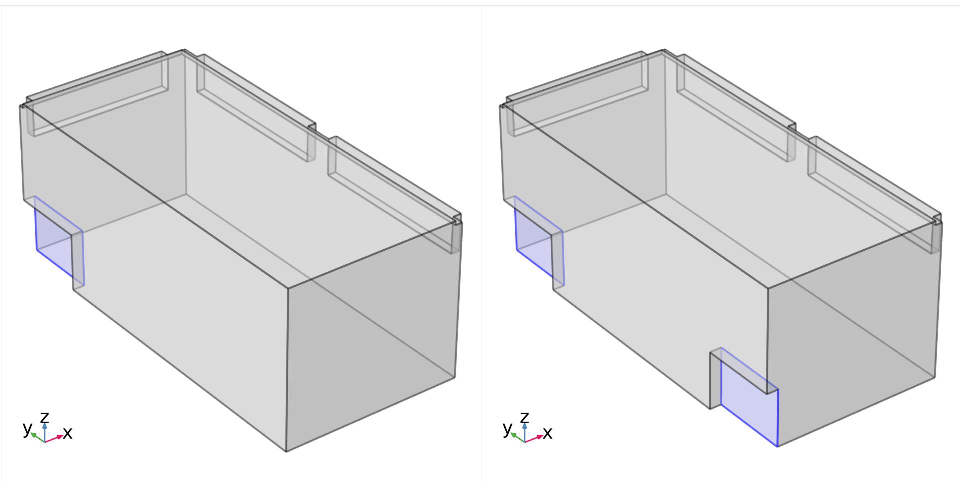

Figure 58: 3D models of the treated room configurations: single panel treatment (left-hand side); double panel treatment. Impedance conditions are assigned to the surfaces highlighted in blue (right-hand side).

9 The acoustic FEM model of a treated room: experimental validation

Treated room configurations were modelled in FEM by assigning a surface averaged and frequency dependent impedance condition, as defined in Eq. 118, to the boundary surfaces corresponding to panel absorbers, according to the three-dimensional models depicted in Figure 58. It is worth noting that absorptive surfaces were assumed to behave as locally reacting. Besides the introduction of such an impedance function, unknown acoustic damping already present in the untreated room was introduced by using the same frequency dependent complex speed of sound, as in the case of the empty room model validation. Assigning an impedance boundary condition to panel absorbers relies on the aim of circumventing the need of a multiphysics simulation, reducing the model to a purely acoustic domain and consequently the physics involved in the model and its number of nodes. Room impulse response measurements were carried out, by installing one panel absorber at a time, according to the two configurations of treatment proposed, as shown in Figure 59. Test signal, equipment and data postprocessing were the same as the case of empty room measurements. Numerical and measured SPL responses were compared at receivers R1, R2 and R3 for both configurations of treatment (Figures 60-61).

Figure 59: Pictures of the sound panel absorbers installed at room corners: single panel configuration (left-hand side); double panel configuration (right-hand side).

Given the results shown in Figures 60 and 61, a more detailed comparison between measured and simulated data is presented here, by performing analyses in both frequency and time domain. In the first instance, difference spectra ΔL_p at receiver positions between empty room and treated room responses were calculated in terms of sound pressure level, as follows:

$$\Delta L_{p,i}(f) = L_{p,empty}(f) - L_{p,i}(f), \tag{124}$$

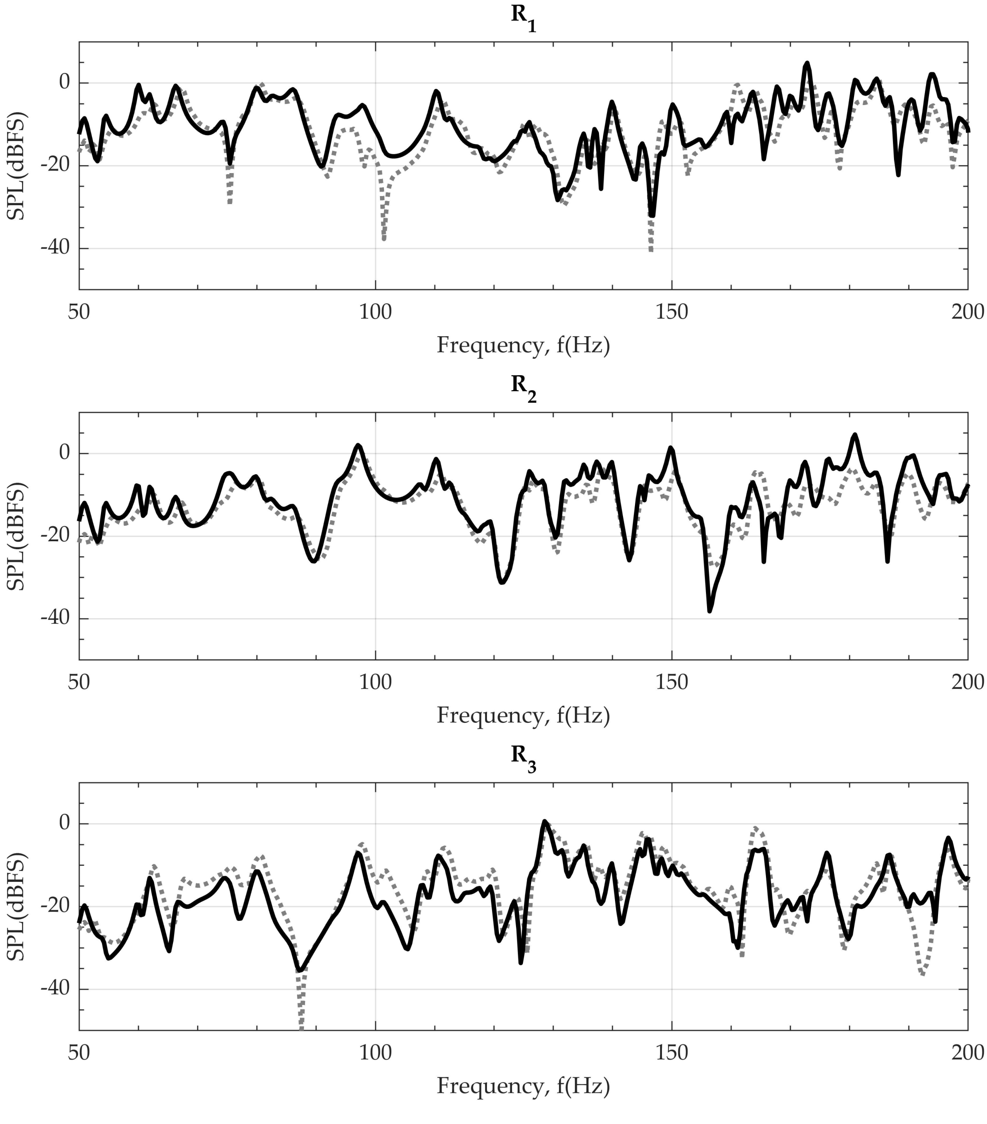

Figure 60: SPL full scaled frequency responses at receiver positions for the single panel treatment configuration at receivers R1, R2 and R3. ....measured values; ——simulated values.

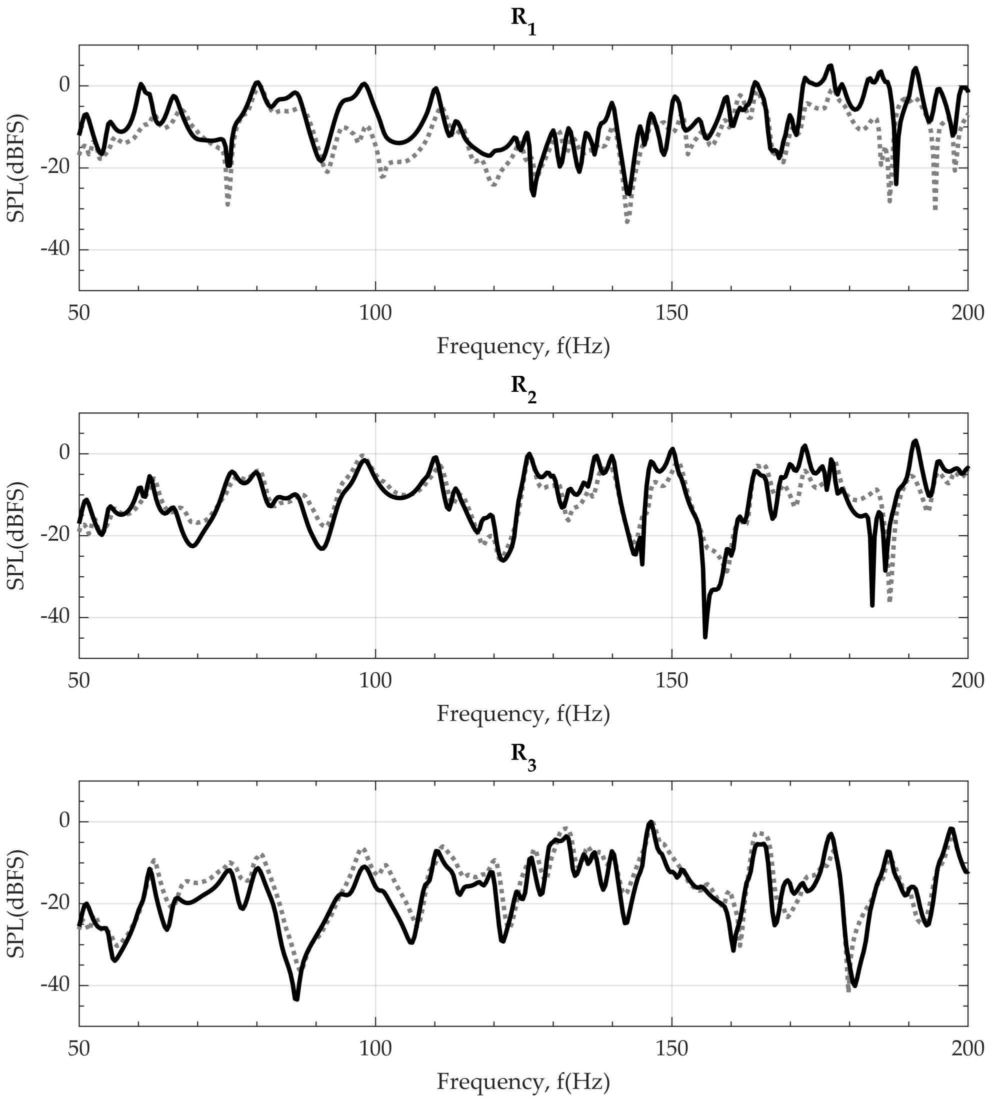

Figure 61: SPL full scaled frequency responses at receiver positions for the double panel treatment configuration at receivers R1, R2 and R3. ....measured values; ——simulated values.

Receiver	$\Delta L_{p,1}$ avg error [dB]	$\Delta L_{p,2}$ avg error [dB]
R1	2.52	3.85
R2	2.45	4.09
R3	2.03	2.73

Table 11: Frequency averaged errors between measured and simulated $\Delta L_{p,1}$ and $\Delta L_{p,2}$ at R1, R2 and R3 receiver positions.

where the index $i = 1, 2$ respectively refers to the single panel ($i = 1$) and double panel ($i = 2$) treatment configurations. Difference spectra were calculated to highlight absorption effects due to the single and double panel treatments with respect to the empty room configuration, minimizing possible non linear effects due to the loudspeaker response, which may affect error estimation between numerical and measured data. Figure 62 shows the difference spectra $\Delta L_{p,1}$ and $\Delta L_{p,2}$ calculated at the receiver R1. As visible from the graph, numerical and measured spectra are in good accordance, showing frequency averaged errors of 2.52 dB for $\Delta L_{p,1}$ and 3.85 dB for $\Delta L_{p,2}$. Averaged errors for each receiver and treatment configuration are summarized in Table 11. Difference spectra were calculated as well for the SPL responses evaluated at receiver positions in a FEM multiphysics simulation. On this purpose, an additional FEM model was set up in which, differently from the acoustics FEM simulations, panel absorbers were modelled in the same way done for the numerical analyses in Chapter 6, by assigning specific physics to each element of the resonator. In particular, the clamped vibrating plate was modelled as a clamped shell, holding valid the assumption of thin plate behaviour; the air cavity was modelled as a separate acoustic domain and the porous layer as an equivalent fluid domain by adopting the Miki model (Figure 63).

The resulting difference spectra at R1 were compared to those evaluated from the acoustic FEM simulations, showing a sensible reduction of the frequency averaged errors for both treatment configurations, as summarized in Table 12. This suggests that a relevant amount of deviation between experimental and acoustic FEM data may be attributable to measurements uncertainties, as expectable. In particular, it is worthwhile evaluating the deviation between difference spectra at the room resonance occurring at 66.6 Hz: as visible from the graphs in Figure 62, in the case of a single panel treatment, the deviation between acoustic FEM and measured data is equal to 2.49 dB and it reduces to 1.68 dB when comparing acoustic FEM to multiphysics FEM data. In the case of a double panel treatment such deviations become respectively equal to 3.28 dB and 2.88 dB.

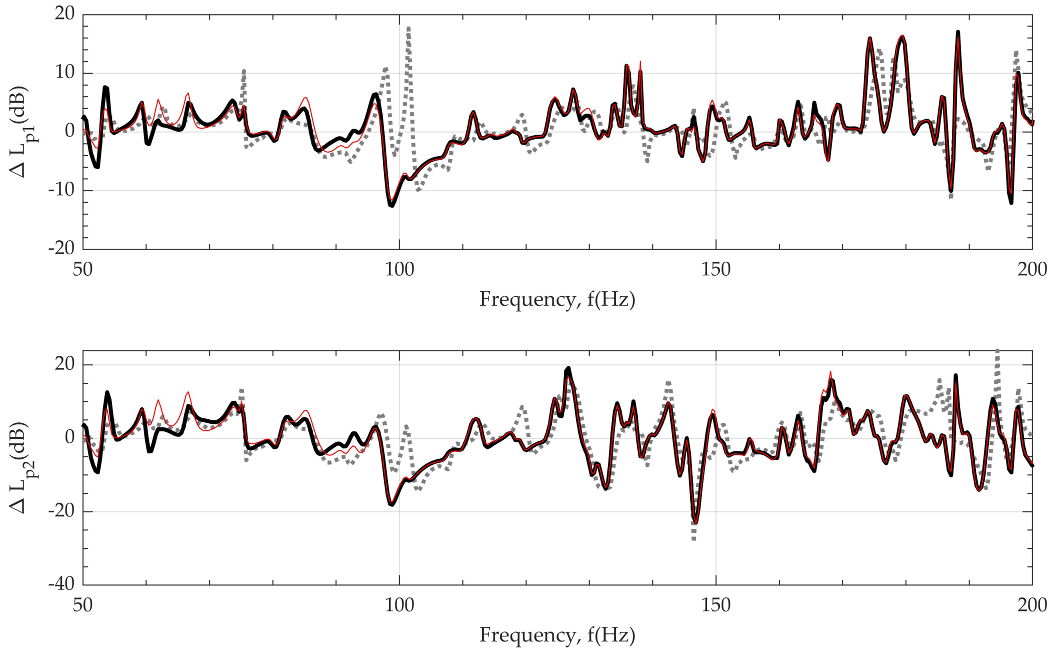

Figure 62: SPL difference spectra at receiver R1: $\Delta L_{p,1}$ (top); $\Delta L_{p,2}$ (bottom). Measured values; acoustic FEM simulated values, multiphysics FEM simulated values.

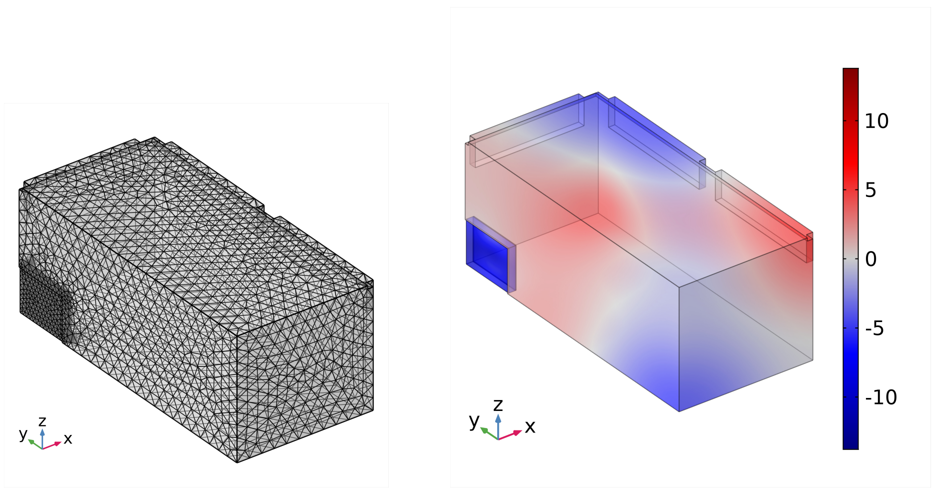

Figure 63: Left-hand side: meshed 3D model for FEM multiphysics simulations of the single panel treatment configuration: air domains were meshed using free tetrahedral elements, the shell was discretised by means of quadratic mapped meshes. Structural-acoustics coupling was assigned as a velocity continuity condition at the interface between air and shell domains. Right-hand side: sound pressure distribution [Pa] throughout the room and within the resonator backing cavity at 66.6 Hz. As visible, at this frequency sound energy is transmitted into the cavity through shell resonant vibration, contributing to the damping of the room mode.

Receiver	$\Delta L_{p,1}$ avg error [dB]	$\Delta L_{p,2}$ avg error [dB]
R1	0.59	1.00
R2	0.52	1.09
R3	0.44	0.67

Table 12: Frequency averaged errors between multiphysics FEM and acoustic FEM $\Delta L_{p,1}$ and $\Delta L_{p,2}$ at R1, R2 and R3 receiver positions.

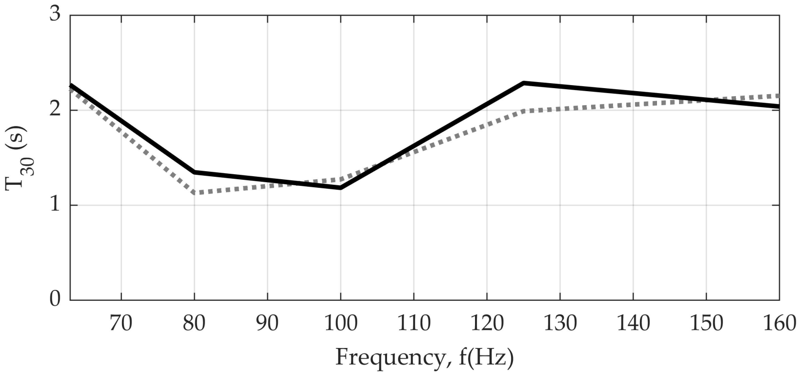

(a)

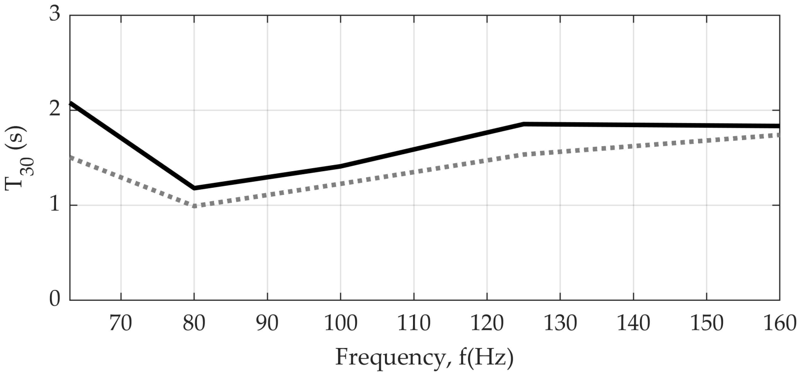

(b)

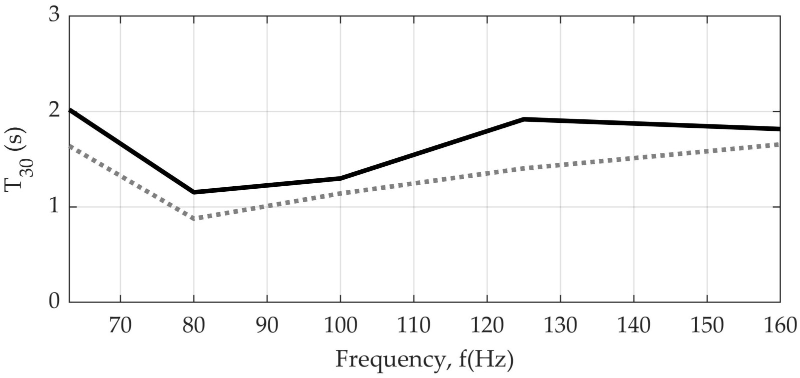

(c)

Figure 64: T_{30} for the three room configurations at receiver R1: (a) Empty Room; (b) single panel; (c) double panel; measured values; acoustic FEM simulated values.

A time domain evaluation of the simulation method was also carried out in order to assess its accuracy in predicting time decays. By means of Inverse Fast Fourier Transform it was possible to convert frequency-domain complex pressure values from stationary acoustic simulations to time-domain impulse responses. These were then compared with the impulse responses measured in the room. The parameter selected for comparison was T_{30} in third octave bands. Here, T_{30} is adopted as an arbitrary measure of energy decay since the measurement procedure does not comply with the relevant room acoustic standard due to proximity to room boundaries. As it can be observed in Figure 64 results and comparable and trends are similar. Average estimation error has been calculated, showing that the error increases with increasing number of panels: in particular, a frequency averaged deviation of 0.15 s was calculated for the empty room configuration, which increases to 0.27 s and 0.30 s in the case of single and double panel treatment, respectively. This is likely to be partly due to an uncertainty build-up of the measurement set up where perfect geometry and idealized conditions are not achievable. Another source of uncertainty may also be the calibration of the empty room model through introduction of the acoustic loss factor within FEM models. Since the loss factor is calculated based on third octave T_{30} values, which are interpolated for the required frequency steps, an accurate depiction of the modal decay times is not achievable within the empty room model. With the introduction of absorbers, individual room modes present within a band may be damped while adjacent modes may not, in a fashion that is possibly not accountable for by the interpolation function. This may partly lead to some of the divergence shown within the plot for the treated cases. Results show nonetheless reasonable accuracy for the purpose of T_{30} predictions.

Conclusions

The aim of this thesis was to provide a thorough characterization of the acoustic behaviour of panel absorbers, resulting in the proposal of an analytical predictive model of their surface averaged acoustic impedance, which takes in account the multimodal vibrational behaviour of the thin plate component. In particular, with respect to the existing mass-spring models, here the effects of finite size, the shape of the sample and its edge constraint conditions are investigated and properly included in the formulations. The resulting impedance was obtained by coupling in series existing impedance expressions of the backing cavity to those evaluated for finite sized thin plates of various shapes, subjected to external transverse excitation.

Particular focus was devoted to the analysis of edge clamped panel absorbers, since such type of constraint, although idealized, represents the closest condition to the actual physical behaviour of real plates fixed at the edges. On this purpose, a set of preliminary numerical analyses provided evidence about the critical effects due to different boundary conditions on the resulting eigenfrequencies of a transversely vibrating plates.

The analytical expression of the acoustic impedance of circular and rectangular isolated clamped plates was compared against experimental acoustic measurements in an impedance tube, showing their validity in the case of plane normal sound incidence. Once this impedance was validated, it was coupled in series to the acoustic impedance of a backing cavity, including the option of a multilayered cavity with a layer of porous material inserted. Numerical validations of such expressions were achieved by means of FEM simulations, still assuming a plane wave normal incidence condition. Furthermore, the effects of porous layers within the cavity were investigated by parametrically varying their thickness and flow resistivity. Results showed that, changing the air flow resistivity among a plausible range of value for porous materials used in acoustical applications, does not significantly affects the overall efficiency of the system in terms of sound absorption. Conversely, different thicknesses of the porous layer have a relevant effect in terms of resonance frequencies shifting and absorption peaks. Furthermore, a preliminary numerical investigation was conducted in order to evaluate the response of a baffled square panel absorber in conditions of spherical incidence, for several heights of the sound source above the sample. In this case, the impedances evaluated numerically show no significant changes in proximity of the resonance frequencies as predicted by the analytical model. Nonetheless, relevant effects are observable in proximity of the antiresonances, where the numerical impedances become smaller the closer the source to the absorber surface. Such an effect may be attributed to pressure phase lags occurring over the surface of the sample due to the spherical wavefront, although a more detailed experimental investigation is required for a more precise estimation.

The applicability of the analytical surface impedance expression as a boundary impedance condition in room acoustic FEM models was then tested, by performing a numerical-experimental analysis. In particular, a real sized room with a reasonably extended low modal density region (20-335 Hz), was chosen for testing in-situ the absorption efficiency of panel absorbers, with particular reference to their effectiveness in dampening low frequency room modes. For this purpose, a FEM model of the empty room was validated against impulse response measurement by comparing sound pressure level responses at several receiver positions, showing a frequency averaged error smaller than 4 dB between numerical and experimental responses. Once the empty room was validated, two different configurations of acoustic treatment were presented, by designing panel absorbers according to the proposed analytical model. The resulting surface impedances were then assigned to the boundary surfaces associated to the position of panel absorbers within the room, setting a purely acoustical FEM model. In light of this, treated room FEM models for single and double panel configurations were validated against impulse response measurements. Results were compared in terms of difference spectra between the empty room and treated configurations, for both FEM and measured data. The frequency averaged deviation between FEM and experimental difference spectra was smaller than 3 dB in the case of a single panel and smaller than 4.5 dB in the case of a double panel configuration. Difference spectra deviations were also calculated comparing FEM data against the results of additional multiphysics FEM simulations. In this case, a maximum deviation value of 1.09 dB was observed, suggesting that a relevant amount of deviation between experimental and acoustical FEM data may be partly attributable to the uncertainty build-up of the experimental set up. Numerical and experimental results were also compared in terms of reverberation time T_{30}, showing a slight increment in deviations by increasing the number of absorbing panels. Given the above, further work is planned to investigate the accuracy of the method by significantly expanding the surface extension and the type of panel absorbers in the room, in which other kinds of absorptive surfaces, such as porous absorbers, are eventually present. Nonetheless, the results obtained so far are promising towards the chance of bypassing multiphysics simulations when modelling panel absorbers in a room, at least at low frequency, by adopting such a methodology. This would be beneficial in terms of computational costs, which would be extremely reduced in the case of purely acoustical FEM simulations. Possible further developments may involve the implementation of this methodology into different numerical methods, in order to test its spectrum of applicability.

References

[1] K. H. Yang, *Basic Finite Element Method As Applied to Injury Biomechanics.* Elsevier Science and Technology Books, 2017.

[2] E. Ventsel and T. Krauthammer, *Thin Plates and Shells: Theory, Analysis, and Applications.* CRC Press, 2001.

[3] R. Szilard, *Elastic Plate Theories and Their Governing Differential Equations.* John Wiley and Sons, Ltd, 2004.

[4] T. Cox and P. D'Antonio, *Acoustic Absorbers and Diffusers.* CRC Press, 2016.

[5] B. H. Song and J. S. Bolton, "A transfer-matrix approach for estimating the characteristic impedance and wave numbers of limp and rigid porous materials," *The Journal of the Acoustical Society of America*, vol. 107, no. 3, pp. 1131–1152, 2000.

[6] "Iso 10534-2:1998 acoustics - determination of sound absorption coefficient and impedance in impedance tubes - part 2: Transfer-function method."

[7] R. Dragonetti, C. Ianniello, and R. A. Romano, "Measurement of the resistivity of porous materials with an alternating air-flow method.," *The Journal of the Acoustical Society of America*, vol. 129 2, pp. 753–64, 2011.

[8] D. Bies, C. Hansen, and C. Howard, *Engineering Noise Control, Fifth Edition.* 2017.

[9] L. Cremer and M. Heckl, *Structure-Borne Sound.* Springer Berlin Heidelberg, 1988.

[10] A. W. Leissa, *Vibration of Plates.* National Areonautics and Space Administration, 1969.

[11] S. S. Rao, *Vibration of Continuous Systems.* John Wiley & Sons, Inc., 2006.

[12] F. Bongard, H. Lissek, and J. R. Mosig, "Acoustic transmission line metamaterial with negative/zero/positive refractive index," *Phys. Rev. B*, vol. 82, pp. 094306–1–094306–11, 2010.

[13] Z. Skvor, *Vibrating systems and their equivalent circuits.* Elsevier, 1991.

[14] S. Yu and X. Yin, "A generalized superposition method for accurate free vibration analysis of rectangular plates and assemblies," *The Journal of the Acoustical Society of America*, vol. 145, no. 1, pp. 185–203, 2019.

[15] Y. Zhu, B. Liu, and K. Zhang, "Wave superposition method applied to calculate the radiation sound power of a stiffened plate," *Journal of Physics: Conference Series*, vol. 1549, no. 5, p. 052072, 2020.

[16] D. J. Gorman, *Vibration Analysis of Plates by the Superposition Method.* WORLD SCIENTIFIC, 1999.

[17] R. Li, P. Wang, R. Xue, and X. Guo, "New analytic solutions for free vibration of rectangular thick plates with an edge free," *International Journal of Mechanical Sciences*, vol. 131–132, pp. 179–190, 2017.

[18] J. W. Strutt, *The Theory of Sound*, vol. 2 of *Cambridge Library Collection - Physical Sciences.* Cambridge University Press, 2011.

[19] G. B. Warburton, "The vibration of rectangular plates," *Proceedings of the Institution of Mechanical Engineers*, vol. 168, no. 1, pp. 371–384, 1954.

[20] C. Sung and J. Jan, "The response of and sound power radiated by a clamped rectangular plate," *Journal of Sound and Vibration*, vol. 207, no. 3, pp. 301–317, 1997.

[21] T.-Y. Huang, C. Shen, and Y. Jing, "On the evaluation of effective density for plate- and membrane-type acoustic metamaterials without mass attached," *The Journal of the Acoustical Society of America*, vol. 140, no. 2, pp. 908–916, 2016.

[22] N. Jiménez, O. Umnova, and J. P. Groby, eds., *Acoustic Waves in Periodic Structures, Metamaterials, and Porous Media.* Springer International Publishing, 2021.

[23] D. E. Muller, "A method for solving algebraic equations using an automatic computer," *Mathematical Tables and Other Aids to Computation*, vol. 10, no. 56, p. 208, 1956.

[24] E. T. Lee and J. W. Wang, *Statistical Methods for Survival Data Analysis. Appendix A: Newton Raphson Method.* John Wiley and Sons, Ltd, 2003.

[25] H. Kuttruff, *Room Acoustics.* CRC Press, 2016.

[26] R. Ford and M. McCormick, "Panel sound absorbers," *Journal of Sound and Vibration*, vol. 10, no. 3, pp. 411–423, 1969.

[27] W. Frommhold, H. Fuchs, and S. Sheng, "Acoustic performance of membrane absorbers," *Journal of Sound and Vibration*, vol. 170, no. 5, pp. 621–636, 1994.

[28] J. F. Allard and N. Atalla, *Propagation of Sound in Porous Media.* Wiley, 2009.

[29] Y. Miki, "Acoustical properties of porous materials : Modifications of delany-bazley models," *The Journal of The Acoustical Society of Japan (e)*, vol. 11, pp. 19–24, 1990.

[30] "Astm e2611-19 - standard test method for normal incidence determination of porous material acoustical properties based on the transfer matrix method," 2019.

[31] L. Savioja and U. P. Svensson, "Overview of geometrical room acoustic modeling techniques," *The Journal of the Acoustical Society of America*, vol. 138, no. 2, pp. 708–730, 2015.

[32] F. Brinkmann, L. Aspock, D. Ackermann, S. Lepa, M. Vorlander, and S. Weinzierl, "A round robin on room acoustical simulation and auralization," *The Journal of the Acoustical Society of America*, vol. 145, no. 4, pp. 2746–2760, 2019.

[33] M. Petyt, *Finite Element Techniques for Acoustics*, pp. 51–103. Vienna: Springer, 1983.

[34] L. L. Thompson, "A review of finite-element methods for time-harmonic acoustics," *The Journal of the Acoustical Society of America*, vol. 119, no. 3, pp. 1315–1330, 2006.

[35] R. Petrolli, P. D'Antonio, J. Storyk, J. Hargreaves, and T. Betcke, "Non-cuboid iterative room optimizer," 2020.

[36] R. Opdam, D. D. Vries, and M. Vorlaaender, "Simulation of non-locally reacting boundaries with a single domain boundary element method," in *Proceedings of Meetings on Acoustics*, ASA, 2013.

[37] C. Wan, C.-J. Zheng, C.-X. Bi, and Y.-B. Zhang, "A boundary element eigensolver for acoustic resonances in cavities with impedance boundary conditions," *The Journal of the Acoustical Society of America*, vol. 147, no. 6, pp. EL529–EL534, 2020.

[38] B. Hamilton and S. Bilbao, "Fdtd methods for 3-d room acoustics simulation with high-order accuracy in space and time," *IEEE/ACM Transactions on Audio, Speech, and Language Processing*, vol. 25, no. 11, pp. 2112–2124, 2017.

[39] G. Fratoni, B. Hamilton, and D. D'Orazio, "Feasibility of a finite-difference time-domain model in large-scale acoustic simulations," *The Journal of the Acoustical Society of America*, vol. 152, no. 1, pp. 330–341, 2022.

[40] J. Reiss, "Pressure-tight and non-stiff volume penalization for compressible flows," *Journal of Scientific Computing*, vol. 90, no. 3, 2022.

[41] S. Bilbao, "Immersed boundary methods in wave-based virtual acoustics," *The Journal of the Acoustical Society of America*, vol. 151, no. 3, pp. 1627–1638, 2022.

[42] M. Aretz and M. Vorlaender, "Efficient modelling of absorbing boundaries in room acoustics fe simulations," *Acta Acustica united with Acustica*, 2010.

[43] R. Dragonetti, M. Napolitano, and R. A. Romano, "A study on the energy and the reflection angle of the sound reflected by a porous material," *The Journal of the Acoustical Society of America*, vol. 145, no. 1, pp. 489–500, 2019.

[44] B. Mondet, J. Brunskog, C.-H. Jeong, and J. H. Rindel, "From absorption to impedance: Enhancing boundary conditions in room acoustic simulations," *Applied Acoustics*, vol. 157, pp. 106884–1–106884–13, 2020.

[45] R. Dragonetti and R. A. Romano, "Errors when assuming locally reacting boundary condition in the estimation of the surface acoustic impedance," *Applied Acoustics*, vol. 115, pp. 121–130, 2017.

[46] N. Roozen, L. Labelle, M. Rychtarikova, and C. Glorieux, "Determining radiated sound power of building structures by means of laser doppler vibrometry," *Journal of Sound and Vibration*, vol. 346, pp. 81–99, 2015.

[47] "Iso 9053-1:2018 acoustics - determination of airflow resistance - part 1: Static airflow method."

[48] "Iso 9053-2:2020 acoustics - determination of airflow resistance - part 2: Alternating airflow method."